CAVITY SOLITONS IN SILICON NITRIDE MICRORESONATORS

A Dissertation

Presented to the Faculty of the Graduate School

of Cornell University

in Partial Fulfillment of the Requirements for the Degree of

Doctor of Philosophy

by

Chaitanya Suhas Joshi

August 2019

CAVITY SOLITONS IN SILICON NITRIDE MICRORESONATORS

Chaitanya Suhas Joshi, Ph.D.

Cornell University 2019

Silicon Photonics is a field of research that has attracted a lot of interest in the past few decades and has led to the development of compact structures on chip for the confinement and manipulation of light. The ability to confine light in a small mode area in waveguides has enabled the exploration of non-linear optical phenomena on chip including frequency conversion using four wave mixing. Recently, demonstrations of chip-based optical frequency combs generated in microresonators fabricated using CMOS compatible materials and fabrication processes has become a rapidly developing field of research. The ability to generate a broadband optical spectrum on-chip by injecting a single frequency continuous wave laser into the microresonator holds promise in enabling applications of these combs in spectroscopy, metrology, and optical data communications. The ability to precisely control the generation of an optical frequency comb and repeatedly achieve low-noise operation is especially important to these applications.

In this dissertation we set out to solve the problem of precise control and repeatable low-noise frequency comb generation in microresonators. In the first part of the dissertation, we investigate thermally controlled cavity soliton generation in silicon nitride microresonators by means of current control of integrated heaters. We report a method to stably and repeatably access cavity soliton states in a silicon nitride microresonator and control the detuning dependent properties of the soliton states using the integrated heaters. We characterize the RF

noise characteristics of these soliton modelocked states and study the ability to generate single and multiple solitons within one cavity round trip.

In the second part of the dissertation we investigate some of the applications of cavity solitons in silicon nitride microresonators. We study the bidirectionally pumped regime of operation of silicon nitride microresonators and demonstrate tunable generation of counter-rotating solitons in a single cavity. We also study the tunability of the soliton trains in opposite directions as a function of pump power ratio in the two directions. We also study a dual comb source consisting of soliton trains generated in two distinct microresonators by maintaining them at a fixed offset in their repetition rates determined by electircal feedback on one of the heaters. The tunability of the offset frequency between the two soliton trains is studied. The tunable dual comb source is applied to a distance ranging measurement where the ambiguity imposed by the fixed repetition rate of the signal comb is lifted by tuning it with respect to the other comb that acts as a local oscillator.

The work presented in this dissertation paves the way for further exploration of applications of cavity solitons generated in silicon nitride microresonators in a reliable and precisely controlled manner.

BIOGRAPHICAL SKETCH

Chaitanya Suhas Joshi was born on Sunday the 3rd of September, 1989 in Thane, India. The eldest son of Meenakshi and Suhas, he spent his first few days at home amid the festivities of the Ganesh Festival, and that is probably where his sweet tooth and also his love of a good drum solo comes from. After spending various parts of his schooling in Pune, Clearwater, Thiruvananthapuram, and Bangalore, Chaitanya completed his school education back where he started it in Pune.

He matriculated in the Fall of 2007 at the Indian Institute of Technology, Guwahati majoring in Engineering Physics. His four years in Guwahati gave him a lifelong love of swimming, classic rock, and competitive quizzing. Those years also laid the foundation for a long process of learning in photonics that has led eventually to this dissertation. It started with the alignment of a Michelson interferometer in the first Physics lab to an internship after his sophomore year at the Tata Institute of Fundamental Research, Mumbai under the mentorship of Prof. Shriganesh Prabhu, understanding the basics of Terahertz Time Domain Spectroscopy. With some more experience in photonics under his belt, he spent a summer at the Technische Universiteit Delft after his junior year of undergraduate studies working on a cross correlation measurement of ultrashort pulses under the mentorship of Prof. Paul Urbach. These experiences crystallized a resolve to go on to do graduate studies in the field of photonics.

In the fall of 2011 he enrolled at Cornell University in the Master of Sciences program in Applied Physics. In Ithaca he rediscovered his love for biking by exploring bike routes around the campus and Cayuga Lake. He worked on his thesis under the guidance of Prof. Alexander Gaeta exploring temporal measurements of short pulses using a two-photon absorption based interferometric

autocorrelator. Chaitanya loved his time on the hill enough to decide to stay on and do a Ph.D. in Applied Physics. A couple of years into his doctoral studies, there was a slight change in scenery from the hills and lakes of Ithaca to the skyscrapers of New York City as the group moved from Cornell University to Columbia University. The work he did during his masters on a autocorrelator to measure pulses generated in silicon nitride microresonators prompted a push towards getting precise control of the pulse formation in these devices. This dissertation is the culmination of those efforts to control pulse formation and study some applications of these pulses.

This document is dedicated to Aai, Baba, and Amol.

ACKNOWLEDGEMENTS

The body of work presented in this dissertation and my journey as a graduate student would not be possible without an incredible support system that has existed including mentors, colleagues, and friends in Ithaca and in New York City as well as family. This dissertation would be incomplete without acknowledging their contributions.

Firstly and most importantly, I would like to thank my advisor Prof. Alexander Gaeta. His deep and complete knowledge of all things that lie within the scope of nonlinear optics has been a constant source of inspiration throughout this span of time that I have spent as a graduate student in his group. Of note in this regard are his 1-1 meetings when he pulls out a paper about a particular phenomenon almost out of thin air within minutes of starting a discussion about it. Alex has assembled a group of extremely talented individuals at Cornell and now at Columbia and their dedication to their work arises just as much from the example that he sets for them as it does from their own drive. Just as he has helped inspire and motivate, Alex has also been a great support at times of crisis within graduate school. Two particular moments within my journey in graduate school come to mind. One was the way in which he managed the move to New York City, pulling all the stops in ensuring that the move felt effortless. The other was at a moment when I got 'scooped' on a project that I was working on. His support in that time really went a long way in rebuilding my confidence and motivation.

The work in this dissertation wouldn't have been possible without Prof. Michal Lipson and her group. The incredible ability that has been built over the years in Michal's group in fabrication of nanophotonic devices has made possible all of the work I have done as a graduate student. A conversation with

Michal leaves you amazed at how crystal clear she sees the big picture and what would make a particular idea worth working on.

A good part of my interactions with Prof. Frank Wise came at the start of grad school while I was still at Cornell. Both as a grader for his nonlinear optics course and in conversations about work. Conversations with Frank are always thoroughly enjoyable and that ensured that I made it a point to drop by his office if I was visiting Ithaca even after the move to New York City. He might be the only other person I know whose knowledge of nonlinear optics matches that of Alex.

I have had the privilege of working with a large number of colleagues in Alex's group and this work wouldn't have been possible without their support and friendship. My first interaction within the group was with Dr, Kasturi Saha who I worked with during my masters and took over the silicon nitride frequency comb work from after she left Cornell. I must thank her for laying the foundations of the work that I have been able to carry forward. I enjoy every chance that I get to hang out with Kasturi and Sid when I visit them in Mumbai. Dr. Adrea Johnson was the go-to source for all things outdoors in and around Ithaca and was always up for ice cream or any other dessert. Dr. Stephane Clemmen and Dr, Sven Ramelow were the wise old postdocs sitting next to my desk in the office in Ithaca as I started out as a grad student and coffee breaks with them meant a deep discussion on photonics half of which I couldn't keep up with at the time. I hope that our paths cross in the future somewhere in Europe. Dr. Alessandro Farsi was a senior grad student at the time I joined the group and we have gone on to have a lot of fun in lab and more outside of lab too. Meeting Alessandro, Maya, and Aviva is always a lot of fun when I am on the west coast. Thanks Alessandro for introducing me to Python.

Among the member of Alex's group that have had the most significant influence on my work and life in graduate school I would like to acknowledge Dr. Yoshitomo Okawachi, Dr. Mengjie Yu, Dr. Jae Jang, and Dr. Alexander Klenner. Most of what I have learned on frequency combs and just how to go about working on photonics experiments I owe to Yoshi. I still remember the time a few months into my Ph.D. after teaching me how to generate a comb by tuning the laser, when Yoshi proudly announced at group meeting that we now had another member of the group who could generate combs. Yoshi has as much of an impact on the positive work culture in the group as Alex. He is the perfect sounding board for ideas and questions about work and will take time to patiently explain something to you. After the move to New York City, Yoshi introduced me to this team called the Brooklyn Nets who weren't quite a force back then. But we still went to games anyway and I grew to love that scrappy young team in the borough of Brooklyn thanks to Yoshi. Ting, Kai, and Yoshi host the group very often at their house in New Jersey for barbecues or board game nights and these fun outings act as a glue that binds the group. I hope to continue visiting whenever I have a chance. The time to celebrate the Nets together is now here and I look forward to seeing some banners being raised in Barclays with Yoshi.

Dr. Mengjie Yu joined the group at a similar time as I did and our journeys within the group mirrored each others in some sense. She was working on trying to generate combs in silicon while I was working on the same in silicon nitride. Her ability to almost immediately understand an idea or a problem amazes me every time I have a conversation with her about work. Outside of work I have always enjoyed hanging out with MJ. Whether it be just going out to grab a round of drinks, or driving down from Ithaca to Binghamton to get

some Biryani, or go to basketball games in Brooklyn each one of those activities have been made more fun by MJ being around.

Dr. Jae Jang has been my neighbor in office for the last 4 years after moving to Columbia. His deep understanding of cavity soliton generation has been instrumental in increasing my understanding of them many times over. The meticulous way in which he goes about setting up experiments is something that I am amazed by. He takes on extremely challenging projects and finds a way to get them to work. He also joins me in freely ranting about life, about grad school, and about how experiments sometimes refuse to cooperate and that is something that helps vent in those times. His trash talking of the Aussies is something that I will miss a lot.

Dr. Alexander Klenner worked with me on the silicon nitride frequency comb generation and has taught me most of what I know about feedback loops and instrument control. Hanging out with Klenner over a beer chatting about the meaning of life was a lot of fun while he was here in New York. The parties that he hosted at his place in Harlem were always loads of fun. That reminds me, I need a place to crash when I visit Zurich next.

I would also like to thank Dr. Xingchen Ji, Dr. Kevin Luke and Dr. Steven Miller, from Michal's group whose work on fabrication of the silicon nitride devices and the integrated microheaters has been instrumental in the work that I have been able to do during my years of graduate school.

Outside of work I have had the privilege of making some really good friends in graduate school. Some within Alex and Michal's groups such as Avik, Gauri, Chaitali, Pratham, Ara, Bok, Yun, Xiaohui, Jared, Gaurang, Ipshita, Steve, Chris, and Aseema and a whole bunch of them outside the group at Cornell, Ved, Shreyas, Aniket, Rohil, Amit, Akshay, Tanay, Kritika, Suhani, Ritika, Pooja, Ajay,

Sachin, Ayush, Aman, Arjun, Pankaj and Reet made living in Ithaca and New York City some of the best years of my life.

I have had the most amazing of roommates over the course of grad school. I knew Ved and Shreyas before moving to Ithaca from our intersecting circles in Pune and our shared love of Manchester United, and the moment I got into Cornell I knew who my roommates were going to be. 418, Prospect, and Seneca were some legendary houses that Ved, Shreyas and I have shared. Those houses turned into social hubs on Friday and Saturday night early on in grad school and some of the most fun parties have happened in those houses. They have also hosted heart to heart conversations about love and life that shall not leave the walls of those houses (except for this hint) and impromptu singalong music sessions. Ved's visits to New York to hit the pool tables of Fat Cat are the stuff of legend.

After moving to New York (yes New Jersey) I had a new set of fantastic roommates in Sidharth, Sandeep, Rohit, TJ, Pragya, Santosh, Mukesh, and Divid. You have all made living (almost) in New York City a whole lot of fun. The discussions about the widest range of topics and the intense sessions of Power Grid with Sandeep, Kalyani, Pragya, Pranav,and Shivam are something that made weekends worth looking forward to.

Avik and I got the chance to work on dual combs together towards the end of his stint in grad school, but our friendship extends way beyond that. Avik knows me really well, too well almost, and knows exactly what he can say that will annoy me the most. I enjoy our conversations on all topics under the sun whether it be trading, CMB(!!), politics, religion, quite literally anything under the sun and sometimes above it too. He might be the most social person I know personally, being able to strike a conversation with absolutely anyone he meets.

The last couple of years of his stint in New York City might have been the deepest exploration of New York City's night life that I have done. His move away from New York to the west coast hasn't stopped our interactions and throwing barbs at each other but has just moved it online unless one of us is visiting the other coast.

Gauri is the most lovable fun person to hang out with. Her love of all things Netflix and sweet Reislings is quite something. It can be somewhat intimidating when you have to pick a Riesling that is just right without being a bit too dry for her tastes. I have known Aniket since I was in high school and because of Gauri being here in New York City he keeps dropping by pretty much every weekend and that lets me indulge in an exploration of the fine cafes, breweries, and sports events that the city has to offer with him.

Chaitali is someone who I enjoy having conversations on deep political or social issues. Her adoration of Sharapova and Zverev doesn't make a whole lot of sense to me at times, but it is what it is. The promptness with which she serves a 'vatrat' when I pass a sarcastic comment always makes me chuckle.

Bok and Yun joined the group after our move to Columbia and they are wonderful friends outside of work and great colleagues in lab. Bok knows the best places to eat and drink in New York so I look forward to keeping in touch about recommendations. Yun and his love for the Lakers gives me ample fodder to trash talk him when it comes to basketball.

Gaurang and Ipshita are founding members of the Columbia Chai Club and the common refrain of Chai-time-yeah? at around 4:30 indicates that it is time to grab a cuppa and discuss perhaps Indian Politics or the latest goings on here at Columbia. I also got a chance to work with them to try and revive SPICMACAY at Columbia and it was a fun few events that I helped organize with them. Gau-

rang and I have gone on a few bike rides around the city but I think that we haven't done that nearly enough and is something we need to fix immediately.

Steve, Chris and Aseema were always up for a discussion on the most random of topics whenever I went up to the their office. Steve and Chris are about to change the world of LIDAR and I wish them all the success in that venture. When you heard sounds of Snarky Puppy emanating from the Lipson lab you always knew that Steve is in the zone!

My Ithaca Emo peeps! Tanay, Kritika, Pooja, Ajay, Sachin, Ayush, Aman, Vaibhavi and Shreyas. We have spent so much time listening to great music over a bottle of fine single malt scotch or watching the silliest of movies or just doing nothing at all but hang out in Villager or at my place or at IBC or Americana. The list of places we've been to is endless and long may it last, wherever we meet next.

The first few months after moving to New York were incredible fun hanging out with Suhani and exploring Greenwich Village often at unearthly hours and making sure we tested the limits of PATHs 24 hour service! That was a whole lot of fun until you moved away to greener pastures across the pond. See you in Europe when I next visit!

My photography folks Amit and Akshay, I am probably one paycheck away from buying a half decent camera as I have always said. And that day is almost here. I will see you in the great outdoors soon, hopefully taking some incredible photographs!

Rohil and Reet are always the best of hosts when I visit Ithaca. Rohil and I have known each other since he joined Cornell,then went to Amherst, then to Monroe, then to State College and then back to Cornell. It's always a fun time hanging out with Rohil until suddenly in the middle of it he drifts off and says

he's reading the news on his phone. Wherever life takes you after Cornell we'll be the best of friends be! Reet and his love for quizzing and his enthusiasm to learn and know more are what makes me connect with him. That and our shared love of football.

And last but not the least, I have to thank my family for making me the person I am today. Aai and Baba, you don't know how much of an inspiration you are to me every single day of my life. Being so far away from you can be difficult at times but it doesn't lessen the impact you have on my life. Aai, your conviction in your beliefs and your eagerness to see things through to the end with the kind of tenacity you show inspires me. Baba, your calmness when faced with any situation is something I wish I can learn from you and to do better in my own life. Amol, your drive to be a force of good in society makes me incredibly proud and inspires me to one day try to do the same.

TABLE OF CONTENTS

LIST OF FIGURES

CHAPTER 1

INTRODUCTION

Light is ever present in nature, from the rays of the sun that shine down upon us all day to the tiny pinpricks of light from the stars at night. These natural sources of light have motivated scientific thinkers over the centuries to study and attempt to manipulate their properties. The study of light, optics and photonics, has motivated the most renowned of scientists across our collective human history. From Euclid in ancient Greece who spoke about sight and perspective in Optica, to Newton who in his treatise Opticks, described some of the first recorded experiments of diffraction of light, that introduced the optical spectrum into scientific discourse. More recent researchers have pushed this same spirit of inquiry further to build man-made sources of light that give us unprecedented control over these properties. Many years of innovation led to the building of a practical incandescent lamp by Thomas Edison just before the turn of the 20th century, and by the middle of the 20th century, to the proposal of the first laser by Schawlow and Townes [1] and subsequently the realization of the first laser by Theodore Maiman [2]. Lasers have advanced the study of light by leaps and bounds in these last 60 years and have touched every aspect of our lives, from communication systems based on optical fibers that wrap the entire globe and let us communicate seamlessly, to their use in chemical and biological spectroscopy, and most recently, in LIDAR sensors in our cars with the advent of self-driving technology.

Lasers are ideal sources for studying the interaction of light with matter. Photonics, or the science of light, is the study of these interactions on a microscopic scale. When light interacts with matter it's properties such as polariza-

tion, intensity, and phase, among others are affected by the material it interacts with. At higher optical powers, we start observing nonlinear effects in these light-matter interactions that allow exchange of energy between photons at different frequencies. The ability to draw glass into optical fiber with a core that is tens of microns in diameter and tens or even hundreds of kilometers long with very low absorption losses has allowed for much longer interaction lengths for light with matter. Higher power laser sources and increased interaction lengths of light has made studying these nonlinear effects easier.

Data are the currency of our virtual experience today and with more and more people joining our connected world everyday, the demand for data only keeps growing exponentially. The consumption of data increases almost analogously to or even faster than the famous Moore's law for transistor density [3]. As data transfer speeds keep increasing, fundamental losses in the materials used to design the transistors that make up logic circuits, and the metal interconnects that link these devices become ultimate limitations to how fast a signal can be modulated and transmitted over an electronic link. Over the last few decades the increase in data rates has meant that a significant portion of the infrastructure for data transmission over longer distances of a few to hundreds of miles has moved from using electrical cables to fiber optic cables to maintain the quality of the signal being transmitted. With continuing increase in data rates, moving to optical components over electronic components at smaller and smaller length scales becomes necessary to overcome the limitations imposed by material losses. This has led to significant interest in the development of chip-scale sources of light that are extremely stable and can be controlled easily.

The upcoming revolution in augmented reality (AR), virtual reality (VR),

and autonomous vehicle technologies has placed added impetus on the ability to accurately and rapidly sense our surroundings. This requires sources of light that can be precisely controlled to measure surface profiles and distance information for objects that may be in the immediate vicinity of the AR or VR device or an autonomous vehicle to ensure the quality of the user experience and the safety of the user. The integration of these sources into a compact, chip-scale form factor would enable their deployment in portable devices for these applications.

Spectroscopy is a very powerful tool that allows for the study of material properties by shining light on them and studying how the light is modified by the material. This gives us valuable information about the material that can be used to study the material. Such a study can give valuable information about the composition of an unknown sample, or about the structure of a material based on its energy levels. Broadband optical sources are required for spectroscopy in order to cover a wide range of energies corresponding to various interactions of light with the material.

Devices built to confine light on chip scales can be made using materials that are compatible with methods developed in the semiconductor electronics industry. The refinement of these methods in the quest to keep up with Moore's law allows the design of extremely high quality photonic devices at the chip-scale. Confining light to these small dimensions results in high intensities at which nonlinear effects present themselves. The ability to control and study these nonlinear interactions in on-chip devices offers an avenue to build new sources of light. As this technology matures, it can find applications in communications, chemical and biological sensing and beyond as it passes through the

hands of future innovators.

We tackle some of these challenges in the same spirit of innovation as our scientific predecessors and try to solve these problems using the work presented in this dissertation.

1.1 Outline of the dissertation

This dissertation will introduce and attempt to explain some of these novel chip scale sources of light and mechanisms for their control. We will discuss the control of resonant structures on Silicon Nitride nanophotonic chips thermally and the use of thermal control to generate dissipative cavity solitons in these structures. We will discuss the controlled generation of counter-rotating solitons travelling in opposite directions along the resonator and some of the novel dynamics that we observe in this system. We will also discuss the operation of soliton trains with a difference in repetition frequency generated on two microresonators on a single chip. These offset locked trains of solitons have a difference in repetition rates that is disciplined to the frequency of an external RF source.

Chapter 2 introduces nonlinear optical effects that can be observed due to the interaction of light with materials. We introduce the physics of nonlinear optical interactions with materials and delve into the details of Four Wave Mixing (FWM) the primary nonlinear optical process that governs optical frequency comb generation that is discussed in detail in this dissertation. We also discuss some of the other effects that we observe to affect the dynamics of dissipative cavity solitons in our silicon nitride microresonators. We also introduce optical

frequency combs and how these nonlinear optical effects affect frequency comb generation.

Chapter 3 gives an overview of integrated photonics and how these on-chip devices are built. We discuss the confinement of light in waveguide structures and low-loss resonant structures on-chip. We take a look at the choices of material and how this affects the nonlinear optical properties of our devices.

Chapter 4 discusses thermally controlled generation of dissipative cavity solitons in silicon nitride microresonators. We discuss previous work done on dissipative cavity solitons in fiber and microresonator cavities that laid the foundation for this work. We introduce our technique for thermal control of these resonant structures using on-chip integrated heaters. We discuss our results in devising a method to repeatably generate soliton modelocked frequency combs in silicon nitride microresonators by precisely controlling the detuning of the cavity with respect to a fixed pump laser by varying the current applied to on-chip integrated heaters.

In Chapter 5 we introduce dual-comb sources for spectroscopy and give an overview of previous approaches to dual comb generation in microresonators as well as discuss bidirectionally pumped microresonator based systems. We then discuss the generation of counter-rotating solitons within a single microresonator. We study this bidirectionally pumped system and explain the novel dynamics that we observe as the control parameter, the ratio in pump power in both directions, is varied.

In Chapter 6 we operate trains of solitons derived from two distinct microresonators on a single chip with a difference in their repetition rate. The

repetition rate of the soliton train from the slave resonator is maintained at a specified frequency difference with respect to the soliton train from the master resonator. The frequency difference is derived from a stable RF source and can be used to generate a tunable dual-comb source disciplined to the RF source by means of electrical feedback applied on to the integrated heaters. We characterize this dual-comb source and demonstrate applications of such a source including ambiguity free ranging.

We conclude in Chapter 7 by discussing other related work based on some of the results presented in this dissertation and potential future applications of the platform established by the work in this dissertation.

CHAPTER 2

NONLINEAR OPTICS

The optical properties of materials are a response of the material to incident light. The response of the material depends on the material structure, symmetry, and also on the properties of the incident light such as polarization, intensity, and frequency among others. Light is a form of electromagnetic radiation that covers a broad range of frequencies, typically ranging from a few gigahertz (GHz) to a few hundreds of terahertz (THz). It is a transverse electromagnetic wave with the electric and magnetic fields oscillating at the frequency of radiation orthogonal to each other and to the direction of propagation of the light. When this light interacts with a material or with an interface between two materials, the properties of the light as well as the materials can be modified. Typically, in a linear optical case, the response of the material properties depends linearly on the strength of the incident electrical field of the light. However given the right conditions, most materials demonstrate a nonlinear response to the strength of the incident electrical field with contributions from higher orders of the electric field, and the study of these nonlinear behaviors is the study of nonlinear optics. The field of nonlinear optics can be considered to have started with the observation of the phenomenon called second harmonic generation (SHG) where upon incidence of the output of a ruby laser at 694.3 nm wavelength onto crystalline quartz, light generated at the second harmonic frequency of the incident light, at 347.2 nm was observed to be generated [4, 5].

2.1 Maxwell's equations and the wave equation

As with all electromagnetic fields, the behavior of light in any material is governed by the Maxwell's equations as described below.

$$\vec{\nabla} \cdot \vec{D} = \rho_f \tag{2.1}$$

$$\vec{\nabla} \cdot \vec{B} = 0 \tag{2.2}$$

$$\vec{\nabla} \times \vec{E} = -\frac{\partial \vec{B}}{\partial t} \tag{2.3}$$

$$\vec{\nabla} \times \vec{H} = \vec{J_f} + \frac{\partial \vec{D}}{\partial t} \tag{2.4}$$

where the electric field $\vec{E}$, and magnetic field $\vec{H}$ are related to the electric flux density $\vec{D}$, and magnetic flux density $\vec{B}$ respectively by the following relations.

$$\vec{D} = \epsilon_0 \vec{E} + \vec{P} \tag{2.5}$$

$$\vec{B} = \mu \vec{H} \tag{2.6}$$

ϵ and μ being the electric permittivity and magnetic permeability respectively of the material in which the light is propagating, determine the induced polarization and magnetization due to the electric and magnetic fields. The materials used in this dissertation are non-magnetic and hence the magnetic permeability μ is simply equal to the vacuum permeability μ_0 = $4\pi \times 10^{-7}$ H/m. The electric permittivity is given by $\epsilon = \epsilon_0(1 + \chi_e)$ where χ_e is the electrical susceptibility. Every material has its own electric permittivity that is dependent on the composition and structure of the material. These differences in material

properties can be utilized to build structures that modify the properties of light in a controlled manner to enable specific regimes of operation.

For dielectric materials such as the ones being used in the devices in this dissertation, the free charges and currents are zero ($\rho_f = 0$ and $J_f = 0$) at the frequencies used in this work. Here $\mu_0\, \epsilon_0 = \frac{1}{c^2}$. Using vector calculus identities and combining the equations above we arrive at the wave equation for light in a dielectric material.

$$\nabla^2 \vec{E} = \frac{1}{c^2}\frac{\partial^2 \vec{E}}{\partial t^2} + \frac{1}{\epsilon_0 c^2}\frac{\partial^2 \vec{P}}{\partial t^2} \tag{2.7}$$

This wave equation admits plane wave solutions of the form,

$$\vec{E}(\vec{r}, t) = E_0 e^{i(\vec{k}.\vec{r} - \omega t)} \tag{2.8}$$

These plane wave solutions indicate a wave propagating with a wave vector $\vec{k}$ in the $\vec{r}$ direction and with a frequency ω.

2.2 Nonlinear polarization

In a dielectric material, due to an incident electromagnetic field, an induced polarization is observed. This is a result of the bound electrons reacting to the field strength of the incident field. In the conventional linear optical case, the induced polarization $\vec{P}$ depends linearly on the applied electric field. and is given by the equation,

$$\vec{P} = \epsilon_0 \chi^{(1)} \vec{E} \tag{2.9}$$

More generally, all materials have a nonlinear response to the applied electric field and the induced polarization is given by expressing the polarization as a power series in the electric field strength.

$$\vec{P} = \epsilon_0[\chi^{(1)}\vec{E} + \chi^{(2)}\vec{E}\vec{E} + \chi^{(3)}\vec{E}\vec{E}\vec{E} + ...] \tag{2.10}$$

These higher order terms in the induced polarization introduce a wide variety of nonlinear effects in the material and its interaction with incident light. These effects can be used, in the right conditions, to manipulate the properties of the material as well as the light.

The Lorentz model for the atom, where an electron is assumed to be bound to the nucleus of the atom by a spring-like force allows for a good primary understanding of linear and nonlinear optical effects. The electrons react to the incident electromagnetic field by vibrating as a damped harmonic oscillator. Depending on the oscillator strength and damping both of which can be directly linked to the material property this would result in the creation of a dipole at each electron-nucleus pair. The sum off all the induced dipole moments over the macroscopic volume of the material would result in an effective material polarization $\vec{P}$ as a response to this incident field $\vec{E}$.

First, we look at the linear optical behavior of the interaction using the Lorentz model to understand how it explains the interaction of light with materials. The motion of the electron in the electron-nucleus system assumes that the nucleus is stationary due to it being much heavier than the electron. The equation describing the motion of the electron is modeled as a damped harmonic oscillator [6].

$$m_e \frac{d^2x}{dt^2} + m_e\gamma\frac{dx}{dt} + m_e\omega_0^2 x = -eE(t) \tag{2.11}$$

Here m_e is the mass of the electron, ω_0 is the resonant frequency of the oscillator, γ is the damping factor of the oscillator. The resonant frequency and the damping factor are material properties which affect how the materials interact with the incident light. The incident light, assumed to be monochromatic will have a field strength $E(t)$ that depends on the frequency of the light, and will drive a response $x(t)$ that is also at the same frequency as evident from the equation of motion.

$$E(t) = E_0 e^{-i\omega t} \tag{2.12}$$

$$x(t) = x_0 e^{-i\omega t} \tag{2.13}$$

By substituting the field Eq. 2.12 and oscillation Eq. 2.13 into the equation of motion Eq. 2.11 we find the amplitude of these oscillations x_0.

$$-m_e\omega^2 x_0 e^{-i\omega t} - im_e\gamma\omega x_0 e^{-i\omega t} + m_e\omega_0^2 x_0 e^{-i\omega t} = -eE_0 e^{-i\omega t} \tag{2.14}$$

$$x_0 = \frac{-eE_0/m_e}{\omega_0^2 - \omega^2 - i\gamma\omega} \tag{2.15}$$

The induced polarization in the bulk material $\vec{P}$ is a macroscopic average over all of the induced dipoles with dipole moments given by $p = -ex_0$ induced in the material.

$$P = -Nex_0 = \frac{Ne^2E_0}{m_e}\frac{1}{\omega_0^2 - \omega^2 - i\gamma\omega} \tag{2.16}$$

From Eq. 2.9 and Eq. 2.16, the first order electric susceptibility $\chi^{(1)}$ is given by,

$$\chi^{(1)} = \frac{Ne^2}{\epsilon_0 m_e} \frac{1}{\omega_0^2 - \omega^2 - i\gamma\omega} \tag{2.17}$$

Here, the linear susceptibility varies as a function of frequency and depends on how far the incident light is from the resonant frequency ω_0. Typically most materials have multiple resonant frequencies that affect the induced polarization and lead to a linear susceptibility that is a sum over the response to all the oscillators.

$$\chi^{(1)} = \frac{Ne^2}{\epsilon_0 m_e} \sum_j \frac{1}{\omega_j^2 - \omega^2 - i\gamma_j\omega} \tag{2.18}$$

The refractive index as a function of frequency can be obtained from the relation given in Eq. 2.18. This variation of the index with frequency limits the gain bandwidth of the nonlinear processes that determines the spectral shape of the frequency combs generated and studied in this dissertation. We will see in Section 2.4 how the gain bandwidth of the Four Wave Mixing process is affected by the dispersion at the pump wavelength, and in Chapter 3 how the variation of index determines the effective dispersion of the waveguides and dictates design choices for the devices used in this dissertation.

In this linear case, the restoring force for the spring model is linear and is of the form $F(x) = -m_e\omega_0^2 x$ which means the system has a potential energy of the form $U(x) = \frac{1}{2}m_e\omega_0^2 x^2$. For a typical material, the restoring force will have a series of terms that would depend on higher powers of the displacement x and this is what lends the nonlinear response to the incident light

on the material. As can be seen from Fig. 2.1 in the case of the first nonlinear term being introduced in the restoring force that takes the form $F(x) = -m_e\omega_0^2 x - m_e a x^2$, the potential becomes asymmetric as a function of x and takes the form $U(x) = \frac{1}{2}m_e\omega_0^2 x^2 + \frac{1}{3}m_e a x^3$. It is evident from the asymmetry of the potential about x=0 that for such a potential to exist in a material, it would require for the material to have an asymmetry about x=0 in terms of crystal structure. This indicates that a second order nonlinearity can only be observed in such non centrosymmetric media.

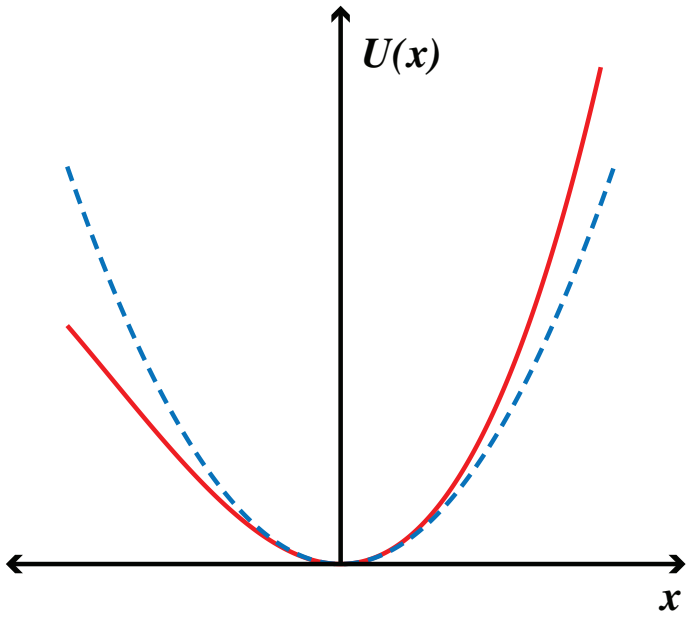

Figure 2.1: The potential energy U(x) in the case of linear (dashed, blue) and second order nonlinear restoring forces(solid,red) as a function of displacement x. The asymmetric potential gives rise to the second order nonlinear susceptibility in non-centrosymmetric media

A third order nonlinear term of the form $-m_e b x^3$ would lend a symmetric nonlinear term in the potential of the form $\frac{1}{4}m_e b x^4$ that would not require for specific symmetry conditions on the material and would be present in a centrosymmetric medium. Most crystalline materials have this form of inversion symmetry and hence a third order nonlinearity can be observed in these

materials given the right conditions. The devices used in this dissertation are fabricated using silicon nitride which shows a third order nonlinearity.

We extend the analysis presented above in the linear case to that of a purely third order nonlinearity in a centrosymmteric medium using a similar approach to that taken in [4]. The restoring force is of the form $F(x) = -m_e\omega_0^2 x + m_e b x^3$. In the case of an isotropic and centrosymmetric material, the force can be expressed in the vector form as,

$$\vec{F} = -m_e\omega_0^2\vec{r} + m_e b(\vec{r}\cdot\vec{r})\vec{r} \tag{2.19}$$

The equation of motion for the electron then becomes,

$$\frac{d^2\vec{r}}{dt^2} + \gamma\frac{d\vec{r}}{dt} + \omega_0^2\vec{r} - b(\vec{r}\cdot\vec{r})\vec{r} = -e\vec{E}(t)/m_e \tag{2.20}$$

We assume an applied electric field given by three distinct frequency terms. This field is assumed to be the case to allow for the most general form of a third order interaction in the analysis. To simplify the expression, the field is expressed as a summation,

$$\vec{E}(t) = \vec{E_1}e^{-i\omega_1 t} + \vec{E_2}e^{-i\omega_2 t} + \vec{E_3}e^{-i\omega_3 t} + c.c. \tag{2.21}$$

$$\vec{E}(t) = \sum_n \vec{E}(\omega_n)e^{-i\omega_n t} \tag{2.22}$$

To separate the different orders for the solution to $\vec{r}(t)$ within the equation of motion, a parameter λ is introduced that can be set to 1 at the end of the analysis.

$$\vec{r}(t) = \lambda \vec{r}^{(1)}(t) + \lambda^2 \vec{r}^{(2)}(t) + \lambda^3 \vec{r}^{(3)}(t) + ... \tag{2.23}$$

Using the λ parameter to separate the different orders of the solution to $\vec{r}(t)$ we get,

$$\frac{d^2\vec{r}^{(1)}}{dt^2} + \gamma \frac{d\vec{r}^{(1)}}{dt} + \omega_0^2 \vec{r}^{(1)} = -e\vec{E}(t)/m_e \tag{2.24}$$

$$\frac{d^2\vec{r}^{(2)}}{dt^2} + \gamma \frac{d\vec{r}^{(2)}}{dt} + \omega_0^2 \vec{r}^{(2)} = 0 \tag{2.25}$$

$$\frac{d^2\vec{r}^{(3)}}{dt^2} + \gamma \frac{d\vec{r}^{(3)}}{dt} + \omega_0^2 \vec{r}^{(3)} - b(\vec{r}^{(1)} \cdot \vec{r}^{(1)})\vec{r}^{(1)} = 0 \tag{2.26}$$

Solving Eq. 2.24 simply yields the linear case as we solved before giving us the linear displacement,

$$\vec{r}^{(1)}(t) = \sum_n \vec{r}^{(1)}(\omega_n) e^{-i\omega_n t} \tag{2.27}$$

where,

$$\vec{r}^{(1)}(\omega_n) = \frac{-e\vec{E}(\omega_n)/m_e}{\omega_0^2 - \omega_n^2 - i\gamma\omega_n} \tag{2.28}$$

The second order term in the displacement $\vec{r}^{(2)}(t)$ is determined by Eq. 2.25 and can be seen to be exactly equal to zero because the equation is not driven by any time varying term. Hence, $\vec{r}^{(2)}(t) = 0$. This is a direct consequence of the centro-symmetry of the material.

Plugging in the solution for the first order displacement Eq. 2.28 into the differential equation for the third order displacement Eq. 2.26, we get,

$$\frac{d^2\vec{r}^{(3)}}{dt^2} + \gamma\frac{d\vec{r}^{(3)}}{dt} + \omega_0^2\vec{r}^{(3)} = -\frac{be^3}{m_e^3}\sum_{mnp}\frac{[\vec{E}(\omega_m)\cdot\vec{E}(\omega_n)]\vec{E}(\omega_p)}{D(\omega_m)D(\omega_n)D(\omega_p)} \tag{2.29}$$

Here $D(\omega_j) = \omega_0^2 - \omega_j^2 - i\gamma\omega_j$ corresponds to the denominators from the linear term.

We can see that the third order response depends on a sum over multiple combinations of frequencies ω_m, ω_n, and ω_p, which means that the frequency dependence of the induced third order displacement $\vec{r}(\omega_q)$ and consequently the third order susceptibility $\chi^{(3)}(\omega_q)$ would depend on different combinations of those frequencies ω_m, ω_n, and ω_p.

Here $\omega_q = \omega_m + \omega_n + \omega_p$ and the frequencies ω_m, ω_n, and ω_p can take positive as well as negative values from the complex conjugate. The presence of a negative frequency can be understood in as an interaction mediated by the annihilation of a photon at that frequency. There are 22 different frequency terms that can be present in the third order nonlinear susceptibility. Some of the nonlinear processes that can take place due to this third order nonlinearity are outlined below,

- Third Harmonic Generation: $\omega_q = 3\omega_m(\omega_m = \omega_n = \omega_p)$,
- Intensity Dependent Refractive Index: $\omega_q = \omega_m = \omega_n = -\omega_p$,
- Self Phase Modulation (SPM): $\omega_q = \omega_m = \omega_n = -\omega_p$,
- Cross Phase Modulation (XPM): $\omega_q = \omega_m \neq \omega_n = -\omega_p$,
- Four Wave Mixing (FWM): $\omega_q \neq \omega_m, \omega_n, \omega_p$.

In this thesis we study various effects that are caused by this third order

nonlinearity, specifically FWM, SPM, and XPM. We discuss these effects below in greater detail.

2.3 Self and cross phase modulation

The self and cross phase modulation is an effect that can be linked to the intensity dependent refractive index of a material [7]. When an intense electric field at a frequency ω propagates through a material, due to the third order nonlinearity, a term at the frequency ω is observed. If we look at the third order polarization term at this frequency it is given by,

$$P^{(3)}(\omega) = 3\epsilon_0\chi^{(3)}(\omega = \omega + \omega - \omega)[E(\omega) \cdot E^*(\omega)]E(\omega) \tag{2.30}$$

The induced polarization due to the incident wave at a frequency ω includes the linear and nonlinear polarization from Eq. 2.30 and is given by,

$$P(\omega) = \epsilon_0\chi^{(1)}E(\omega) + 3\epsilon_0\chi^{(3)}\left|E(\omega)\right|^2 E(\omega) \tag{2.31}$$

The refractive index can be related to the susceptibility in this case as below [4],

$$n^2 = 1 + \chi = 1 + \chi^{(1)} + 3\chi^{(3)}\left|E(\omega)\right|^2 \tag{2.32}$$

Through this relation, the refractive index can be related to the intensity of the light as,

$$n = n_0 + n_2 I \tag{2.33}$$

With I, the intensity of the light given by,

$$I = 2n_0\epsilon_0 c\,|E(\omega)|^2 \tag{2.34}$$

Since the nonlinear susceptibility is much smaller than the linear part, we can use the approximation $n = (1+\chi)^{\frac{1}{2}} = (1+\chi+\chi_{NL})^{\frac{1}{2}} = n_0(1+\frac{1}{2n_0^2}\chi_{NL})$, that gives us the nonlinear index of refraction as,

$$n_2 = \frac{3}{4n_0^2\epsilon_0 c}\chi^{(3)} \tag{2.35}$$

The above analysis reflects the modification of the refractive index at the frequency of a wave due to itself. It is therefore termed as self phase modulation where we observe a change in the refractive index and hence, the phase as the wave propagates through the medium.

If we now look at the case of two waves, one intense and its effects on the refractive index at another frequency carried by a second wave which may or may not be intense, we can observe the cross phase modulation effect where an intense wave affects the index and therefore the phase of another wave at a different frequency. Here we assume the intense wave to be at a frequency ω and the second wave to be at a frequency ω'. If we combine all the terms of the form $\omega' = \omega' + \omega - \omega$ we get the third order nonlinear susceptibility of this interaction to be,

$$P^{(3)}(\omega') = 6\epsilon_0\chi^{(3)}(\omega' = \omega' + \omega - \omega)[E(\omega) \cdot E^*(\omega)]E(\omega') \tag{2.36}$$

Following the same analysis as before and using the value of n_2 obtained previously from Eq. 2.35 and following the same analysis, we get $n_{2,XPM} = 2\, n_2$. This implies that the refractive index change induced on a second wave in the case of XPM is twice as strong as that induced in the case of SPM.

The change in refractive index locally due to the intensity results in a change in the phase of a wave as it propagates through the medium. So in addition to the phase due to the linear term in the refractive index, the wave picks up an additional nonlinear phase as it propagates over a distance L.

$$n(\omega, I) = n_0(\omega) + n_2 I \tag{2.37}$$

$$\phi_{\text{SPM}} = \frac{2\pi}{\lambda}\, n_2\, I\, L \tag{2.38}$$

$$\phi_{\text{XPM}} = 2\,\frac{2\pi}{\lambda}\, n_2\, I\, L \tag{2.39}$$

We introduce a nonlinear parameter γ following the treatment in [4, 7] that we will use throughout this dissertation which includes the nonlinear index as well as the effective area of the waveguide (or fiber / beam more generally).

$$\gamma = \frac{2\pi n_2}{\lambda A_{\text{eff}}} = \frac{\omega n_2}{c A_{\text{eff}}} \tag{2.40}$$

This also allows the nonlinear phase due to the self- and cross-phase modulation to be expressed in terms of the power P as,

$$\phi_{\text{SPM}} = \gamma P L \tag{2.41}$$

$$\phi_{\text{XPM}} = 2\gamma P L \tag{2.42}$$

As we can see from Eq. 2.35, the value of n_2 is very small as compared to the linear refractive index of a material, however in the presence of an intense field, the product $n_2\ I$ will be non-negligible and will affect the refractive index of the material locally. We will see how this affects the dynamics of counter-rotating solitons in a cavity in Chapter 5.

2.4 Four wave mixing

Four Wave mixing is another process that is allowed due to the presence of a third order nonlinearity in a material. As mentioned above in Section 2.2 the four wave mixing process, as the name states, involves four frequency components, ω_{p1} and ω_{p2} are the two pump frequencies and ω_s is the signal frequency. In the FWM process, two photons at ω_{p1} and ω_{p2} are annihilated to create photons at ω_s and a new frequency ω_i. As we can see from the energy level diagram in Fig. 2.2, energy conservation dictates that the idler frequency is given by $\omega_i = \omega_{p1} + \omega_{p2} - \omega_s$.

When we have a single pump wave ($\omega_{p1} = \omega_{p2} = \omega_p$) we have a degenerate FWM process where the signal and idler frequencies are offset by $\delta\omega$ on either side of the pump wave to preserve the energy conservation relation ($\omega_s = \omega_p + \delta\omega$ and $\omega_i = \omega_p - \delta\omega$). From the wave equation (Eq. 2.7) and considering the nonlinear effects on the polarization as shown in Section 2.2, we

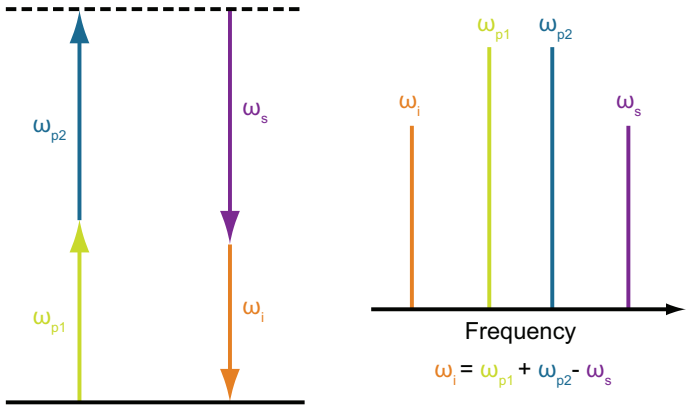

Figure 2.2: FWM energy level diagram with the two pump fields ω_{p1} and ω_{p2} and the signal and idler fields ω_s and ω_i. The two pump photons are annihilated to create signal and idler photons. Under the right phase matching conditions, the signal and idler waves see parametric amplification.

can look at the effects of the nonlinear interaction between the pump, signal and idler waves as they propagate in a direction z along a material using coupled amplitude equations that look at the evolution of the amplitudes (A_p, A_s, A_i) of the plane wave solutions to the wave equation. Here, the amplitudes are assumed to be slowly varying with time and this assumption allows for them to have a purely $A(z)$ dependence in these equations. The pump power is assumed to be undepleted and the signal and idler powers are assumed to be lower than the pump. This allows us to consider only the SPM and XPM terms due to the pump on the pump, signal, and idler waves. Additionally, the FWM interaction term only includes the power transfer from the pump photons to the signal or idler photon.

$$\frac{dA_p}{dz} = -\frac{\alpha_p}{2}A_p + i\gamma\left|A_p\right|^2 A_p \tag{2.43}$$

$$\frac{dA_s}{dz} = -\frac{\alpha_s}{2}A_s + i2\gamma\left|A_p\right|^2 A_s + i\gamma A_p^2 A_i^* e^{-i\Delta\beta z} \tag{2.44}$$

$$\frac{dA_i}{dz} = -\frac{\alpha_i}{2}A_i + i2\gamma\left|A_p\right|^2 A_i + i\gamma A_p^2 A_s^* e^{-i\Delta\beta z} \tag{2.45}$$

The pump evolution, Eq. 2.43 contains a linear loss term and a SPM term. The pump is assumed to be undepleted in the FWM process and hence there is no energy transfer term. The signal evolution, Eq. 2.44, and idler evolution, Eq. 2.45, on the other hand have a linear loss term, a term for the XPM from the pump, as well as a FWM energy transfer term. The FWM term has a phase difference $\Delta\beta$ that arises from the fact that the pump, signal and idler photons in the FWM process travel at different speeds due to differences in the refractive index of the material as we have discussed before. The propagation constant is defined based on the effective index of the waveguide as $\beta = \frac{\omega n_{\text{eff}}(\omega)}{c}$. We will discuss the propagation constant and other properties of the waveguides in greater detail in Chapter 3.

$$\Delta\beta = 2\beta_p - \beta_s - \beta_i \tag{2.46}$$

We perform a Taylor expansion of the propagation constant about the pump frequency, with β_1 and β_2 being the first and second derivatives of the propagation constant with respect to the frequency.

$$\beta_p = \frac{\omega_p n_e(\omega_p)}{c} \tag{2.47}$$

$$\beta_s = \frac{\omega_p n_e(\omega_p)}{c} + \beta_1(\omega_s - \omega_p) + \frac{1}{2}\beta_2(\omega_s - \omega_p)^2 \tag{2.48}$$

$$\beta_i = \frac{\omega_p n_e(\omega_p)}{c} + \beta_1(\omega_i - \omega_p) + \frac{1}{2}\beta_2(\omega_i - \omega_p)^2 \tag{2.49}$$

Putting these together, the phase mismatch due to dispersion comes out to be $\Delta\beta \approx \beta_2\delta\omega^2$. The total phase mismatch is given by this phase mismatch due to dispersion and the phase accrued by the pump wave due to the nonlinear

phase shift.

$$\kappa = 2\gamma P + \Delta\beta \tag{2.50}$$

Since the nonlinear phase is always positive, the $\Delta\beta$ term has to be negative which means that the β_2 has to have a negative value. This implies that the waveguide needs to have an anomalous group velocity dispersion (GVD) at the pump frequency. We will see in Chapter 3 how such an anomalous GVD is achieved.

Modulation Instability is a process by which a small perturbation to a intense continuous wave (CW) field results in amplification of sidebands on either side of the intense pump field. This results in the break up of the CW field into a series of pulses modulated at the frequency separation to the generated sidebands. Power is transferred from the pump to the sidebands through FWM and by solving the nonlinear Schrödinger equation including the dispersion and Kerr nonlinearity terms, the gain for this process is expressed as [7],

$$g = \sqrt{(\gamma P)^2 - \kappa^2/4} \tag{2.51}$$

$$= \sqrt{\gamma P \Delta\beta - \Delta\beta^2/4} \tag{2.52}$$

For silicon nitride, which is the nonlinear material used in this dissertation, we use $n_2 = 2.5 \times 10^{-19}\ \frac{\mathrm{m}^2}{\mathrm{W}}$ based on prior literature [8–10], we use an effective area of $A_{\text{eff}} = 1 \times 10^{-12}\ \mathrm{m}^2$ (which would imply a waveguide cross section on the order of 1 μm $\times$ 1 μm), and a pump wavelength of 1560 nm. These numbers result in a value of $\gamma \approx 1\ \mathrm{W}^{-1}\mathrm{m}^{-1}$ based on Eq. 2.40. A typical value for β_2

for the waveguides used in this dissertation at this pump wavelength is around $\beta_2 = -100$ ps^2/ km. We plot the gain per meter of propagation for these cases over a wavelength range spanning 100 nm around the pump wavelength. To show the variation of the gain profile as the dispersion is varied we pick two values of $\beta_2 = -100$ ps^2/km and $\beta_2 = -50$ ps^2/km and two pump power values $P = 10$ W and $P = 20$ W. This provides some intuition as to how the gain changes as a result of the variation of these parameters as can be seen in Fig. 2.3. A smaller anomalous GVD at the same power results in pushing the gain peaks further out from the pump in frequency while maintaining the same peak gain value. On the other hand, as we would expect from a nonlinear process that clearly scales with pump power, increasing the pump power results in a higher gain.

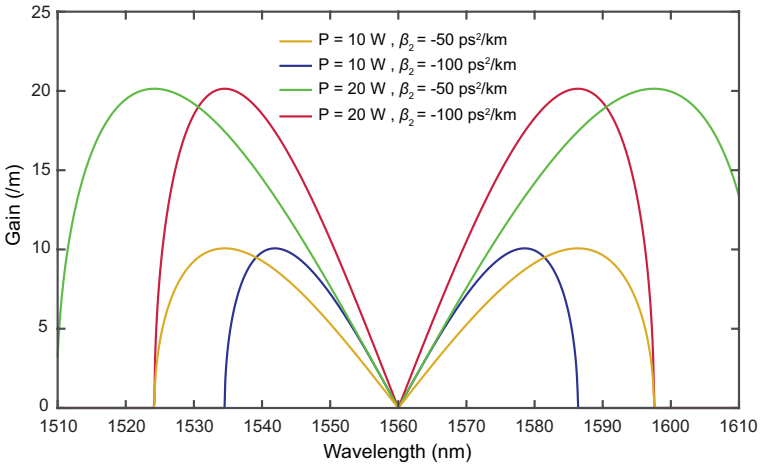

Figure 2.3: FWM Gain variation with wavelength around the pump wavelength for various pump power and dispersion values. The selected pump power values of P = 10,20 W and group velocity dispersion β_2 = -50,-100 ps^2/km are typical for the waveguides used in this dissertation.

These trends in gain for the modulation instability process will dictate some of the choices of waveguide cross section made for devices in this dissertation. When the parametric gain for the modulation instability exceeds the waveguide

loss, we will see parametric amplification of the signal and idler as the waves propagate through the waveguide resulting in the formation of primary sidebands around the pump frequency. Building resonant structures around the gain medium recirculates the waves and allows for enhancement of the powers within the resonant structure. By building resonant structures, we ensure that the input pump power to the resonant structure doesn't need to be as high as the 10 or 20 W that we show in Fig. 2.3. The resonant enhancement of the intracavity power will allow for a much lower input power to be enhanced to these levels and we will be able to see gain within the cavity for the FWM process. The cavity imposes an additional constraint on the frequencies of the pump, signal and idler waves in that they all have to be on resonance with one of the longitudinal modes of the cavity in order for the FWM process to occur efficiently. As we will see in Chapter 3, silicon nitride microresonators are an ideal cavity to resonantly enhance the FWM gain. Such a resonantly enhanced system is called an Optical Parametric Oscillator (OPO) and the first demonstration of such an OPO was in Lithium Niobate ($LiNbO_3$) [11]. When the gain per cavity round trip exceeds the round trip losses, the OPO operates above threshold and we can observe the gain at the signal and idler frequencies corresponding to the peak of the modulation instability gain. We will see in Chapter 4 how as the pump is tuned into resonance with the microresonator cavity, signal and idler waves are generated seeded by vacuum fluctuations and rise in power at the peak of the FWM gain determined by the waveguide dispersion and initiate the frequency comb and cavity soliton generation process through modulation instability.

2.5 Optical frequency combs

Optical frequency combs (OFC) represent a significant technological advance in the last two decades. The development of OFC technology has led to the application of these frequency combs to a multitude of fields of study. As the name implies, an optical frequency comb consists of discrete frequency components that are equally spaced in frequency akin to a comb. The spacing between the comb lines is Δf. If we look at the time domain picture, the frequency comb resembles a series of pulses separated from each other by $\frac{1}{\Delta f}$. This becomes fairly obvious if we look at the Fourier transform of a series of equally spaced components. The phase slippage between the carrier wave and the envelope of the pulses or the carrier-envelope-phase (CEP), ϕ_{cep}, results in an instantaneous frequency called the carrier envelope offset frequency, $f_{\text{ceo}} = \frac{d\phi_{\text{cep}}}{dt}$. The comb spectrum with the comb spacing Δf and this offset frequency f_{ceo} is shown in Fig. 2.4. The offset frequency shifts the entire comb spectrum and consequently the frequency f_{m} of the m$^{\text{th}}$ comb line is given by,

$$f_{\text{m}} = f_{\text{ceo}} + m \times \Delta f \tag{2.53}$$

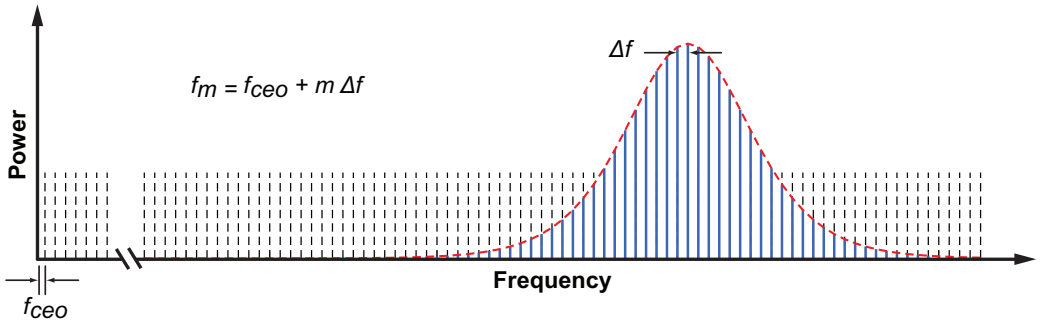

Figure 2.4: A representative comb spectrum with the comb spacing Δf and offset frequency f_{CEO}. The comb lines are in the optical frequency domain.

The start of optical frequency comb technology can be considered to be the first modelocked laser [12] where a He-Ne laser was modelocked by using a synchronous intracavity modulation. In this case the spectrum of the laser already looks like a comb. Indeed, for modelocked lasers, the spectral components follow the $f_{\mathrm{m}} = f_{\mathrm{ceo}} + m \times f_{\mathrm{rep}}$ relation where f_{rep} is the repetition frequency of the pulses from the laser. Extending these lasers to be called frequency combs can be said to require having precise control over the f_{rep} and f_{ceo} that allows for a significant increase in the precision to which the frequencies of the comb are known through Eq. 2.53 [13]. Having this higher level of precision in the frequencies of the comb enables applications such as precise frequency metrology that is of use to making optical clocks. This level of precision has allowed spectroscopy of a Cesium transition [14] and enabled measurements of large frequency differences undetectable well beyond the bandwidth of photodetectors using different modes of a comb [15]. This led to the development of a frequency comb based optical clock by referencing a frequency comb to a single $^{199}Hg^{+}$ ion [16]. Precision spectroscopic measurements aided by frequency combs of several other important atomic and molecular transitions including Rb [17], I_2 [18, 19], Ca [20] among other have been subsequently performed. These frequency combs probe well characterized atomic and molecular transitions and transfer the precision to which the transitions are known onto the modes of the comb that can then be used for frequency metrology at other frequencies distant from the transition [21].

These comb sources rely upon precise control of the f_{rep} and f_{ceo}. This is achieved by a technique known as self-referencing of the combs using $f - 2f$ interferometry [22] that allows for detection and stabilization of the CEO frequency f_{ceo}. Here the $2\mathrm{m}^{\mathrm{th}}$ mode, f_{2m}, of a comb is mixed with a frequency

doubled m$^{\text{th}}$ mode, $2f_m$. The difference between these two frequencies results in a beat note at f_{beat},

$$f_{\text{beat}} = 2(f_{\text{ceo}} + m \times f_{\text{rep}}) - (f_{\text{ceo}} + 2m \times f_{\text{rep}}) = f_{\text{ceo}} \tag{2.54}$$

Additionally based on the broad spectral coverage, precision in frequencies and spacing between the frequency comb lines that typically lies in the microwave frequency range, several other applications have been explored such as frequency comb spectroscopy of various atomic and molecular species [23–27], astronomical spectrograph calibration using the lines of the comb to act as a frequency ruler for star light from a telescope [28–30], low phase noise microwave frequency generation [31, 32], optical arbitrary waveform generation [33, 34] among many others.

The f_{rep} can be measured directly or indirectly and in this way each of the comb modes are known to the precision that the f_{ceo} and f_{rep} are known. Typically the femtosecond modelocked lasers that are used in the results above do not span a octave in frequency that is be required for the $f - 2f$ interferometry. The spectrum of the mode locked lasers is broadened into a supercontinuum through nonlinear effects in microstructured fiber [17] or other nonlinear fibers / materials as can be see in Fig. 2.5 to get the spectral coverage that includes the f_m and f_{2m} modes for some m. We include a typical schematic for the spectral broadening approach used in these initial frequency comb experiments along with an outline of the $f - 2f$ interferometry scheme to detect f_{ceo} in Fig. 2.5.

Over the last decade another approach to frequency comb generation has seen a significant amount of research. This is frequency comb generation using

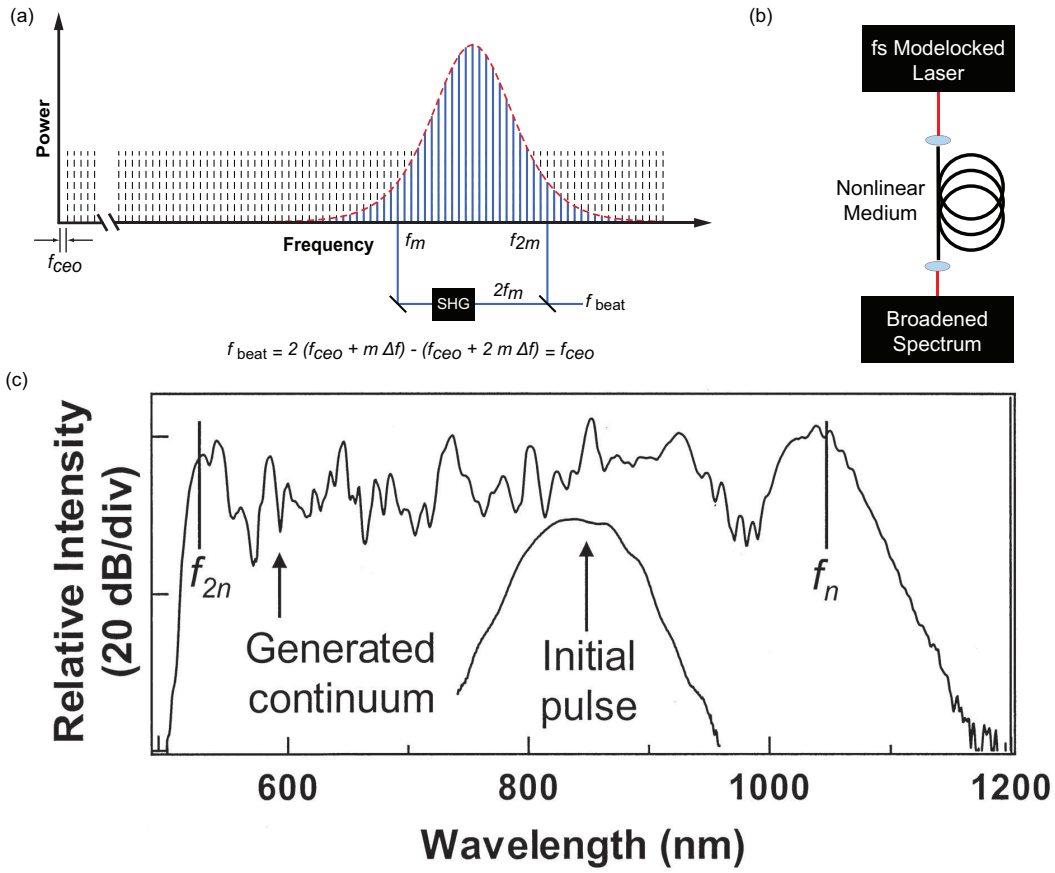

Figure 2.5: (a) A schematic for the $f-2f$ interferometry to detect the f_{ceo}. The 2m$^{\text{th}}$ mode, f_{2m}, of a comb is mixed with a frequency doubled m$^{\text{th}}$ mode, $2f_m$ to detect the f_{ceo} (b) A schematic of a setup typically used for spectral broadening of modelocked lasers to a supercontinuum spanning an octave covering the f_m and f_{2m} modes. (c) Spectrum of the mode locked lasers after broadening through nonlinear effects in microstructured fiber (Adapted from [17])

the Kerr nonlinearity in waveguides. These photonic chip based combs rely on some of the nonlinear processes that we have discussed in this dissertation previously and enable the generation of compact frequency comb sources that can be used in similar applications as the solid state laser based comb sources described above [35]. Photonic Chip based combs use two approaches to generating broadband frequency comb spectra, supercontinuum generation in waveguides pumped by short pulses, or comb generation through Kerr nonlinearity in microresonators. The supercontinuum generation approach is similar to the

approached used by solid state laser based frequency combs we have discussed previously as shown in Fig. 2.5(b) where the nonlinear material is the waveguide in this case.

Photonic chip based combs based on microresonators rely on the process of four wave mixing to achieve frequency conversion between the various comb lines. The one distict difference in this approach and the supercontinuum based approach is that these frequency combs are pumped by a CW pump laser instead of a modelocked femtosecond laser. When the pump is close to resonance with the modes of the ring resonator some of the pump power couples into the microresonator. This causes initial sidebands to be generated at the peaks of the modulation instability gain depending on the dispersion and power of the pump laser coupled into the microresonator as seen in Fig. 2.3. Subsequently as the pump is moved closer to being on resonance even more pump power couples into the microresonator, these sidebands grow in strength as more power is transferred from the pump to the sidebands. The sidebands then act as secondary pumps and allow for frequency conversion to other modes of the resonator. The comb generation process follows non-trivial nonlinear dynamic evolution through degenerate and non-degenerate four wave mixing to eventually generate a frequency comb covering a wide optical bandwidth [36] as outlined in Fig. 2.6. A more complete description of the resonance conditions are given in Chapter 3 and a discussion on the dependence of the frequency comb generation dynamics with respect to the frequency offset of the pump from the resonance frequency of the cavity, the pump-cavity detuning, is discussed in Chapter 4 and 5.

Supercontinuum generation in waveguides has been demonstrated in vari-

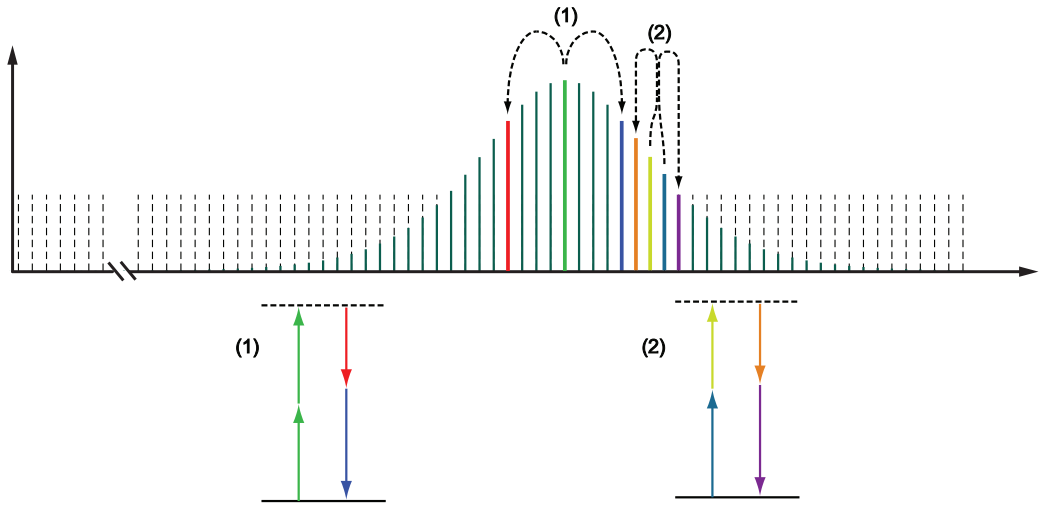

Figure 2.6: The nonlinear dynamical evolution of the frequency comb generation process sees contributions from degenerate and non-degenerate four wave mixing to reach a state with a filled in frequency comb spectrum over a broad bandwidth.

ous material platforms including Silicon [37–39], Silicon Nitride [40–44], Germanium [45], Lithium Niobate [46, 47], Aluminum Nitride [48]. These results have been able to generate coherent octave spanning, self-referenced spectra similar the case of fiber as a nonlinear medium and have demonstrated comparable frequency precision to those schemes in a more compact footprint with integrated waveguides.

The first demonstration of frequency comb generation in a microresonator was shown in silica microtoroids [49]. With a microtoroidal cavity of radius 75 μm, a frequency comb spanning nearly 300 nm in optical bandwidth was generated using a CW pump at 1550 nm. The spacing between the comb lines corresponded to the longitudinal modes of the microtoroidal cavity and is approximately 7 nm. We will look at the mode spacing of these microresonators in detail in Chapter 3. After this first demonstration in silica microtoroids, the field of microresonator based frequency combs has grown rapidly. Frequency combs have been demonstrated in various material platforms including Silica [49], Sil-

icon [50], Diamond [51], Lithium Niobate [52], Aluminum Nitride [53], Hydex [54], Aluminum Gallium Arsenide [55], Calcium Fluoride [56, 57], Magnesium Fluoride [58], Gallium Phosphide [59] and Silicon Nitride [60–64].

These early demonstrations of frequency combs in various materials established the understanding of comb generation in microresonators through nonlinear processes. However in most of these cases, since the complex nonlinear dynamic evolution of the frequency combs with detuning was not well understood, the generated spectra were incoherent which limited the frequency precision of the comb lines. In addition, the phase relationship between the different frequency components remained inconsistent and did not allow for modelocking of the combs and the formation of short pulses. In Chapter 4 we will delve deeper into work done to gain more insight into the detuning dependent evolution of frequency combs to soliton modelocked states and how the work in this dissertation advances thermal control of microresonator chip based frequency combs.

CHAPTER 3

INTEGRATED PHOTONICS

Historically, the invention of optical fibers can be pointed to as the singular event that led to the revolution in optical communications. The invention of the optical fiber gave the ability to beat the effects of diffraction and be able to carry light and over very long distances [65] with extremely low losses [66]. As optical data communication speeds have increased to keep up with ever increasing needs for data, the length scales over which electric interconnects see high enough loss to make them non viable has dropped from the kilometer scale to the centimeter scale and beyond. The losses in the metal interconnects arise due to skin effect losses that limit the flow of electrons close to the surface of the interconnect within the skin depth as the frequency is increased. This reduces the effective cross section of the interconnect and increases the losses due to Joule heating [67]. At the centimeter and sub centimeter length scale, on chip optical interconnects will be required as data rates continue to grow. Silicon Photonics is an enabling technology for these optical interconnects [68–70]. Silicon and other materials like silicon nitride, silicon dioxide have already found use in standard Complimentary Metal-Oxide-Semiconductor (CMOS) foundry processes for chip based electronics. Fiber based technologies that have been used for optical communications have meant a maturation in the affiliated technologies such as lasers, modulators and high bandwidth photodetectors in the telecommunications wavelength bands from 1260-1360 nm (Original,O-band), 1530-1565 nm (Conventional,C-band), 1565-1625 nm (Long Wavelength,L-band) and other less common ones outside these wavelength windows. Silicon, silicon nitride and silicon dioxide are all transparent to light in these telecommunications bands which makes them suitable for the fabrication of chip based optical

devices such as those used in this dissertation. As we saw in Chapter 2, most materials exhibit nonlinear behavior. However, they do so in the very specific conditions of high intensity incident fields and only when the material dispersion allows for the phase matching of the nonlinear optical processes to observe parametric gain. We also noted that enhancement in a resonant structure would allow us to observe optical parametric oscillation at lower pump powers. Silicon photonics is uniquely positioned to solve all of these challenges that are imposed by the theoretical considerations of nonlinear optics. This makes silicon photonic devices an ideal platform to control and manipulate light and observe nonlinear effects at telecommunication wavelength bands.

In this chapter we will look at some of the tools that are crucial to the design of devices that can then be fabricated using well established processes for nanophotonic devices developed by the Lipson Nanophotonic Group at Cornell and Columbia University [71,72].

3.1 Optical waveguides

If we look at the guiding of light using the ray picture of wave propagation, both optical fibers and silicon photonic waveguides confine light within the 'core' or the guiding material, using the property of light known as total internal reflection. This behavior of light occurs at an interface between two materials where light is incident upon the interface from the material with a higher refractive index ($n_1 > n_2$). It was first observed in streams of water and the first demonstration of light guided within a water stream using TIR was shown by John Tyndall with water serving as the 'core' and the surrounding air as the 'cladding' mate-

rial [73]. The law of reflection, Eq. 3.1, and the Snell's law of refraction, Eq. 3.2, govern the propagation of light in the ray picture.

$$\theta_i = \theta_r \tag{3.1}$$

$$n_1 \sin(\theta_1) = n_2 \sin(\theta_2) \tag{3.2}$$

In the case where $n_1 > n_2$, above a critical angle θ_c none of the light will be refracted into the outer material and all of the light will be reflected back. This angle can be calculated from Snell's law by setting the angle of refraction to $\pi/2$ indicating that the light doesn't propagate into the cladding medium. From this we can get θ_c as,

$$\theta_c = \sin^{-1}(\frac{n_2}{n_1}) \tag{3.3}$$

As we can see in Fig. 3.1(b), light at an angle $\theta_1 < \theta_c$ is not guided in the waveguide and leaks into the cladding when it reflects off the interface between the core and cladding. With each successive reflection some of the light in the unguided wave loses its power to the cladding. On the other hand, light at the critical angle θ_c is guided within the waveguide and can propagate through the waveguide with lower losses.

Studying the guiding of light using a mode picture gives us deeper understanding of the propagation of light in a waveguide and how this varies with frequency. As shown in Fig. 3.1(a), for a given cross section h$\times$w of the waveguide we can solve for the eigenmodes of the waveguide using the Maxwell's equations, Eqs. 2.1-2.4, and boundary conditions at the interface between the

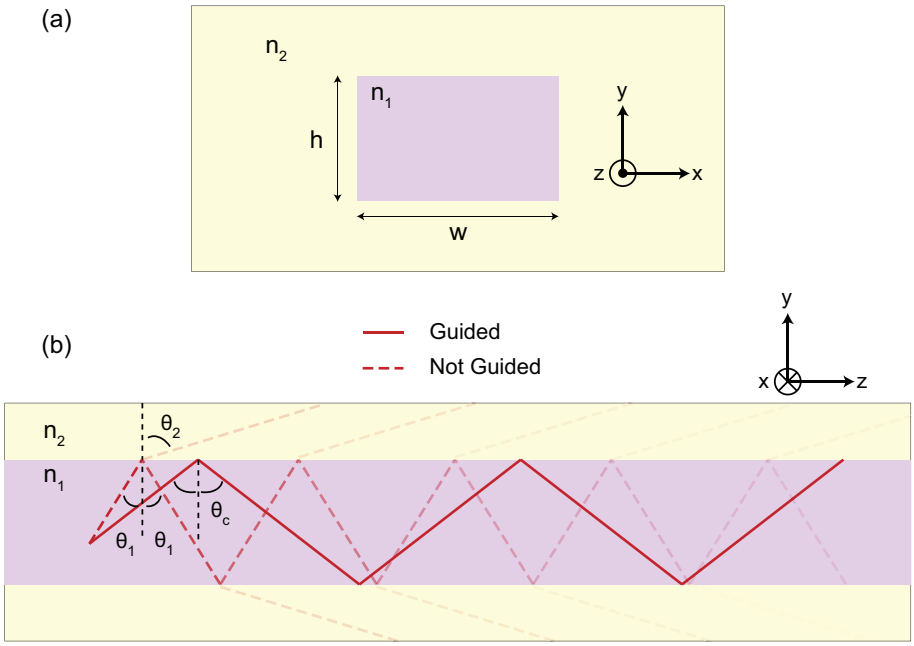

Figure 3.1: (a) A cross sectional view of a waveguide with core index n_1 and cladding index n_2. (b) Side view of the waveguide showing guided light (solid, red) traveling in the waveguide at an angle of incidence θ_c that allows TIR, and unguided light (dashed, red) at a smaller angle of incidence θ_1 that leaks into the cladding.

core and cladding with refractive indices n_1 and n_2. The eigenmodes give us the propagation constant for a given mode as a function of frequency. This gives us the effective index of the waveguide n_{eff} that lies in between n_1 and n_2. If the n_{eff} is closer to n_1 it implies that the mode is more confined within the core, whereas if it is closer to n_2 it implies that the mode is less confined within the core and leaks into the cladding. n_{eff} also gives us the group velocity dispersion of the waveguide that can be used to determine the gain that results in modulation instability that initiates the frequency comb generation process as was discussed previously in Section 2.4.

The transverse electric (TE) modes have their electric field $\vec{E}$ oriented along the x axis. The magnetic field $\vec{H}$ and the wave vector $\vec{k}$, are orthogonal to each other and to the electric field and are oriented in the plane of Fig. 3.1(b), the y-z

plane. The transverse magnetic (TM) modes have their magnetic field oriented along the x axis and the electric field and wave vector lie in the y-z plane. The conditions on the fields that are required to solve for the TE and TM modes are as follows,

- Tangential component of E and H has to be continuous across the interface between two materials,
- For the TE modes, $E_y = 0$ and $E_z = 0$, as the electric field is oriented in the x direction.
- For the TM modes, $H_y = 0$ and $H_z = 0$, as the magnetic field is oriented in the x direction.

While anayltical solutions for the modes can be found using these boundary conditions, practically using Finite Element Method (FEM) based mode solvers becomes a computationally less intensive task. Mode solvers such as the one provided by COMSOL Multiphysics ® [74] can be used to solve for the eigenmodes of the waveguide. Using the COMSOL mode solver which incorporates these conditions along with the wave equation derived from Maxwell's equations previously, we get field distribution eigenmodes and the effective waveguide index n_{eff} as eigenvalues for a waveguide with a given cross section. The distribution of the field for the fundamental TE mode (TE_0) of a waveguide with a cross section 950 $\times$ 1500 nm with the core as Si_3N_4 and cladding as SiO_2 is shown in Fig. 3.2.

For every eigenmode of the waveguide, we have a corresponding eigensolution for the effective waveguide index n_{eff} that leads to a propagation constant β,

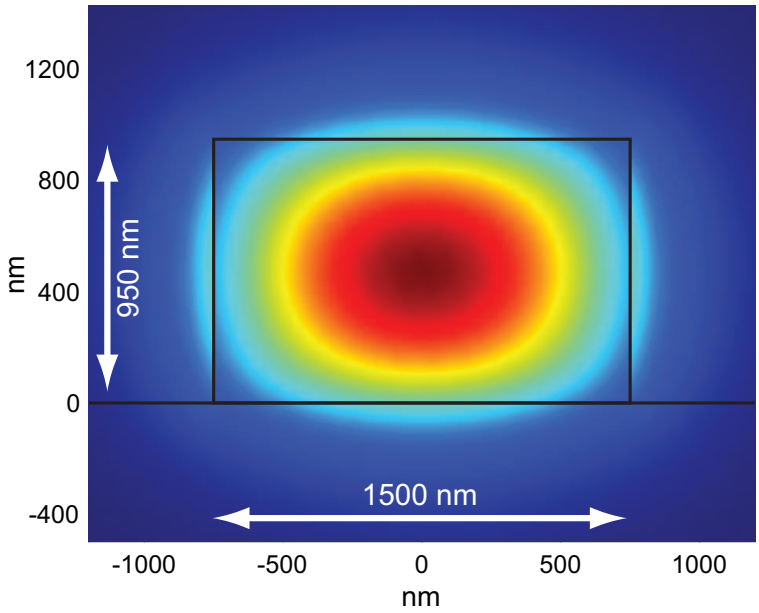

Figure 3.2: The electric field distribution for the TE_0 mode at a wavelength of 1560 nm for a Si_3N_4 waveguide with a SiO_2 cladding and a cross section of 950 $\times$ 1500 nm. Most of the mode remains confined within the Si_3N_4 but there is some leakage of the mode to the cladding SiO_2. $n_{\text{eff}} = 1.8524$ for this cross section.

$$\beta = \frac{\omega n_{\text{eff}}}{c} \tag{3.4}$$

The dispersion of the refractive indices of the core and cladding are incorporated into these calculations through their respective Sellmeier equations, that gives us the dispersion of the effective waveguide index $n_{\text{eff}}(\omega)$. The phase velocity and group velocity are given by the relations,

$$v_p = \frac{\omega}{\beta} \tag{3.5}$$

$$v_g = \frac{\partial \omega}{\partial \beta} \tag{3.6}$$

For a given wavepacket, the phase velocity, v_p, is the velocity at which the

phase of a particular frequency component of the wavepacket propagates whereas the group velocity, v_g, is the velocity at which the envelope of the wavepacket propagates. The group velocity dispersion is the derivative of the inverse of the group velocity and is given by,

$$\text{GVD}(\omega_0) = \frac{\partial}{\partial\omega}\Big(\frac{1}{v_g}\Big)_{\omega=\omega_0} \tag{3.7}$$

$$= \frac{\partial}{\partial\omega}\Big(\frac{\partial\beta}{\partial\omega}\Big)_{\omega=\omega_0} = \Big(\frac{\partial^2\beta}{\partial\omega^2}\Big)_{\omega=\omega_0} = \beta_2 \tag{3.8}$$

We have already discussed in some detail previously how the GVD factors into the parametric gain for the FWM process in Section 2.4. Bulk silicon nitride has a GVD that is normal (i.e. positive β_2) at typical pump wavelengths used in this dissertation of around 1560 nm. Modal dispersion due to the waveguide cross section allows us to compensate for this and achieve a negative value of β_2 at the pump wavelength λ_p = 1560 nm. In Fig. 3.3 β_2 for waveguides with cross sections 950 $\times$ 1500 nm and 730 $\times$ 1500 nm is shown which has a negative value at 1560 nm, a typical pump wavelength used in this dissertation. Throughout this dissertation, we use waveguides with a cross section of 950 $\times$ 1500 nm or 730 $\times$ 1500 nm.

3.2 Ring resonators

In Chapter 2 we looked at how nonlinear effects in materials benefit from high intensities. In the previous section we looked at how high confinement waveguides enhance the intensity of light. This happens when the power carried by the incident light in the form of electromagnetic fields is confined to an ex-

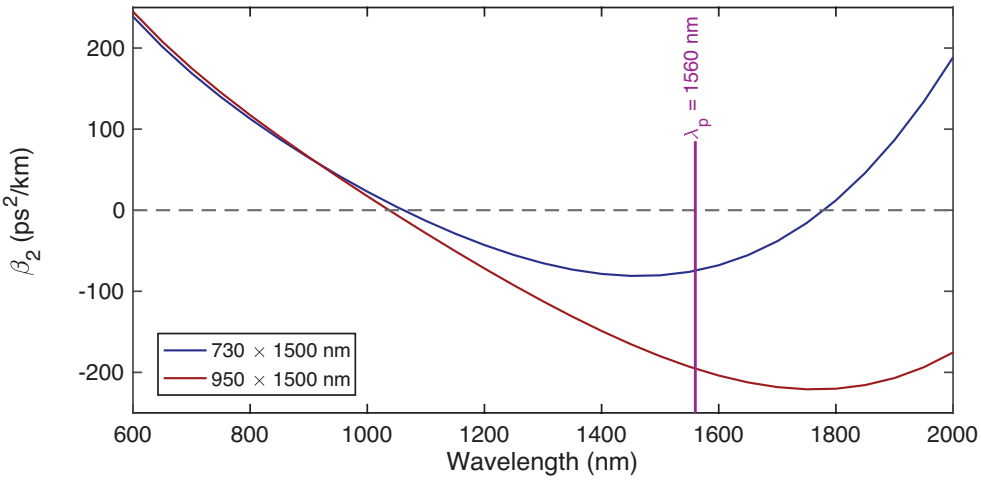

Figure 3.3: Group Velocity Dispersion for waveguides with cross sections 950 × 1500 nm and 730 × 1500 nm. These cross sections both allow for anomalous GVD at our typical pump wavelength λ_p = 1560 nm.

tremely small modal area on the order of 1 μm^2. The intensities achieved within these high confinement waveguides still require a significant amount of power to be carried in the light in order to observe nonlinear frequency conversion. One approach to boosting these powers is by packing a significant portion of the power in a short burst such as an optical pulse. Typically nonlinear interactions in straight waveguides or optical fibers are observed in this manner. The fiber or waveguide with the right dispersion for phase matching of the nonlinear process being studied is pumped with a extremely short optical pulse typically on the femtosecond scale. The high power at the peak of the pulse results in a non-negligible nonlinear response which leads to nonlinear frequency conversion and leads to spectral broadening. The field of optical frequency combs has particularly benefited from the nonlinear spectral broadening in dispersion engineered optical fibers and optical waveguides in several material platforms.

Another way of enhancing the power is by using a cavity to recirculate the power. A cavity results when an optical wave goes over the same path repeat-

edly. In the right conditions, the wave will overlap with itself and add up constructively over successive round trips around the cavity which leads to an enhancement in the field strength and the power within the cavity. Such a condition is called as being on 'resonance' with the cavity. The resonance condition occurs when an integer number of cycles of light at a given frequency exactly fit into one round trip around the cavity which allows for the field to constructively interfere with the input field entering the cavity and add up. Mathematically, this can be described as, the phase accumulated by the light over one round trip should be an integer multiple of 2π,

$$\phi(\omega) = \beta(\omega) \times L = 2\pi m \tag{3.9}$$

Equivalently since $\beta = \omega n_{\text{eff}}/c = 2\pi n_{\text{eff}}/\lambda$ we get the relation,

$$L n_{\text{eff}} = m\lambda \tag{3.10}$$

The evanescent tails of the eigenmodes shown in Fig. 3.2, overlap which leads to coupling of light between the waveguides that depends on the gap between the waveguides g. The coupling constant based on the gap is κ. As we can see in Fig. 3.4, at the coupling region the coupling is κ and the transmission is t. Assuming lossless coupling, $t^2 + \kappa^2 = 1$. The round trip loss is $a = e^{-\alpha L}$ where α is the conventionally used parameter for waveguides, loss per unit length. The transmitted power through the ring, P_{tr}, and the power circulating in the ring, P_{circ} normalized to the input power, are given by the following equations [75],

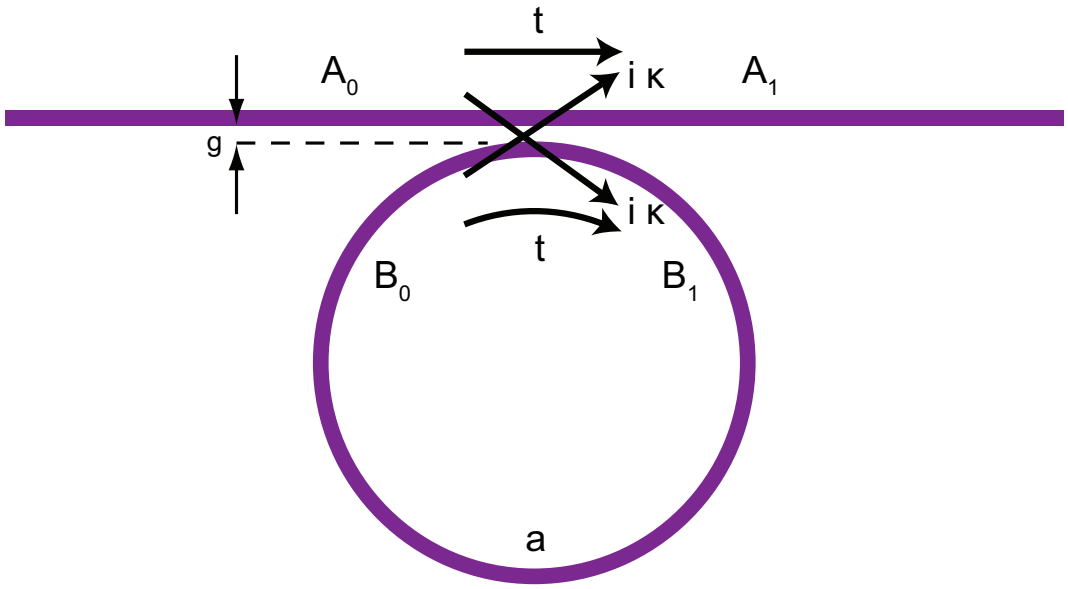

Figure 3.4: Group Velocity Dispersion for waveguides with cross sections 950 × 1500 nm and 730 × 1500 nm. These cross sections both allow for anomalous GVD at our typical pump wavelength λ_p = 1560 nm.

$$P_{tr}(\lambda) = \left|\frac{A_1}{A_0}\right|^2 = \frac{a^2 + t^2 - 2at\cos(\beta L)}{1 + a^2t^2 - 2at\cos(\beta L)} \tag{3.11}$$

$$P_{circ}(\lambda) = \left|\frac{B_0}{A_0}\right|^2 = \frac{a^2\,\kappa^2}{1 + a^2t^2 - 2at\cos(\beta L)} \tag{3.12}$$

From these equations it is clear to see that the circulating power will be maximum, when the $\cos(\beta L)$ is maximum and this directly leads us to the resonance condition we discussed earlier in Eq. 3.9. The circulating power and transmitted power are normalized to the input power $|A_0|$.

We use the propagation constant, β that we obtained from COMSOL FEM simulations for the 730 × 1500 nm waveguide and assume a ring with a radius of 100 μm to look at the transmission of the ring resonator built using such a geometry. Critical coupling is achieved when the round trip loss a equals the transmission at the coupling region t that results in the transmission on reso-

nance dropping exactly to 0. We assume exaggerated linear losses of 20 dB/m and a corresponding $\kappa = 0.34$ that leads to near critical coupling for a resonator with a radius of 100 μm to better illustrate the resonance feature. For this case, as we see in Fig. 3.5, we see a resonance condition at 1559.14 nm and 1561.00 nm. Typical losses for silicon nitride waveguides fabricated using the processes used for devices in this dissertation are 4.2 dB/m [71], or 0.8 dB/m [72] for an optimized process to reduce sidewall roughness of the waveguides and limit scattering losses.

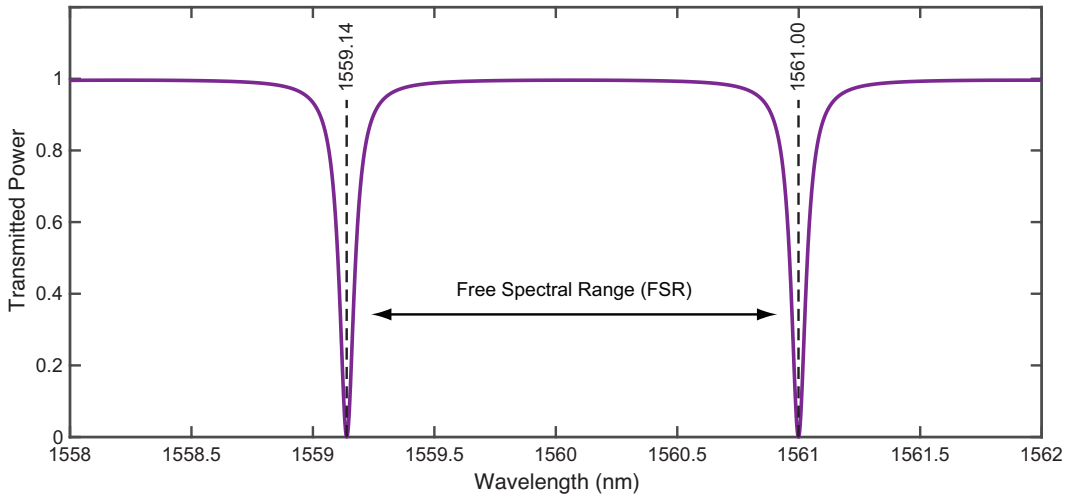

Figure 3.5: Resonances for a ring resonator with radius 100 μm for a waveguide with a cross section of 730 $\times$ 1500 nm. We observe resonances at 1559.14 nm and 1561.00 nm.

The spacing between the resonances is the free spectral range (FSR) of the resonator. In this dissertation we use a typical FSR of 200 GHz.

3.3 Silicon nitride as a nonlinear optical material

Nonlinear interactions can be observed in a variety of materials with varying nonlinearities. Materials with higher nonlinearity show nonlinear effects at very

low light intensities and conversely materials with lower nonlinearities at extremely high intensities. Some of the strongest nonlinearities can be observed in alkali vapors such as Rubidium with extremely low intensities as low as a few photons [76]. Noble gases on the other hand show extremely low nonlinearities, yet high harmonic generation can be demonstrated in these gases with extremely high power lasers as in weakly ionised Argon gas [77]. Both these extremes require highly controlled systems with precise control of pressures or operation in the presence of a vacuum.

To observe nonlinearities at moderate powers in compact form factors with relatively less complex systems a significant amount of work has been done in silica glass and fiber [4, 7]. Waveguides made using various materials represent a similar platform for observing nonlinear effects at moderate intensities. Complementary metal-oxide-semiconductor (CMOS) technologies have matured significantly due to their use in the large scale electronic chip fabrication process [10]. The primary material used in these processes is Silicon (c-Si) that has a typical refractive index of 3.48 at 1550 nm in the telecommunications C-band. Silica (SiO_2) has a refractive index of 1.45 at 1550 nm. The high index contrast allows for very tight confinement in waveguide geometries [78]. The nonlinear refractive index of silicon at telecom wavelengths is $4 \times 10^{-18}\text{m}^2/\text{W}$ [79]. This is significantly higher than the nonlinear refractive index of silica that is $2.6 \times 10^{-20}\text{m}^2/\text{W}$ that leads to much higher nonlinearity ($\gamma = 300\text{m}^{-1}\text{W}^{-1}$) [10]. However one significant drawback of silicon based integrated photonic devices arises from the two photon absorption process. The bandgap of silicon is 1.17 eV that corresponds to a wavelength of 1060 nm [80]. This means that at 1550 nm two photon absorption (TPA) is observed. TPA limits the nonlinear effects and is detrimental to FWM process that leads to broad-

band frequency comb generation [81]. Thus, pumping a silicon ring resonator in the telecommunications wavelength range makes it difficult to generate a frequency comb. Indeed, by pumping beyond the two photon absorption wavelength, in the mid infrared, frequency combs have been generated in silicon microresonators [50, 82]. Silicon resonators are an ideal material platform for frequency comb generation in the mid infrared.

Silica can also be formed into resonant structures on a micron scale to generate frequency combs due to its nonlinearity. One significant advantage of using silica microresonators is the ability to get extremely pure crystalline silica resonators with low losses. This compensates for the lower nonlinearity as compared to silicon by having integrated microresonators with quality factors over 100×10^6, due to the lower loss [83]. Frequency combs can be generated in these silica microtoroids, and indeed the first demonstration of a continuous wave pumped Kerr nonlinearity based frequency comb was in these resonators [49]. Silica waveguides and resonators exhibit strong Raman gain arising from the vibrational levels of the crystal structure [84]. Raman gain allows for observation of such phenomena as stokes soliton generation [85], and Raman lasing [86] in silica microresonators, but it also has detrimental effects that can limit the bandwidth of cavity solitons generated in such a device [87]. The bandgap of silica is 9 eV that corresponds to 138 nm and means that TPA is negligible at telecom wavelengths [88].

Silicon nitride is a material also used extensively in the microelectronics fabrication process as a passivation layer acting as a diffusion barrier preventing water molecules form interacting with the circuits to avoid corrosion [89] or as an etch mask [75]. This has meant that significant knowledge of silicon ni-

tride film deposition can be derived from the microelectronics technology and applied to building waveguide and resonator structures. The refractive index of the low pressure chemical vapor deposition (LPCVD) based silicon nitride films used in this dissertation is 1.99 at 1550 nm. This is lower than the refractive index of silicon which leads to lesser confinement of the light when silica is used as a cladding material, but the index contrast is still high enough to allow for significant enhancement of the intensity due to the confinement. The nonlinear index of silicon nitride is $2.5 \times 10^{-19} \frac{\mathrm{m}^2}{\mathrm{W}}$ [8, 9] that is about 10 times higher than that of silica but less than that of silicon. The material shows negligible TPA at telecom wavelengths as the bandgap is 5 eV or 248 nm in wavelength. Low waveguide losses as low as 0.8 dB/m [72], quality factors higher than 10×10^6, high confinement, negligible TPA, high FWM gain and the ability to engineer the dispersion based on the cross section make silicon nitride an ideal material for the generation of optical frequency combs in microresonator devices pumped at telecom wavelengths.

CHAPTER 4

THERMALLY CONTROLLED SOLITON MODELOCKING IN MICRORESONATORS

Frequency combs rely upon the broadband coherence across the generated optical spectrum to enable applications such as frequeny metrology [90], direct frequency comb spectroscopy [91], Dual comb spectroscopy [27, 91–94], ranging [95,96], low phase noise RF signal generation [31,32] and other applications. In order to achieve broadband coherence, in the case of supercontinuum generation based frequency combs, the coherence of the modelocked pump laser is transferred to the broadened spectrum through the nonlinear broadening process utilizing self-phase modulation to compress the pulse in time and broaden the spectrum while minimizing nonlinear processes that degrade the coherence such as modulation instability that is seeded from noise [35, 97].

Microresonator based frequency combs as we saw earlier in Section 2.5, when pumped in the anomalous group velocity dispersion region, rely upon the modulation instability to generate sidebands that initiate the comb generation process. This led to most of the preliminary results in microresonator based frequency combs being high noise and incoherent, but having broadband spectra. It was unclear if such a process seeded from noise through MI would result in the generation of coherent optical spectra. A clearer understanding of the nonlinear dynamical evolution of the frequency comb generation process and how it depends on the dispersion, pump power as well as detuning of the pump laser frequency from the resonance frequency of the microresonator was required to allow microresonator based combs to be used for most applications that required coherence over the optical bandwidth spanned by the comb.

4.1 Modeling of frequency comb evolution

Work done by Lugiato and Lefever in resonant cavities that included a nonlinear material provided the primary basis for understanding of these systems [98]. The evolution of the light as it propagated around the cavity is predicted by a differential equation including the effects of diffraction and self focusing of light due to a third order nonlinearity. In the case where this system is pumped with a plane wave, they predict that the plane wave will spontaneously be converted into a stationary beam with a transverse stripe structure within the cavity under the right conditions of diffraction and self focusing. This system is analogous to microresonators or fiber cavities pumped by a CW pump laser. The CW pump laser is analogous to the plane wave input field, the diffraction is analogous to the dispersion of the waveguide or fiber cavity and the Kerr nonlinearity is analogous to the self focusing nonlinearity. Other terms for linear losses within the cavity, detuning with respect to the cavity mode, and terms for other nonlinear effects that may affect the evolution of the field can be incorporated into the differential equation to predict the evolution of the frequency comb as various parameters are modified. The study of modulation instability in synchronously pumped dispersive and nonlinear cavity predicted the existense of stable temporal dissipative structures in these cavities [99]. A modified Lugiato Lefever equation (LLE) formalism for microresonator and fiber cavities was developed after the preliminary experimental results were demonstrated to better understand these results as well as identify other regimes of operation. The modified Lugiato Lefever equation can include additional terms for effects that can affect the evolution of the comb generation process such as multiphoton absorption [81], Raman gain [100]. The modified LLE takes the form,

$$T_R\frac{\partial E(t,\tau)}{\partial t} = \sqrt{\kappa}\,E_{\text{in}} + \Bigg[-\frac{\alpha}{2}-\frac{\kappa}{2}-i\delta_0+iL\sum_{n\geq 2}\frac{\beta_n}{n!}\Big(i\frac{\partial}{\partial\tau}\Big)^n + i\gamma L\Big(1+\frac{i}{\omega_0}\frac{\partial}{\partial\tau}\Big)\left|E(t,\tau)\right|^2\Bigg]E(t,\tau) \tag{4.1}$$

where $E(t,\tau)$ is the intracavity field, E_{in} is the input pump field with a frequency ω_0, t and τ are slow and fast time axes respectively, with τ referring to the temporal distribution of the field within the cavity at a time t, β_n is the n-th order dispersion term, κ is the transmission at the coupling region, γ is the nonlinear parameter, L is the cavity length, T_r is the round trip time. The LLE predicts a solution that takes the form of hyperbolic secant squared pulses on a CW background. The pulse power is given by the equation,

$$P(t) = P_0\,\text{sech}^2(\frac{t}{\tau_0}) \tag{4.2}$$

where τ_0 is the pulse width of the soliton that is determined by the dispersion and detuning.

The evolution of the intracavity field as the input field and detuning are varied can be studied using the modified LLE and predicts several regimes of operation for microresonator frequency combs. Here, the detuning is defined as the difference between the frequency of the pump and the resonance frequency of the cavity. Blue detuned implies that the pump frequency is higher than the cavity resonance frequency. As the pump is tuned onto resonance from the blue detuned side, first the continuous wave pump field breaks into several pulses through modulation instability due to the generation of sidebands at the MI gain peak. As it is tuned in further, closer to the zero effective detuning these

pulses transition to a chaotic state with the pulses interacting with each other. When the pump crosses the zero detuning point and crosses to the red detuned side the pulses transition to a stable multi-soliton state. Tuning further into the red detuned side the number of solitons in the cavity over one round trip drops till a single soliton survives.

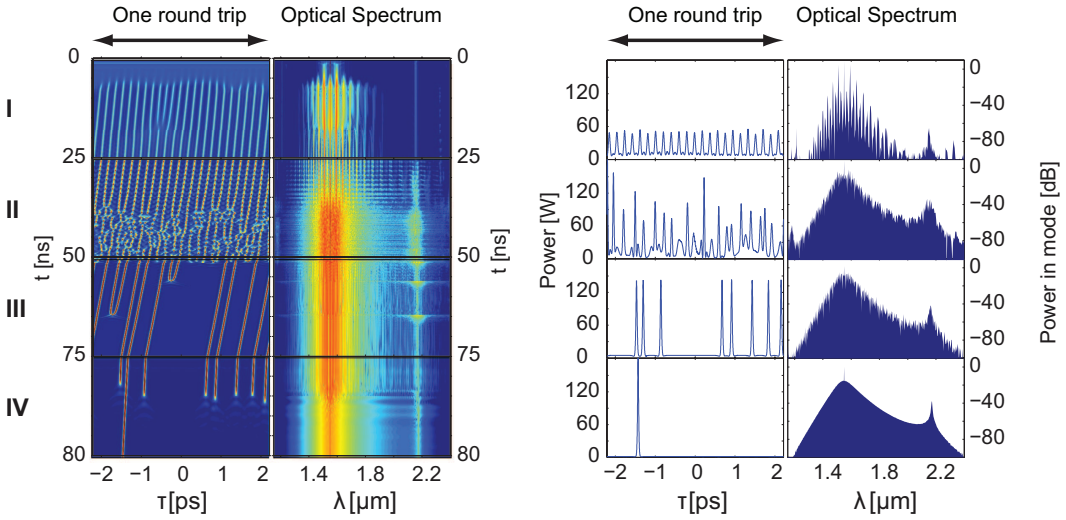

Figure 4.1: Evolution of the comb as the detuning with respect to the resonance frequency is tuned. (I) Modulation instability leads to the CW pump breaking into a series of pulses, in the frequency domain this manifests as sidebands at the peak of the MI gain. (II) The pulses interact in a chaotic state. (III) As the detuning crosses the zero detuning point over to the red detuned side, we see the emergence of multiple stable solitons in the cavity. (IV) Tuning further into the red detuned, a single soliton survives, characterized by a smooth hyperbolic secant spectrum with a CW background. The image is adapted from [101] which uses a 226 GHz ring with a cross section of 725 $\times$ 1650 nm.

As we can see from Fig. 4.1, fine control of the detuning results in the ability to reach a cavity soliton state. In this modelocked state, the phase relationship between the different frequency components of the frequency comb remains constant leading to the formation of pulses. Additionally, it also leads to perfect equidistance of the frequency comb lines with the separation between adjacent comb lines being f_{rep} that corresponds to the repetition rate of the pulses. As we discussed earlier in Section 2.5, the ability to generate coherent broadband spec-

tra enables applications in spectroscopy, low-noise RF generation and ranging.

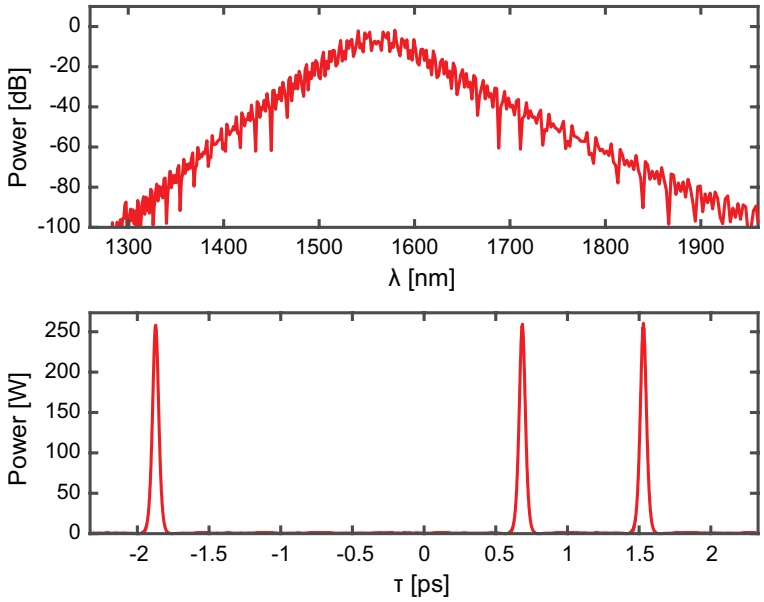

Figure 4.2: A stable three soliton state for a microresonator with radius 120 μm and waveguide cross section 950 $\times$ 1500 nm.

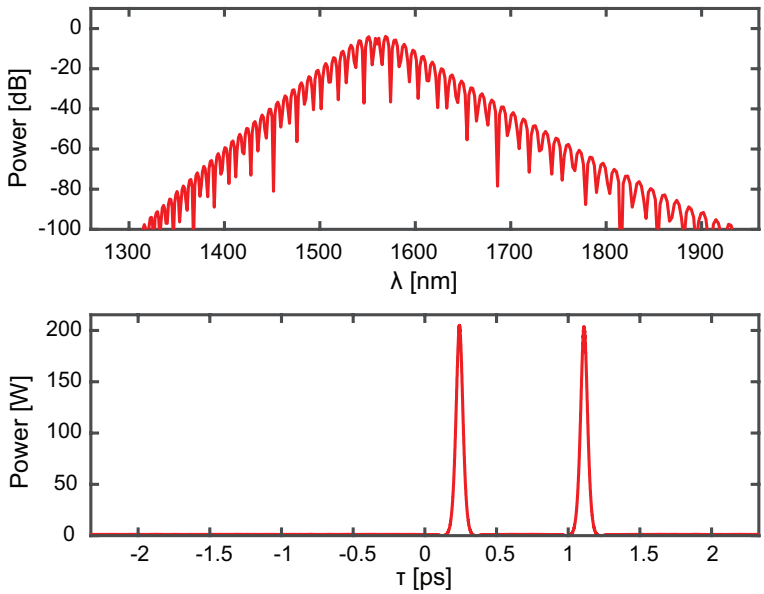

Figure 4.3: A stable two soliton state for a microresonator with radius 120 μm and waveguide cross section 950 $\times$ 1500 nm.

We use the dispersion calculated using the COMSOL FEM solver for the 950 $\times$ 1500 nm cross section and assume a ring with a radius of 120 μm to sim-

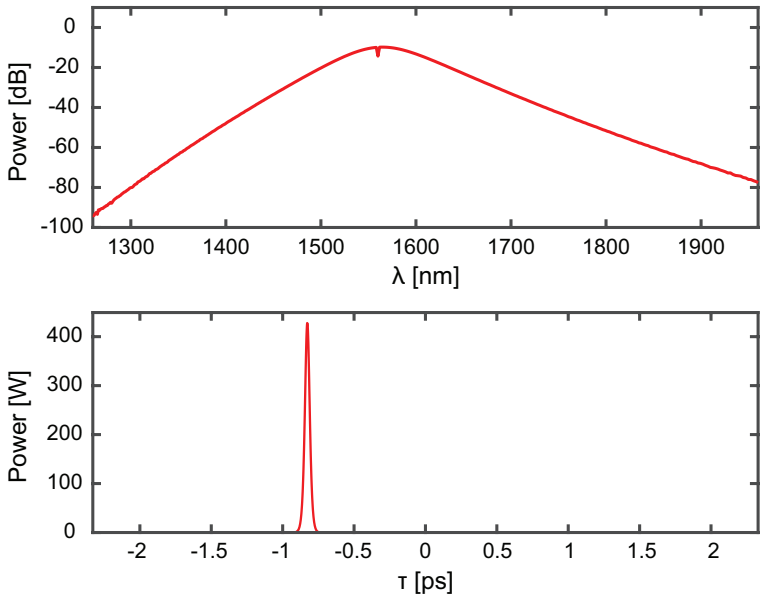

Figure 4.4: A stable single soliton state for a microresonator with radius 120 μm and waveguide cross section 950 $\times$ 1500 nm.

ulate the solution to the intracavity field using an adaptive split step fourier method [101]. By adjusting the detuning and adjusting the point at which we stop on the red detuned side, the LLE predicts different modelocked solutions with three, two and one soliton circulating in the microresonator cavity as can be seen in Fig. 4.2 - 4.4.

The modified LLE indicates that there exists a route to deterministically achieve soliton modelocked states in microresonators by adjusting the effective detuning from the blue detuned side and terminating the sweep on the red detuned side. However practically there are limitations to how this can be achieved precisely. One of the limitations arises from the fact that the effective detuning with respect to the resonance has a bistability. This bistability is introduced by the SPM that we studied in Chapter 2. In Section 3.2, we looked at the case of resonances for a ring with radius 100 μm in silicon nitride with a cross section of 730 $\times$ 1500 nm to look at the transmitted power through the cavity. In

this analysis, the effects of the SPM were not considered. The analysis considered a resonance condition given in terms of the circulating power by Eq. 3.12. Here the phase term for a given wavelength is $\phi(\lambda) = \beta(\lambda) * L$ however when we include the nonlinear phase introduced by the nonlinearity through SPM, the phase term becomes $\phi(\lambda) = \beta(\lambda) * L + \phi_{\mathrm{NL}}(\lambda)$. The power in the ring is given by B_0 and the input power is given by A_0. The power circulating in the cavity normalized to the input pump power including the nonlinear phase shift is given by,

$$P_{\text{circ}}(\lambda) = \left|\frac{\mathrm{B}_0}{\mathrm{A}_0}\right|^2 = \frac{a^2\,\kappa^2}{1 + a^2t^2 - 2at\,\cos(\beta\,L + \gamma\,|\mathrm{B}_0|^2\,L)} \tag{4.3}$$

As we can see in Eq. 4.1, the SPM term means that the power coupled into the ring acts on itself to shift the resonance wavelength due to the nonlinear phase. This creates a bistable solution for the power coupled into the cavity. We look at the resonance close to 1561 nm for the 730 $\times$ 1500 nm cross section ring with a radius of 100 μm that we saw in Fig. 3.5, but consider a lower linear loss in the waveguide of 4 dB/m [71] that is consistent with the values we expect for typical waveguides in this dissertation. We look at the unperturbed Lorentzian resonance shape according to Eq. 3.12 in black, and solve for the power coupled into the cavity using the Eq. 4.1. This leads to the distortion of the resonance. We look at two cases of input power in the bus waveguide $|\mathrm{A}_0|^2$ = 250 mW and 500 mW in red and blue respectively.

As we can see from the red and blue curves in Fig. 4.5, the effective detuning of the pump to the resonance remains on the blue detuned side even if the pump wavelength lies at a higher wavelength than what is termed as the cold

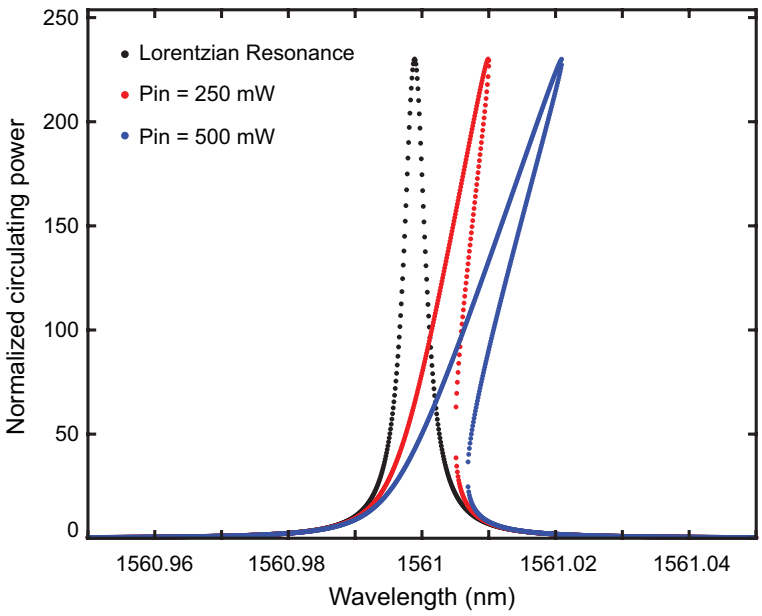

Figure 4.5: Shift induced in the resonance due to the SPM at high intracavity powers. We consider the case of the unperturbed Lorentzian resonance in black, and input powers of 250 mW and 500 mW in red and blue respectively.

cavity resonance wavelength of 1561 nm. Tuning into resonance from the blue detuned side, one needs to tune further than this wavelength to be able to access the red detuned side where the solution of the LLE predicts the existence of the soliton states. Additionally, the soliton generation process is initiated by the modulation instability that occurs on the blue detuned side so the laser frequency has to be tuned in a specific direction from blue to red detuned in order to access the soliton states.

In addition to the shift in resonance introduced by the Kerr nonlinearity we also see a shift introduced by the thermal nonlinearity. The coupled pump power leads to heating of the microresonator. This introduces a thermal shift in the resonance frequency due to the thermo-optic effect $\left(\frac{\partial n}{\partial T}\right)$. In the case of silicon nitride, the thermo-optic effect results in an increase in index corresponding to the temperature $\left(\frac{\partial n}{\partial T} \geq 0\right)$, which means that the thermal shift acts in the same

direction as the SPM induced shift that tilts the resonance further.

Following this preliminary work on modeling frequency comb generation and its dependence on pump-cavity detuning using the modified LLE, cavity solitons have been demonstrated in many of the material platforms on which frequency combs have previously been demonstrated, including Magnesium Fluoride [102], Silica [103–108], Silicon [82], Hydex [109], Lithium Niobate [110, 111], Aluminum Nitride [112], and Silicon Nitride [113–119].

The properties of Silicon Nitride that we previously discussed in Section 3.3, make it a suitable material for the demonstration of soliton modelocked combs using pumps in the near infrared region and more specifically in the wavelengths that form part of the telecommunications bands. The maturity of optical telecommunications technology allows us access to good laser sources with narrow linewidth, high sensitivity and high bandwidth photodetectors as well as other components such as filters, optical fibers etc.

The ability to generate coherent soliton frequency combs at the chip scale using microresonators opens up several applications such as dual-comb spectroscopy, distance ranging, low phase noise microwave sources, and coherent communications. It also enables the study of phenomena such as breather solitons [120–122], dispersive wave (Cherenkov radiation) emission [113], stokes solitons [85], bidirectional solitons in a single microresonator [123–125], and soliton crystals [126].

Coherent spectra can also be generated in normal GVD microresonators, where effects such as higher order mode interaction induced avoided crossings [127], or tunable avoided crossings using coupled rings [128], locally distort

the GVD and allow for phase matching of the modulation instability to initiate broadband comb generation.

4.2 Pump laser control of soliton modelocking

An obvious approach to controlling the effective detuning between the pump laser and the microresonator cavity is to tune the pump laser wavelength. Typically the linewidth of the cavity is $\mathcal{O}(100\text{ MHz})$ for nominal quality factors of the microresonators of 2×10^6 [71]. For most tunable lasers there are two tuning mechanisms, a coarse tuning based on mechanical actuation of the cavity length that tunes the laser wavelength over a large wavelength span and finer tuning based on piezoelectric actuation of one of the cavity end mirrors that tunes the lasing wavelength finely. The piezoelectric wavelength tuning speed is limited to how fast the piezoelectric material can be electrically modulated. The typical amplitude of the piezoelectric scan corresponds to 30 GHz at slow modulations of around 100 Hz that drops to 6 GHz at the maximum modulation speed of 2 kHz [129]. The piezo tuning amplitude is adequate to be able to tune starting from off resonance on the blue detuned side of the resonance and tuning into resonance and across the zero effective detuning to the red detuned side and eventually off resonance. Based on the modified LLE simulations, we expect to be able to generate a stable single soliton state using a waveguide with a cross section 950 $\times$ 1500 nm as seen in Fig. 4.4. A typical ring resonator used for the generation of soliton modelocked frequency combs is shown in Fig. 4.8. The pictured ring has a cross section of 730 $\times$ 1500 nm, with a free spectral range of 220 GHz.

We use a tunable laser at close to 1540 nm and amplify it using an erbium doped fiber amplifier (EDFA) that acts as the pump laser. The amplified pump laser is coupled to the bus waveguide by means of a lensed fiber (OZ Optics). The polarization of the pump laser is controlled by a paddle polarization controller to ensure that the input light is TE polarized to ensure that we operate in the TE_0 mode [Fig. 3.2], that has anomalous GVD at the pump wavelength of 1540 nm [Fig. 3.3]. We use a waveguide with a cross section of 950×1500 nm. The bus waveguide has an inverse taper at the input and output facets that expands the waveguide mode adiabatically and maximizes the overlap of the expanded mode with the output of the lensed fiber leading to significantly improved input coupling. We use a microresonator with a free spectral range of ≈ 200 GHz. We couple in 56 mW of pump power into the bus waveguide. At the output, the generated spectrum is coupled out using an aspheric lens that has an anti-reflection coating for telecommunication wavelengths. The output is split into three parts using fiber or free space optics. One part is sent to an optical spectrum analyzer (OSA) to record the generated frequency comb spectrum the other two parts are sent to a fast photodiode to monitor the pump transmission and also to measure the RF noise using a RF Spectrum Analyzer as the pump-cavity detuning is varied. The pump laser is swept across the cavity resonance from the blue detuned side to the red detuned side by applying a slow triangular ramp signal (100 Hz) from a waveform generator to the piezo tuning input of the laser.

The transmitted pump power normalized to the maximum pump transmission when the pump is completely off resonance is recored as the laser is swept across the resonance and is shown in Fig. 4.6. We observe several features in the normalized pump transmission as this sweep is performed. These features as

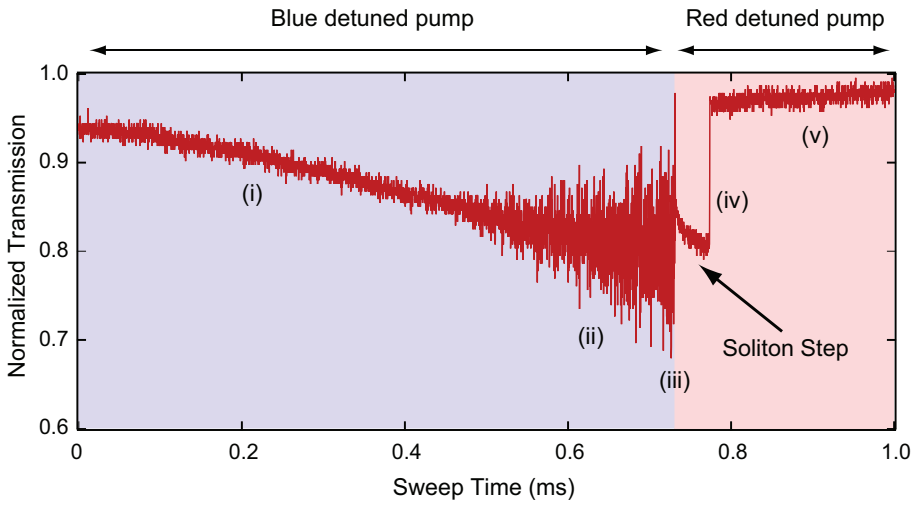

Figure 4.6: The normalized pump power as the pump laser is swept across the resonance by applying a triangular ramp sweep to the piezo control on the laser. We see several features (i-v) that are explained in the text. We also see a step-like feature indicated by the arrow that is characteristic of the transition to a particular soliton state.

indicated on the plot are as follows,

i. First we see the normalized transmitted pump power begins to dip below 1 as the laser light starts coupling into the ring.

ii. As the effective detuning is reduced further, we see noise appear on the pump transmission.

iii. Tuning further, the effective detuning reaches the zero detuning point at which point the intracavity power begins to drop and we see a jump in the transmitted power.

iv. This is followed by a step like feature in the pump transmission where the pump is on the effective red detuned side.

v. Finally, the pump transmission returns to 1 when the pump is completely off resonance on the red detuned side of the cavity.

As we see here in Fig. 4.6, pump laser tuning allows access to soliton states [102]. However, the speed of laser tuning limits the repeatable generation of soliton states in a given microresonator cavity. The frequency sweep of the laser shown in Fig. 4.6 results in a characteristic step like feature indicating a transition to soliton states. However the appearance of this step is not repeatable at the limited tuning speeds of the pump laser. The stochastic nature of the soliton step appearing as the effective detuning is swept is a result of the thermal and Kerr nonlinearities that introduce an additional phase shift as the intracavity pump power changes. The transition from the blue detuned to the red detuned side of the resonance frequency causes a drop in the intracavity power. This results in a corresponding recoil of the resonance as the nonlinear phase shift reduces. While the Kerr nonlinearity is instantaneous, the thermal nonlinearity has a related time constant due to the dissipative nature of distribution of heat in the material. This means that the thermal recoil will occur over a certain finite time. The laser-cavity detuning will have to be adjusted to counter this recoil in order to stably and repeatably access the soliton states. Typical thermal time constants for microresonator devices are a lot faster ($\mathcal{O}(100\text{ ns})$) than tunable lasers can be tuned ($\mathcal{O}(1\text{ ms})$) which limits the use of laser tuning to counter the thermal recoil. While limited in terms of repeatability, we can tune the laser in from the blue detuned side and terminate the scan within the step to access the soliton state with a non-zero probability. One such instance is shown in Fig. 4.7 where the generated single soliton agrees remarkably well with the predicted hyperbolic spectral pulse shape on top of a CW background from the pump. The dashed blue curve is a best fit to the hyperbolic secant pulse spectrum with a spectral 3 dB bandwidth of 24 nm.

Several approaches have been used to counter the effect of thermal recoil

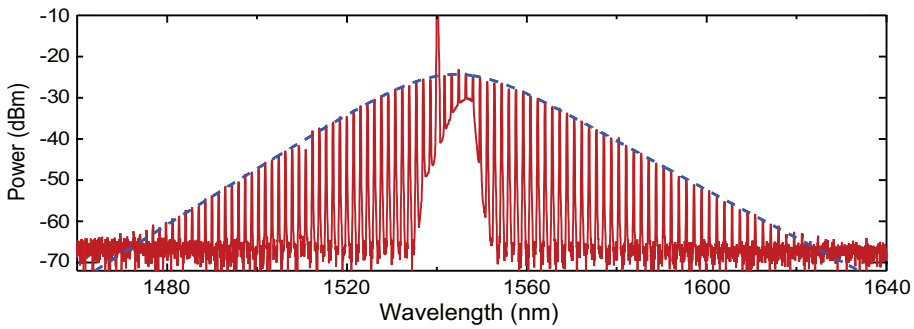

Figure 4.7: The generated single soliton state by tuning the pump laser from the blue detuned to the red detuned side and terminating the sweep in the soliton step. The recorded optical spectrum (in red) agrees well with a hyperbolic secant pulse spectrum (dashed blue) with a 3 dB bandwidth of 24 nm.

on the effective detuning in order to stably access the detuning range required for the soliton states including an abrupt increase in the pump power using acousto-optic modulators (AOMs) [105, 119], single sideband phase modulators to create a rapidly tunable pump [106], auxiliary lasers that couple into a different longitudinal mode of the microresonator to counter the drop in intracavity pump power [107, 109], and control of the free carriers in silicon to induce a change in the refractive index [82]. We use integrated heaters to achieve this fast control of the effective pump-cavity detuning to stably and repeatably access the soliton states.

4.3 Thermally controlled soliton modelocking

Silicon nitride and silicon dioxide, the core and cladding materials of the waveguides used to fabricate the microresonators used to generate frequency combs have a refractive index that varies with temperature. By adjusting the temperature of the microresonator the efective index of the waveguide can be tuned. The slope of the thermo-optic coefficient determines whether the induced phase due

to a change in temperature is positive or negative. For materials with a positive thermo-optic coefficient, the phase shift due to this thermal nonlinearity is the same sign as the nonlinear phase due to the Kerr nonlinearity. At room temperature, the thermo-optic coefficients of the the two materials are as below [130],

$$\frac{\partial \mathrm{n_{SiN}}}{\partial T} = 2.45 \pm 0.09 \times 10^{-5}\ \mathrm{RIU/^{\circ}K} \tag{4.4}$$

$$\frac{\partial \mathrm{n_{SiO}}}{\partial T} = 0.95 \pm 0.1 \times 10^{-5}\ \mathrm{RIU/^{\circ}K} \tag{4.5}$$

Silicon nitride and oxide have thermo-optic coefficients with a positive sign implying that the index increases with increasing temperature. From the resonance condition given by Eq. 3.10 and the thermo-optic coefficients of the nitride and oxide Eqs. 4.4 & 4.5, an increase in temperature results in an increase in the effective index n_{eff} which results in an increase in the resonance wavelength λ_{m} and a decrease in the resonance frequency ω_{m}. This means that if the pump laser ω_{p} starts blue detuned with respect to the resonance frequency $\delta = (\omega_{\mathrm{p}} - \omega_{\mathrm{m}}) > 0$, the resonator needs to be cooled down in order for the pump to be tuned from the blue detuned side $(\delta > 0)$ to the red detuned $(\delta < 0)$ side of the resonances. One potential approach to tuning a microresonator thermally is to place a thermoelectric cooler (TEC) element under the microresonator chip. The TEC element relies on the Peltier effect [131] to create a temperature gradient across a junction between two conductors when a current is passed through the junction. The chip can be placed at either end of the TEC to raise or lower the temperature with respect to the ambient temperature. At one end of the junction, the chip effectively acts as a heat sink and raises its temperature relative to the ambient temperature, or it can be placed on the opposite end of the junction where it gets cooled with a heat sink drawing heat away at the other

end. However the heating or cooling of the chip using this approach relies on a diffusive heat transfer process and can be very slow. It can potentially be slower than the laser tuning speeds depending on how thick the oxide and silicon substrate layers are with time constants for the tuning of the order $\mathcal{O}(1s)$. This slow tuning speed at best can allow us to switch between two detuning levels but it cannot be relied upon to generate a soliton state. As we saw earlier in Section 4.2 apart from the direction of tuning, the speed of tuning also affects the probability of generating a soliton state, so a detuning control approach that can allow significantly faster tuning speeds is required.

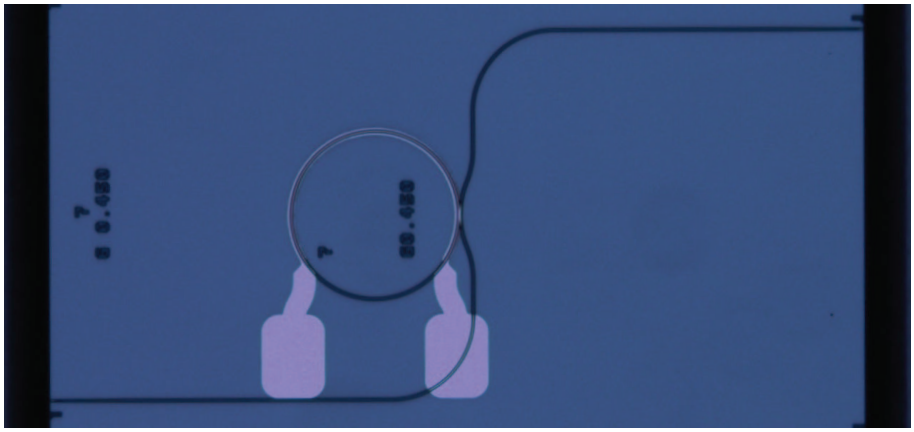

Figure 4.8: A typical ring resonator with integrated heaters used to generate soliton modelocked frequency combs. The ring in the picture has a cross section of 730 $\times$ 1500 nm, with a free spectral range of 220 GHz at 1560 nm. The gap between the bus waveguide and the ring is 450 nm.

The fabrication process for the microresonator devices [71,72] allows for the deposition of a metal layer on top of the Oxide cladding layer. The thickness of the cladding layer is 3 μm including a 500 nm layer of HTO and 2.5 μm of PECVD oxide. A thin 100 nm layer of platinum is sputtered on top of the oxide layers and heater patterns are defined using photolithography. The heaters lie above the ring and form a near complete arc following the ring and are 6 μm wide as can be seen in Fig. 4.8. The two ends of the heater arc are tapered out

into contact pads with a rounded rectangular shape 25 μm on each side. The larger contact pad area allows us to easily land tungsten probe tips and make contact with the heater layer. The contact pads are spaced at a 100 μm pitch that matches the pitch of the tungsten probe tips. The process of heating relied upon is Joule heating where a current passed through the resistive heater generates heat. This heating of the platinum layer leads to the creation of a temperature gradient through the oxide and nitride layers resulting in a change in the n_{eff} of the waveguide. This heat transfer process is also diffusive but since the distance of the heater layer from the waveguide layer is much smaller than in the case of the TEC the thermal time constant is much smaller.

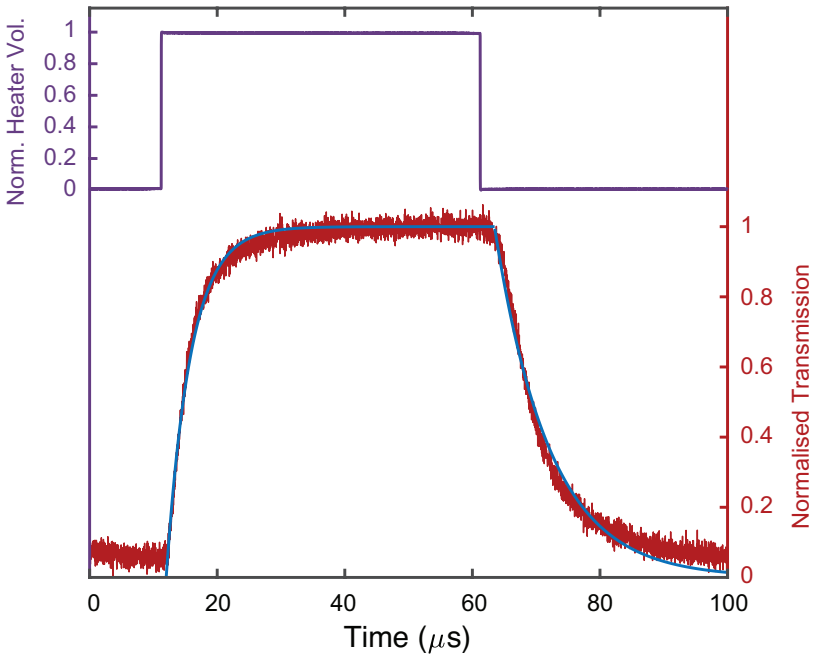

Figure 4.9: We modulate the heater voltage with a square wave while on resonance (purple curve). The corresponding response in the pump transmission (red curve) shows an exponential rise and decay which yields the thermal time constants by fitting to an exponential rise and fall (blue curves).

We test the thermal response times for our integrated heaters by operating at a low optical power where the thermal and Kerr nonlinearity are low. This

allows us to measure the thermal constants and rise and fall times without any distortion due to these non-linearities. We park the heaters at a linear point on the dip of the resonance and modulate the heater with a square wave. The pump transmission curve is recorded and normalised to 1. From a fit to exponential rise and fall functions $e^{-t/\tau}$ and $1 - e^{-t/\tau}$, the time constants for the rise and fall exponential curves are, $t_{\text{rise}} = 3.82\ \mu$s and $t_{\text{fall}} = 8.60\ \mu$s. The 90-10 time constants are $\tau_{\text{rise}} = 8.40\ \mu$s and $\tau_{\text{fall}} = 18.89\ \mu$s. The fall time results in a bandwidth for the heaters of 18.52 kHz. This is significantly faster than the bandwidths for the piezo control on the laser, that is at best limited to 2 kHz at very smaller amplitude and around 300 Hz at larger amplitudes.

Additionally, the ability to tune the resonance frequency by applying a current to the heaters allows us to use fixed frequency lasers instead of tunable lasers as the pump. Tunable lasers derive their tunability from mechanical movement of the cavity to adjust the cavity length that changes the laser frequency. The mechanical movement of the laser cavity is derived by mechanical actuators on on one of the end mirrors for coarse tuning over a wide range or piezoelectric tuning of one of the end mirrors to achieve fine tuning. This adds phase noise to the laser output and leads to a broadening of the laser linewidth. Typical linewidths over 5 ms of averaging for tunable lasers are 200 kHz [129]. The frequency comb generation process in microresonators as we have seen is governed by parametric four-wave mixing (FWM), and this leads to a transfer of phase noise and amplitude noise on the pump to the comb lines which determines the linewidth of the comb lines [132, 133]. Using a quieter narrow linewidth pump laser would lead to the generation of narrow linewidth comb lines. Fixed frequency lasers, by design use a passive cavity, that allows for much narrower laser linewidths. The laser we use is an external cavity laser

(Redfern Integrated Optics Orion module) with an architecture consisting of a Indium Phosphide gain chip with one highly reflective end acting as one cavity mirror. This is butt coupled at the low reflection end to a planar waveguide with a Bragg grating that acts the output mirror. The entire structure is placed on top of a thermoelectric cooler that provides a small degree of tunability (20 pm) around the center wavelength that the laser is designed for. The laser is designed to align perfectly with one of the channels of the DWDM ITU grid. The pump laser we use is a Channel 22 laser corresponding to a frequency of 192.2 THz (1559.79 nm). A schematic of the laser architecture and the spectrum as measured in the laser datasheet [134] are shown in Fig. 4.10.

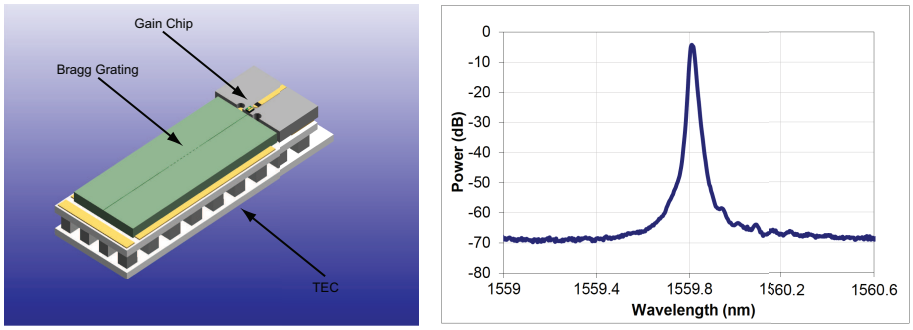

Figure 4.10: Schematic of the RIO laser architecture and measured output spectrum at the ITU Channel 22 (192.2 THz). Figure for the laser architecture adapted from [134]

We amplify the pump laser using an EDFA and couple the light into the bus waveguide using a lensed fiber. The polarization of the input light is controlled using a 3 paddle polarization controller to ensure that we are coupling into the TE_0 mode. The light at the output is split into two parts to monitor the optical and RF characteristics of the generated frequency comb. A schematic of the setup used to generated thermally controlled solitons in silicon nitride microresonators is shown in Fig. 4.11.

The impedance of the heaters is measured to be $\approx 240\ \Omega$. We use the same

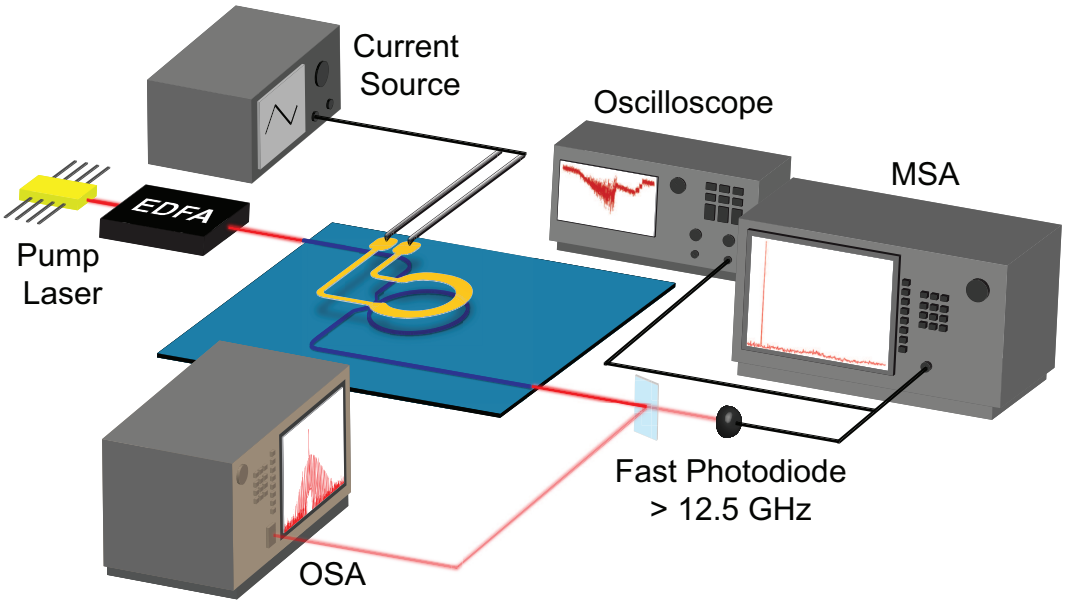

Figure 4.11: Schematic of the experimental setup used to thermally control the generation of frequency combs in a silicon nitride microresonator. The pump laser is amplified using an EDFA. The output is characterized optically and electrically using an Optical Spectrum Analyzer (OSA), Microwave Spectrum Analyzer (MSA) to characterize the RF noise, and an Oscilloscope to monitor the pump transmission. The electrical signals are generated by detecting the optical output on a fast photodetector with a bandwidth $\geq$ 12.5 GHz.

microresonator with a free spectral range of 200 GHz. We amplify the pump laser using an EDFA and couple 71 mW into the bus waveguide. We then apply a DC offset current of 25 mA to send 150 mW of electrical power to the heaters through tungsten probe tips from an arbitrary waveform generator. This brings the resonance frequency of the microresonator close to the laser frequency such that the laser is blue detuned with respect to the cavity resonance as required to initiate the comb generation process. We then apply a triangular ramp signal at a frequency of 10 kHz corresponding to a power modulation amplitude of 5 mW. As the resonance frequency is swept across the pump laser, we see the pump transmission go through the same evolution as the pump tuning case seen earlier in Fig. 4.6 until it reaches the zero detuning point. On the red detuned side, due to the tuning speed being a lot closer to the speed of the thermal

recoil, we see richer dynamics in the evolution of the soliton states. We see multiple steps corresponding to different numbers of soliton propagating around the cavity. By carefully adjusting the termination point of the scan different soliton states can be accessed. These single and multi soliton states are similar to the ones predicted by the modifed LLE as we saw in Fig. 4.2-4.4. A sweep of the cavity resonance frequency across the pump frequency using a triangular ramp at 10 kHz is shown in Fig. 4.12.

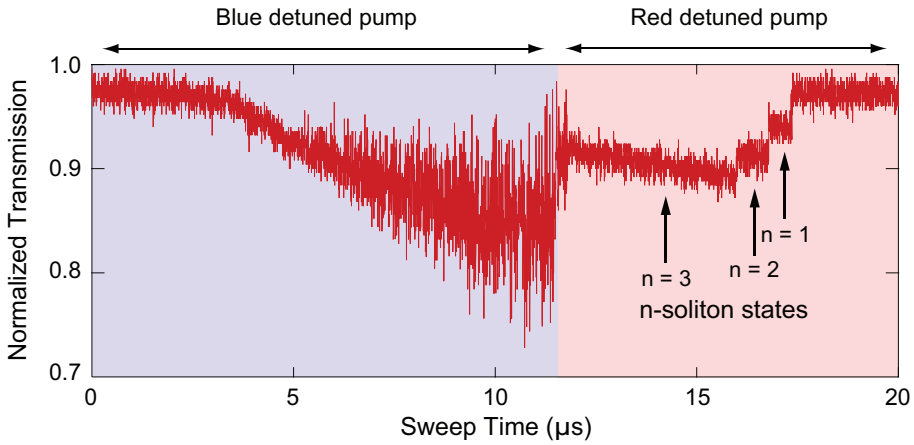

Figure 4.12: The normalized pump power as the microresonator resonance frequency is swept across the pump laser by applying a triangular ramp sweep at 10 kHz with an amplitude of 5 mW in electrical power to the integrated heaters using a waveform generator. On the red detuned side we observe multiple steps that correspond to single and multi soliton states.

We record the evolution of the generated comb spectrum and the RF noise using an OSA and MSA. The comb evolves through various states as the detuning scan is terminated at various points on the blue and red detuned side. This behavior closely agrees with the predictions from the modified LLE in Fig. 4.1. The evolution of the optical and RF spectra is as follows

- First we see the generation of primary sidebands at the peak of the MI gain spectrum [Fig. 4.13 (i)]. Here the optical spectrum has the primary

sidebands and secondary peaks generated from cascaded FWM. The RF spectrum is at the noise floor of the detection.

- Tuning further into resonance, we see the sidebands grow in power and act as secondary pumps for additional FWM frequency conversion. This leads to interacting mini-combs with the possibility of different comb lines being generated within a single cavity resonance. This interaction between families of mini-combs manifests as spikes on the RF spectrum [Fig. 4.13 (ii)].
- As we tune in further close to the zero effective detuning point, the comb transitions to a high noise chaotic state. With the increase in pump power, we see chaotic interactions that eventually lead to the broad RF noise that approximately spans the cavity resonance linewidth. On the optical spectrum this appears as a broad spectrum with comb lines generated at each cavity resonance with a plateau like spectrum [Fig. 4.13 (iii)].
- When the scan is terminated on the red detuned side within the single soliton step, the RF noise from the high RF noise drops back to the noise floor. On the optical spectrum we see a transition from the plateau like comb spectrum to a hyperbolic secant pulse shape [Fig. 4.13 (iv)]. Based on the hyperbolic secant fit, the 3 dB bandwidth of the soliton is 20 nm corresponding to 120 fs pulses.

This transition in the RF noise from the high noise state to the noise floor was first observed in Silicon Nitride microresonators and was confirmed to be indicative of pulsed operation [60]. This drop in noise results from the organization of the strongly interacting pulses within the cavity to a series of stable solitons as predicted by the modified LLE. In the frequency domain this results

in perfect equidistance of the comb lines in frequency and the multiple comb lines within a single cavity resonance drop transition to a single comb line. The spacing between the comb lines is the inverse of the repetition rate f_{rep} of the pulses circulating within the cavity.

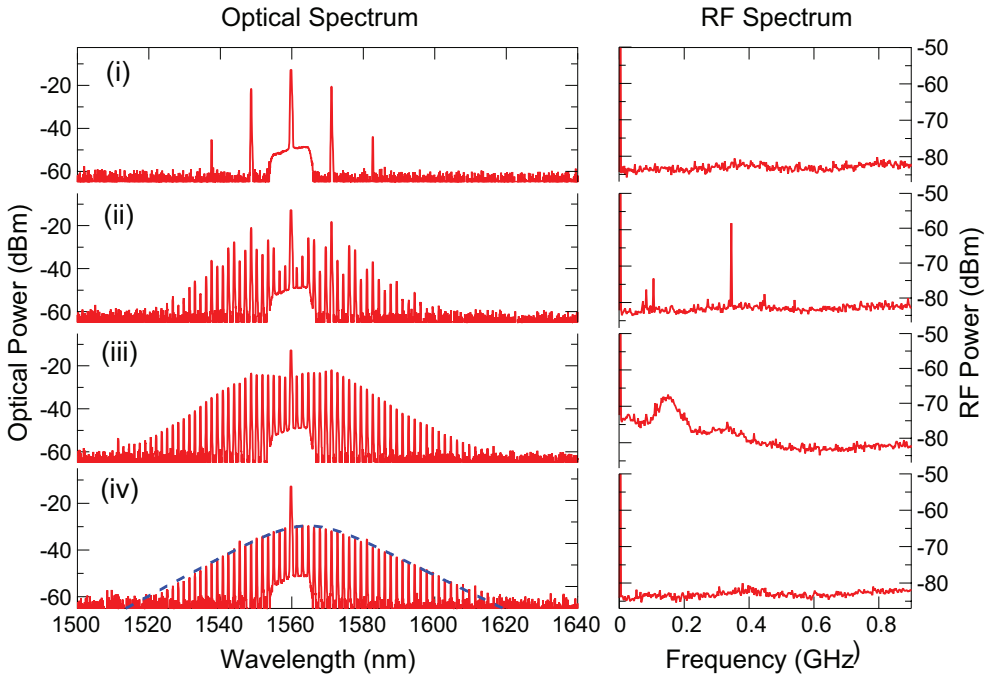

Figure 4.13: The optical and RF spectra as the comb evolves are recorded using an OSA and MSA. The recorded spectra as the detuning is varied and the scan is terminated at different detunings correspond to (i) the initial sidebando formation at the MI gain peak, (ii) the mini-comb formation, (iii) the broadband high-noise regime, with the plateau-like optical spectrum and broad noise peak and (iv) the low-noise single-soliton state with a fitted sech^2-spectral profile (blue dashed curve).

The pump laser frequency starts blue detuned with respect to the cavity resonance, so the cavity needs to be cooled in order for the effective tuning to go from the blue to the red. So we first apply a downward ramp on the heater current. This downward ramp continues to the point of zero effective detuning. At this point the power drop in the cavity results in a thermal recoil that causes the effective detuning to jump abruptly into the red detuned. We introduce a small

but sharp increase in the heater current at this point. At the end of this sharp increase, we terminate the scan and stop at a DC level. The amplitude of the sharp increase partially compensates for the thermal recoil and determines the effective detuning on the red detuned side at which we settle. Looking at this in terms of equilibrium temperature, the drop in ring temperature due to the drop in intracavity power is partially compensated by the rise in temperature introduced by this sharp increase in heater current. The tuning curve is shown in Fig. 4.14.

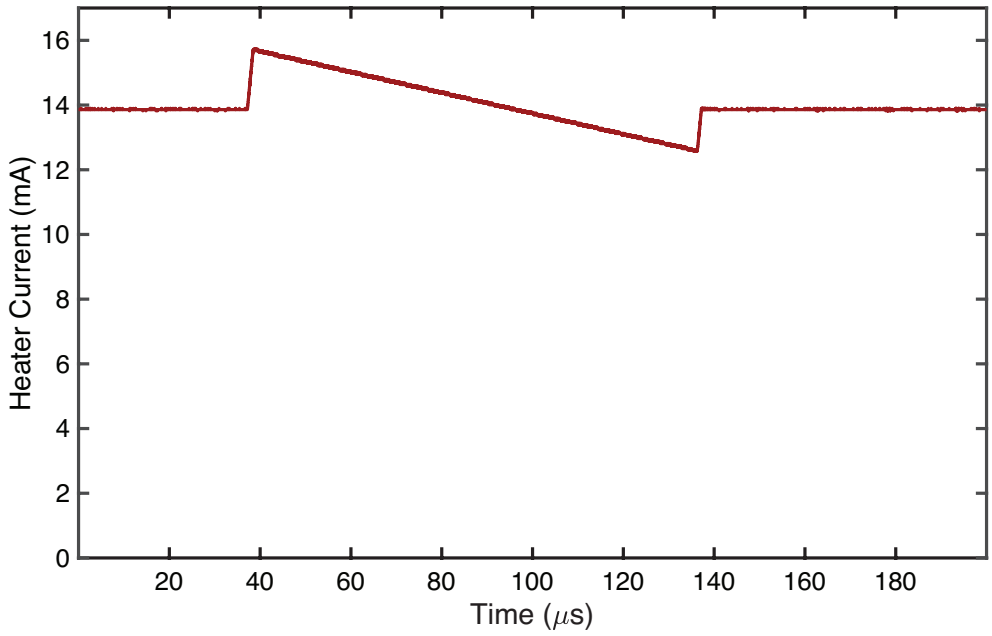

Figure 4.14: The current tuning curve used to reach a soliton modelocked state in a silicon nitride microresonator. The DC offset lines up the resonance close to the laser wavelength. The top of the ramp is such that the laser starts blue detuned with respect to the pump. The amplitude of the sharp increase in current prior to termination of the tuning curve back at the DC level determines the effective red detuning of the laser at the end of the tuning curve.

By adjusting the amplitude of the sharp increase we can precisely terminate the scan in the single soliton state. The generated single soliton spectrum is recorded and fit to a hyperbolic secant spectrum. The 3 dB bandwidth of the generated soliton is 20 nm based on the hyperbolic secant fit. This corresponds

to pulses with a pulse width of 120 fs. The recorded optical spectrum and fit to the hyperbolic secant spectral shape can be seen in Fig. 4.15.

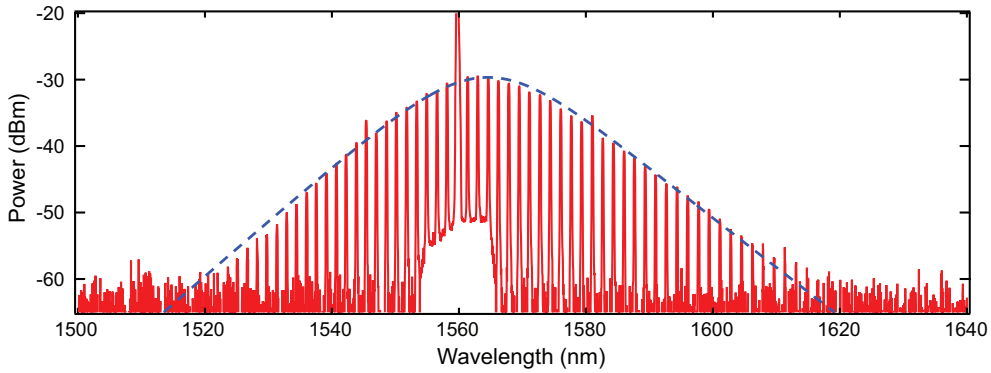

Figure 4.15: A single soliton is generated by choosing the appropriate amplitude of the sharp increase in the heater current prior to terminating the heater current scan at a given DC level. The recorded optical spectrum is fit to a hyperbolic secant spectral shape (dashed blue). The fit to the hyperbolic secant yields a 3 dB bandwidth of 20 nm.

By changing the amplitude of the sharp increase in the heater current, other states that correspond to the steps with a higher number of solitons seen in Fig. 4.12 can also be accessed. These states correspond to two or three solitons circulating within a single round trip of the cavity. The relative phase between the solitons results in the appearance of modulations on top of the time averaged spectrum recorded by the OSA. The relative phase determines the shape of the modulations. These spectra are recorded in various multi-soliton states and are shown in Fig. 4.16. Of special interest is the state in Fig. 4.16 (a) that depicts a state with every other comb line perfectly extinguished resulting in a time averaged spectrum that appears to be at twice the expected comb spacing. This corresponds to a series of pulse at twice the repetition rate determined by one round trip of the cavity. This implies that there are two equally spaced pulses within each cavity round trip perfectly separated from each other by a π phase.

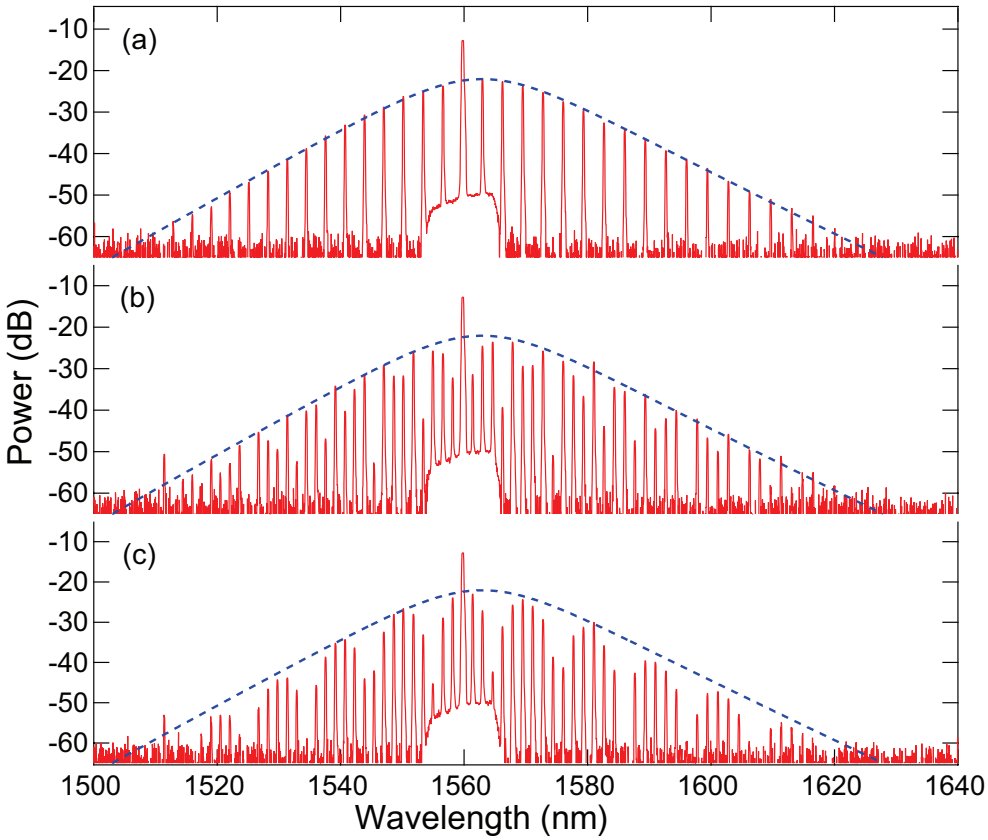

Figure 4.16: Generated multi-soliton states corresponding to different detunings as the scan is terminated. The spectrum in (a) is of particular interest because it shows a two soliton state with the pulses exactly π out of phase within the cavity.

With a slightly lower pump power, the thermal shift due to the drop in intracavity power is lower. We lower the pump power to 28 mW in the bus waveguide and record the transmission as the heater current is scanned. We observe a low noise, 4 soliton step that is at a similar power to the high noise state as shown in Fig. 4.17 (a). In this case the intracavity power due to the four solitons within one round trip is approximately equal to the high noise state and this state is thermally stable with negligible thermal recoil when the effective detuning crosses the zero detuning point. This allows us to tune into this state slowly as it is thermally stable with respect to the detuning. We can tune into this state extremely slow near DC tuning. The resulting multi-soliton state is Fig. 4.17 (b)

and shows a 4 FSR state. As before this corresponds to a state with 4 solitons equally spaced within one round trip of the microresonator cavity spaced by a $\pi/2$ phase shift from each other.

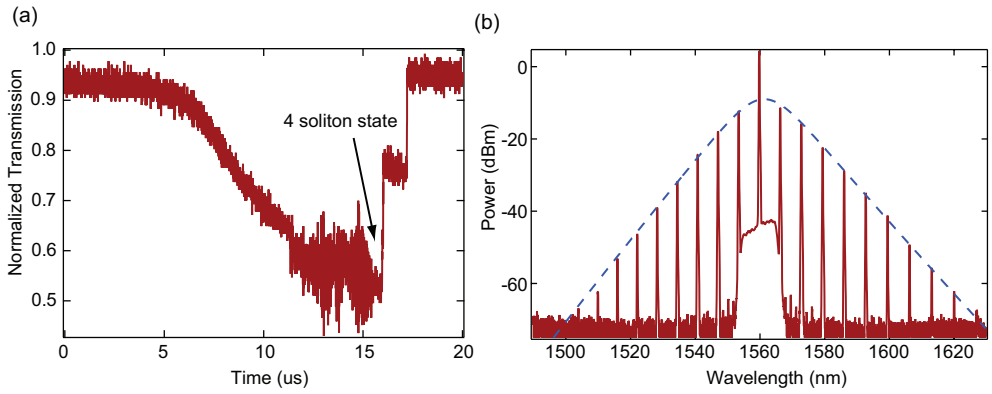

Figure 4.17: (a) Pump transmission for a thermally stable 4 soliton state that we can tune into at slow speeds. (a) The 4 FSR state shows a spectrum with every 4th line present. This corresponds to a state with four pulses exactly $\pi/2$ out of phase within the cavity.

The same ring resonator in slightly different conditions supports a single soliton within one cavity round trip, two equally spaced solitons with a π phase shift, and four equally spaced solitons with a π phase shift. The waveguide cross section used to generate these spectra is multi mode. These states appear to be preferentially excited in this particular microresonator and this can be attributed to the presence of mode crossings. The mode crossing results in a local enhancement of the comb line near the crossing. Mode crossings occur due to conversion of light from the fundamental mode to a higher order mode.

If we assume a perfectly rectangular waveguide, the modes are orthogonal to each other. Any perturbation from the perfectly rectangular cross section can result in coupling of light from the fundamental mode to a higher order mode. In the ring resonator, side wall and top surface roughness can act as scattering locations and allow coupling between modes. Additionally, the coupling region

can act as a local perturbation and cause coupling between the fundamental and higher order modes. The effective refractive indices for different modes differ. This leads to different resonance frequencies for the different mode families. If the resonance frequencies for the fundamental mode and a higher order mode overlap at a particular frequency, this causes an enhancement in the coupling between the two modes. Locally, at this frequency it leads to a change in the dispersion of the fundamental mode. This creates an imbalance in the phase matching that enhances a particular comb line. This results in the preferential excitation of the two and four soliton states under the right effective detuning and pump power conditions as seen in Fig. 4.18. Since the pulses are equally spaced within the cavity at a harmonic of the native repetition rate, it results in a harmonically modelocked state [135]. These can also be considered to be soliton crystals with equidistant solitons [126,136].

This technique of using integrated heaters to control the soliton generation allows for repeatable generation of solitons. Once the parameters of the tuning curve are accurately established, the system is able to consistently reach an identical soliton state each time the tuning modulation is sent through the heaters. We record 15 consecutive traces of the initialization of a particular soliton state over 3 seconds. As we can see from Fig. 4.19 the system reaches the same state each time.

The ability to repeatably and reliably generate solitons in a silicon nitride microresonator enables several applications such as dual comb spectroscopy [137], synchronization of two soliton trains on distinct, nearly identical microresonators by coupling them in a master-slave relationship [138], harmonic and subharmonic synchronization between soliton trains at a multiple of each

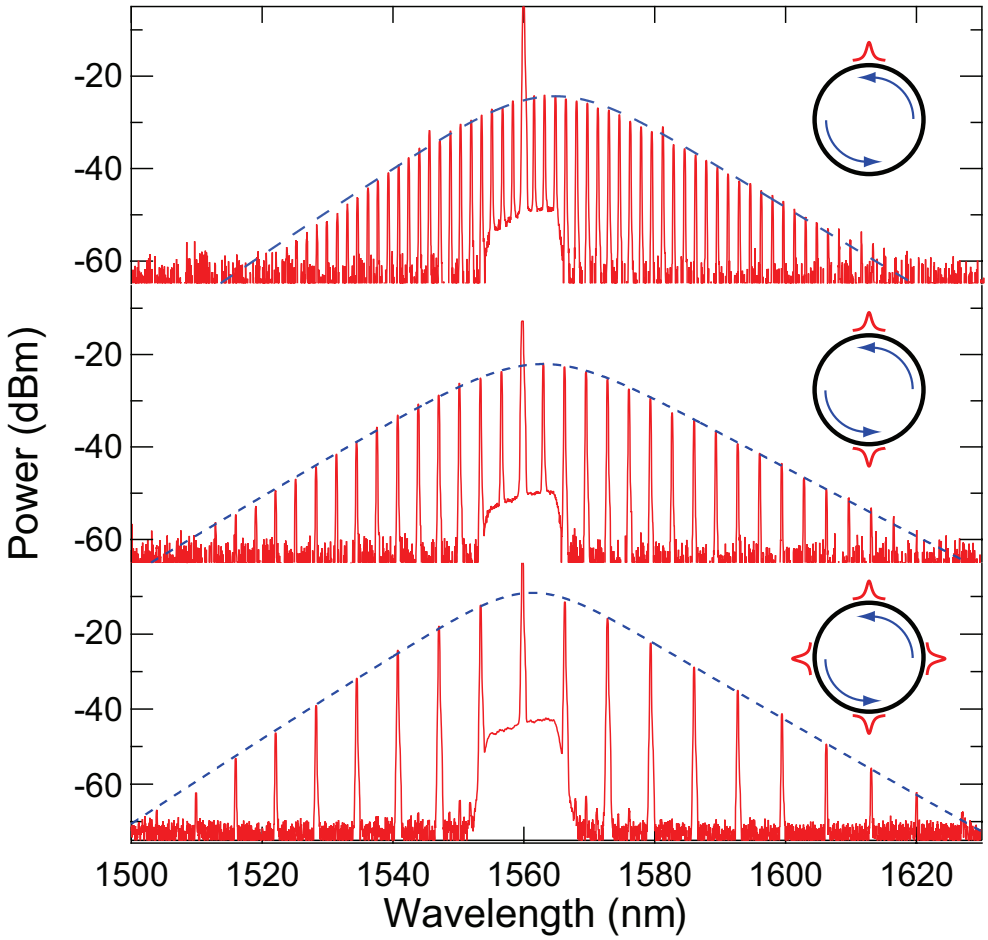

Figure 4.18: Generated one, two, and four soliton states corresponding to harmonically modelocked states. The two and four soliton states correspond to equally spaced solitons around one round trip and result in time averaged spectra at 2 and 4 FSR spacings.

other [139], a near-visible soliton modelocked frequency comb [140], and a battery operated integrated comb source that uses a high quality factor resonator to generate the comb as well as act as an end mirror for the laser cavity [141].

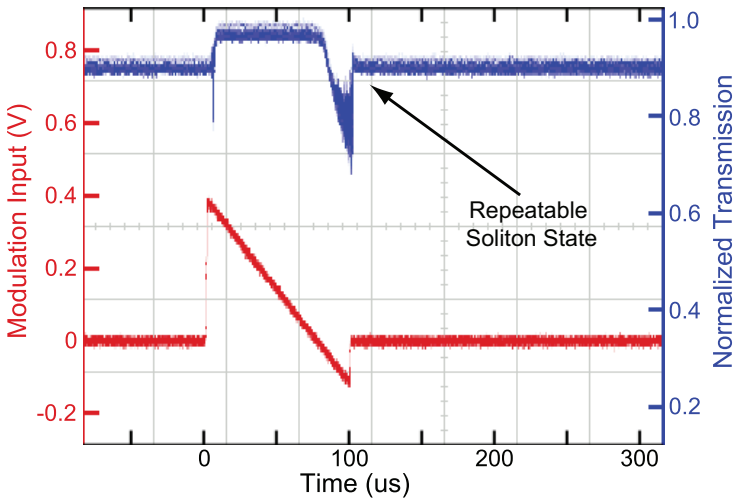

Figure 4.19: Repeatable generation of an identical soliton state can be achieved using the thermal tuning method detailed in this dissertation. Recorded persistence traces of 15 consecutive initializations of the same soliton state over a span of 3 seconds.

CHAPTER 5

COUNTER-ROTATING CAVITY SOLITONS

Optical frequency combs find applications in spectroscopy by virtue of their frequency precision and high coherence over a broad bandwidth. Direct frequency comb spectroscopy can be performed by sending a single frequency comb through a material sample of interest and observing the absorption features imprinted on the optical spectrum. This approach is well suited to studyng known transitions at a specific frequency such as the spectroscopy of particular lines of atomic and molecular species [17–20]. However, for broadband spectroscopy this approach has limitations. Over a broad bandwidth there might be multiple absorption features from the same species and resolving them requires a frequency selective element such as a monochromator or a FTIR spectrometer that scans over the frequency spectrum and detects the absorption features at their respective frequencies. Alternatively, the spectrum at the output can be separated in frequency using a grating or a virtually imaged phased array (VIPA) and detected on a photodetector array to resolve each comb line independently [25]. The speed of scanning of the monochromator or the FTIR delay arm limits the acquisition speed of the spectral measurements to time scales on the order of tens of milliseconds to a second or more depending on the optical bandwidth to be covered. On the other hand, in the case of the dispersive elements such as a VIPA to separate the spectral components, the density of lines and spatial separation will determine the size, and corresponding cost of the photodetector array required which limits the resolution of the spectroscopy measurement. An approach to spectroscopy using frequency combs that attempts to solve these limitations is dual comb spectroscopy (DCS) that uses two combs at slightly different repetition frequencies f_1 & f_2 that act as a reference

and probe combs.

5.1 Dual comb spectroscopy

DCS is a powerful spectroscopic technique that uses two combs with slightly different repetition frequencies f_1 & f_2. The f_1 comb acts as a reference local oscillator comb while the f_2 comb probes the species of interest. The two combs are then recombined and detected on a photodetector. The heterodyne beat signal between the two combs is recorded using a photodetector of the appropriate bandwidth and appears at the difference in frequencies between each pair of comb lines from the reference and probe combs. The difference in repetition rates $\Delta f = f_1 - f_2$ means that the heterodyne beating of each pair of comb lines will result in a RF tone at a multiple of Δf. The recorded heterodyne beat signal will have a sequence of beat notes separated by Δf in the frequency domain. In the time domain this results in a interferogram [92]. The technique was first proposed in 2002 by Schiller [142] who set up the mathematical framework and proposed a basic setup to perform these spectroscopic measurements. Subsequently demonstrations of dual comb sources were shown using a pair of Ti-Sapphire lasers [94], stabilised fiber modelocked lasers [27], free running fiber modelocked lasers [143], Cr^{2+}:ZnSe femtosecond oscillators in the mid infrared [144], tunable electro-optic combs [145], modelocked integrated external-cavity surface emitting lasers (MIXSEL) [146], quantum cascade lasers (QCL) [147].

The ability to generate soliton modelocked frequency combs on microresonator devices led to the development of integrated dual-comb sources on various material platforms such as silicon nitride [137], silicon [148], silica [149] and

magnesium fluoride [150]. We use two silicon nitride microresonators in series on a single bus waveguide to generate a pair of single soliton modelocked combs with slight different repetition rates with a difference in frequency of $\Delta f = 1.12$ GHz. The combined output of the two soliton trains is sent through a liquid sample of dichloromethane to record the spectrum. With 20 μs of acquisition of the time interferogram on a fast photodiode (BW $\geq$ 45 GHz), a spectrum spanning 170 nm can be recorded [137]. A schematic diagram that explains dual comb spectroscopy, and the measured spectrum of dichloromethane is shown in Fig. 5.1.

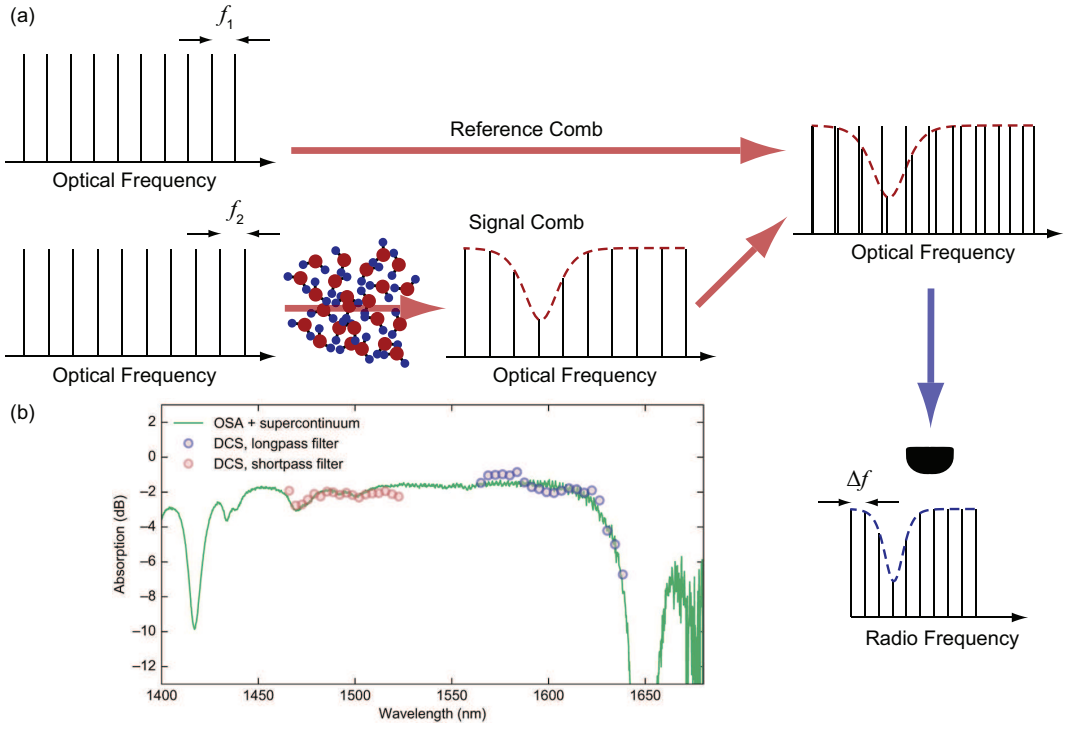

Figure 5.1: (a) A schematic of dual comb spectroscopy. Two combs with slightly different repetition frequencies act as the reference and signal combs. The absorption spectrum of the species of interest is imprinted on the signal comb and can be measured through heterodyne detection on a fast photodetector. (b) A spectrum of dichloromethane recorded using two soliton modelocked silicon nitride microresonators with a frequency difference of$\Delta f = 1.12$ GHz adapted from [137].

5.2 Bidirectionally pumped microresonators

An interesting regime of operation for microresonators is bidirectional pumping. Bidirectional pumping results in richer nonlinear dynamic interactions between the two pump fields that lead to novel dynamics when the detuning of the laser are is swept with respect to the resonator frequency. Operating in this pumping regime would enable the study of novel frequency comb generation dynamics that include soliton interactions within the cavity as well as XPM between the pump fields that introduces coupling between the modes propagating in opposite directions. Dual combs generated on two distinct microresonators are limited in mutual coherence by the uncorrelated noise between the two lasers [149], or uncorrelated heater current noise [137], or uncorrelated current noise on the p-i-n junction [148]. The ability to generate soliton modelocked combs in both directions in a single microresonator would eliminate sources of common mode noise due to relative fluctuations between the pump lasers or the electrical source of uncorrelated noise. Recently, there have been demonstrations of bidirectional mode-locked solid state [151] and fiber [152, 153] laser cavities, and has been used to demonstrate dual comb spectroscopy [154], a bidirectionally pumped microresonator-based system could be highly compact and fully integrated onto a chip.

As we saw earlier in Eq. 3.12, the pump power circulating in the cavity acts on itself through SPM and causes a bistability in the resonance. In the case of a bidirectionally pumped microresonator, the two directions are coupled to each other because in addition to the SPM we also have an interaction between the two pump field in opposite directions through XPM. Recent studies have looked at the effects of such an interaction mediated by the SPM and XPM in a

bidirectionally pumped system [155]. The symmetry breaking in such a system can be exploited to create a gyroscope with enhanced sensitivity to rotation [156, 157].

$$P_{\text{circ,CW}}(\lambda) = \frac{P_{\text{in,CW}}\, a^2\, \kappa^2}{1 + a^2 t^2 - 2at\, \cos(\beta\, L + \gamma\, (P_{\text{circ,CW}} + 2P_{\text{circ,CCW}})\, L)} \tag{5.1}$$

$$P_{\text{circ,CCW}}(\lambda) = \frac{r P_{\text{in,CW}}\, a^2\, \kappa^2}{1 + a^2 t^2 - 2at\, \cos(\beta\, L + \gamma\, (P_{\text{circ,CCW}} + 2P_{\text{circ,CW}})\, L)} \tag{5.2}$$

Apart from the bistability due to the SPM, the bidirectional pumping leads to an additional phase shift that is introduced on the fields in both direction by the XPM. This leads to an additional shift on the effective detuning as the laser-cavity detuning is tuned. As before we look at the power coupled into the clockwise and counterclockwise directions assuming a degenerate pump in both directions. We assume a input pump power, $P_{\text{in,CW}} = 60, 70, 80$ mW in the clockwise direction and a ratio $r = P_{\text{in,CCW}}/P_{\text{in,CW}} = 0.9$. The power circulating in the cavity in the clockwise and counterclockwise direction for these cases is solved for using Eq. 5.1 and Eq. 5.2 for these values and can be seen in Fig. 5.2. We observe the increasing region of bistability due to the higher SPM similar to Fig. 4.5. However with increasing power we also see the formation of a 'bubble'-like feature on the resonance shape on the blue detuned side of the resonances. This arises due to the leading factor of 2 on the XPM term causing a larger nonlinear shift on the opposite direction. The power imbalance in the pump in the two directions leads to a bubble that pushes the direction with the higher pump power closer to zero detuning faster the the direction with the lower pump power. We will see in Section 5.3 how the power imbalance creates a corresponding imbalance in the effective detuning that allows for independent control of the generated frequency combs in the two directions.

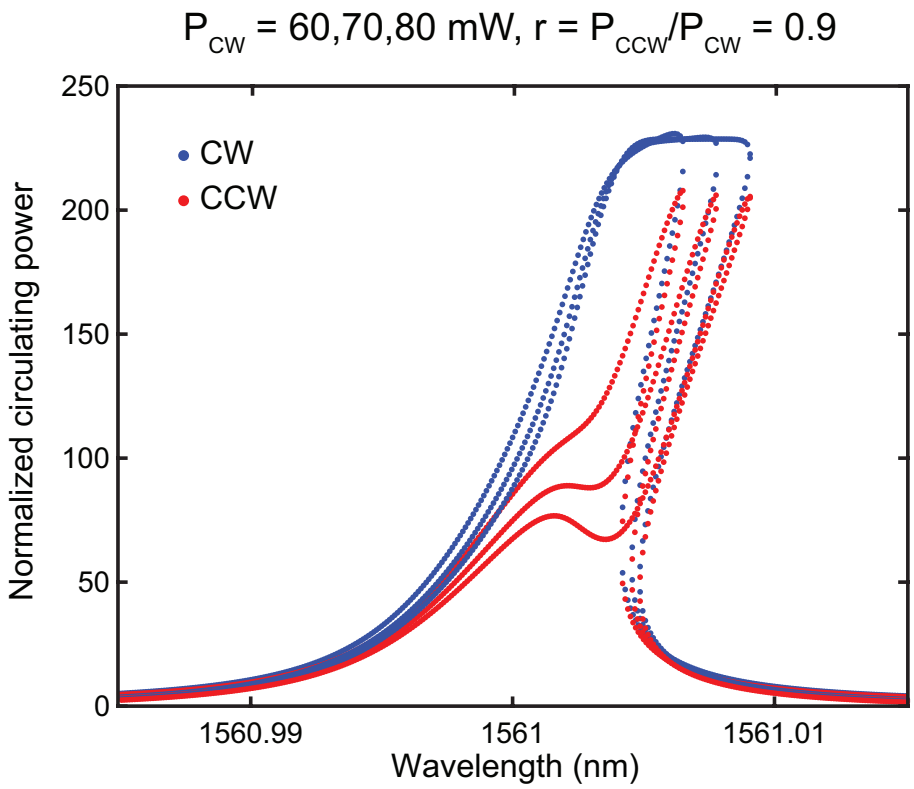

Figure 5.2: The power coupled into the clockwise (blue) and counterclockwise (red) modes for $P_{\text{in,CW}} = 60, 70, 80$ mW and a ratio $r = P_{\text{in,CCW}}/P_{\text{in,CW}} = 0.9$.

5.3 Counter-rotating solitons in a microresonator

In our experiment to generate counter-rotating solitons in such a bidirectionally pumped system Fig. 5.3(a), we pump a single microresonator with a degenerate pump at 1559.79 nm. We amplify this laser with a polarization maintaining (PM) EDFA and split the amplified pump into two parts using a PM 50:50 fiber splitter. The PM components ensure that we maintain the polarization throughout the experimental setup in the TE polarization. The two outputs of the 50:50 splitter are sent to two variable optical attenuators (VOAs). This allows us to independently control the pump power in the CW and CCW directions that lets us control the ratio r as a control knob for the tunability of the generated dual comb source. Another similar experiment performed in silica microresonators

to generate counter-rotating solitons uses a pair of acousto optical modulators to frequency shift a single pump by different frequency shifts to act as a control knob on the tunability of the generated dual comb [124]. The pumps in the CW and CCW directions is connected to port 1 of two circulators. Port 2 of both circulators is connected to a pair of PM-lensed fibers to couple light in and out of the chip. We use the same silicon nitride rings we used previously with a 200-GHz free spectral range (FSR) and a cross section of 950 x 1500 nm that yields anomalous group-velocity dispersion at the pump wavelength that allows thermally controlled soliton generation by controlling the current passed through integrated platinum heaters [115]. We pump an undercoupled resonator with a coupling gap of 500 nm to the bus waveguide. We characterize the generated frequency combs independently of each other Fig. 5.3(b) as well as the generated dual comb after combining the two combs Fig. 5.3(c) [123].

First, we characterize the two combs independently of each other. The combs in the opposite direction are picked off at port 3 of the circulators and split into two parts using a pair of 50:50 splitters. The split outputs are sent to a pair of OSAs and photodetectors to record the pump transmission and optical spectra for the clockwise and counterclockwise combs as seen in Fig. 5.3(b). Using an arbitrary waveform generator, we apply a triangular current ramp on the integrated platinum heaters. We monitor the pump transmission as the resonance frequency is swept across the laser frequency starting with the pump blue detuned with respect to the resonance frequency. We observe the familiar dip in the pump transmission as the pump is close to resonance on the blue detuned side. Tuning further into resonance we observe a high noise state. Beyond this once we cross to the red detuned side of the resonance, we observe the transition to a low noise state on both the clockwise and counterclockwise pump transmis-

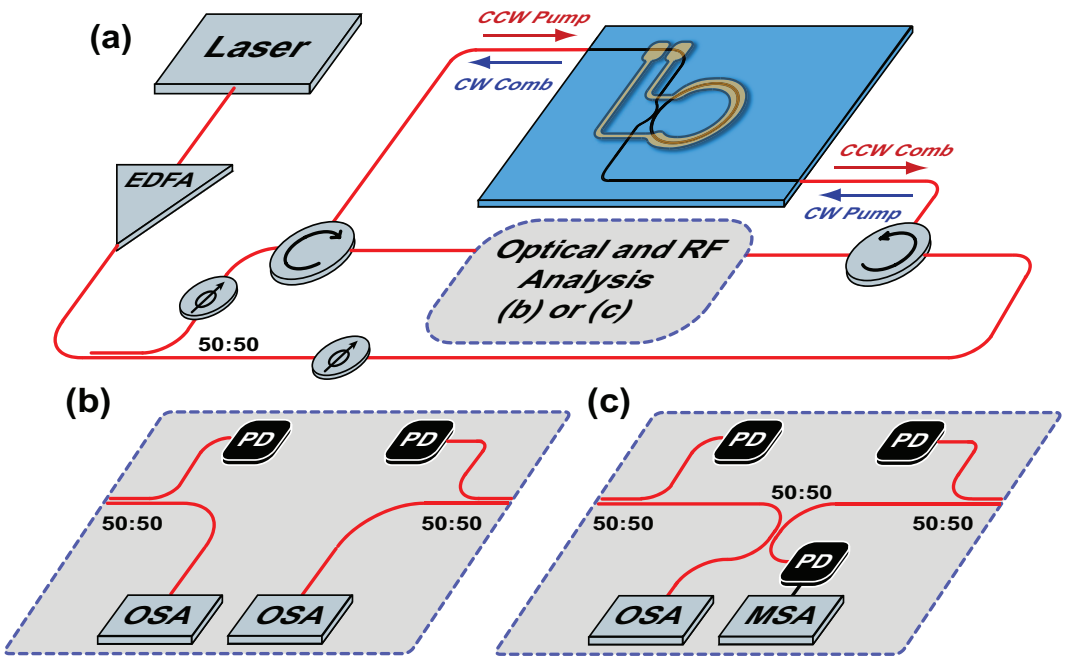

Figure 5.3: (a) Experimental setup to generate counter-rotating solitons in a single microresonator using a single pump laser at 1559.79 nm. The generated counter-rotating solitons are characterized (b) individually, measuring the optical spectra and transmitted optical powers in CW and CCW directions and (c) after combining the dual comb output in both directions to measure the mixed optical and heterodyned RF signal.

sion curves. In Fig. 5.4 we also see signatures of the 'bubble'-like feature on the blue detuned side that appears due to the XPM term in addition to the soliton step before the pump drops out of resonance on the red detuned side.

The soliton step consistently appears at lower pump powers in both directions, and we can tune into this state by terminating the heater scan as soon as the effective detuning in both directions crosses the zero detuning point as seen in Fig. 5.5. We apply a downward ramp on the current starting from a DC level with the pump blue detuned with respect to the resonance frequency. At the end of the downward ramp we apply a flat DC level. The power in the high noise state is close to that in the soliton state and hence we can tune into this state reliably at a reliably slow speed of 200 Hz and don't need to apply a rapid

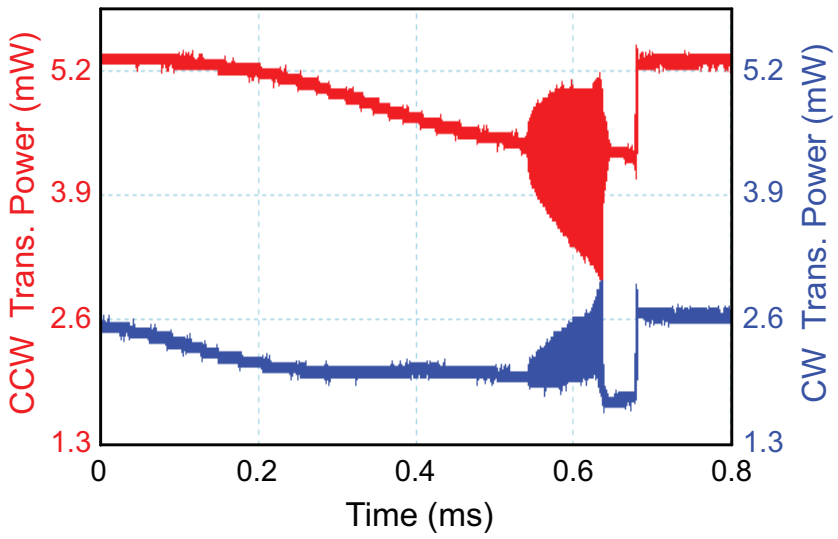

Figure 5.4: Clockwise (blue) and counterclockwise (red) pump transmissions as the resonance frequency is swept across the pump laser starting on the blue detuned side of the resonance frequency and ending on the red detuned side off resonance. We see a characteristic step like feature on the red detuned side past the high noise state.

upward rise at the end of the tuning curve.

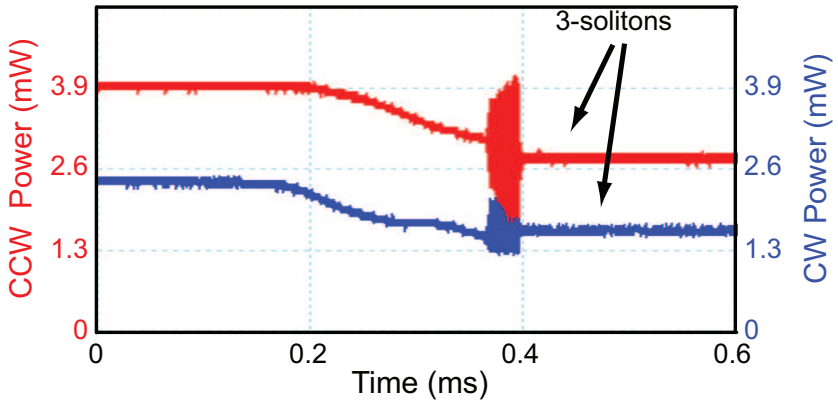

Figure 5.5: Transmitted pump power as detected on the photodetector when a 3 soliton state is generated in both the clockwise (blue) and counterclockwise (red) directions by applying a single downward ramp at a speed of 200Hz on the heater current before terminating the burst at a DC level on the effectively red detuned side for both directions.

The independent optical spectra are also recorded in both directions and are observed to be a 3 FSR state in both directions corresponding to three equally

spaced solitons in the cavity over one round trip as seen in Fig. 5.6. This is characteristic of a harmonically modelocked state as was observed previously in the unidirectionally pumped case.

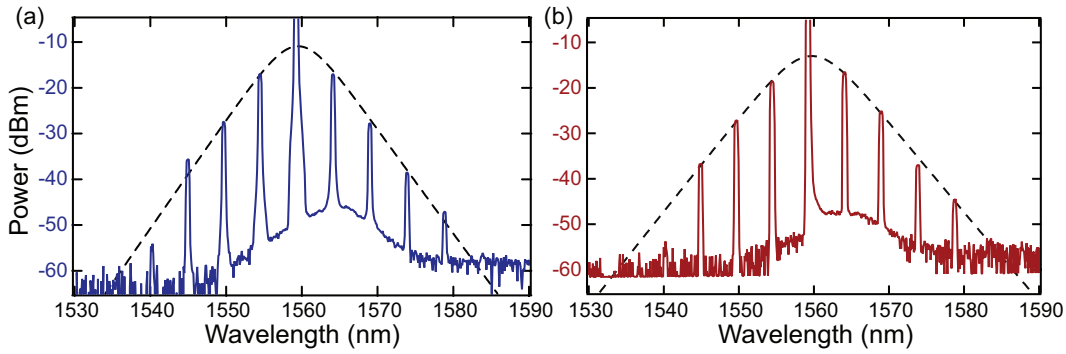

Figure 5.6: Optical spectra recorded on two OSAs as a 3 soliton state is generated in both the clockwise (blue) and counterclockwise (red) directions by applying a single downward ramp at a speed of 200Hz on the heater current before terminating the burst at a DC level on the effectively red detuned side for both directions. The spectra agree well with the hyperbolic secant fit (dashed black).

The setup is then modified to characterize the generated dual comb source. We keep the pump transmission detection independent on two photodiodes. The other half of the split output spectra is send onto a third 50:50 mixer where the two combs are combined. One half of the combined output is sent to an OSA to record the combined optical spectrum. The other half is sent to another photodiode and then onto a MSA that records the heterodyned RF beat notes between the two combs. The counterclockwise to clockwise pump power ratio is set to 0.67. We first record the combined optical spectrum as seen in Fig. 5.7. The spectrum follows the expected 3 FSR spacing and agrees well with the hyperbolic secant fit. The resolution limit of the OSA is 1.25 GHz and we don't see pairs of lines from the combs in the two directions at this minimum setting. This implies that if there is a difference in repetition frequencies between the combs in the two directions, it is less than 1.25 GHz.

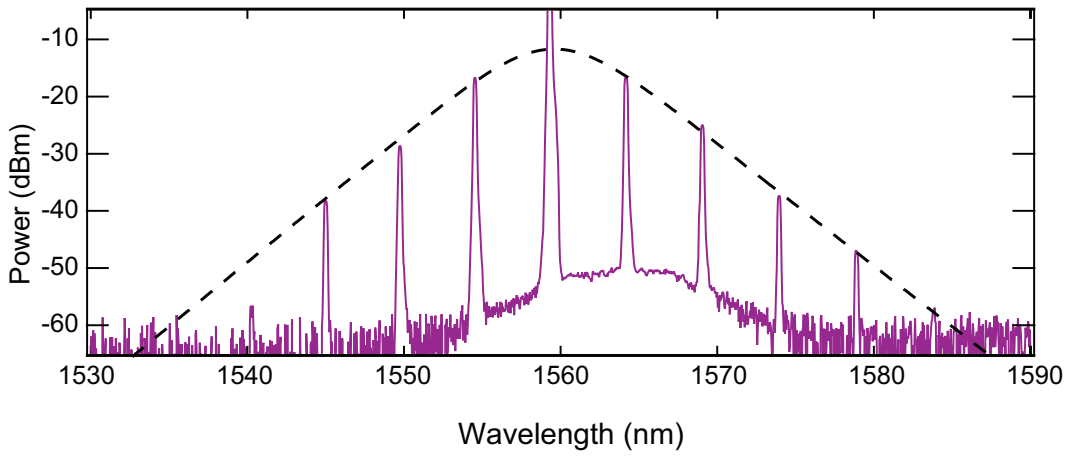

Figure 5.7: Combined optical spectra recorded on an OSA as a 3 soliton state is generated in both directions with a pump power ratio of $r = 0.67$. The resolution limit of the OSA of 1.25 GHz prevents us from seeing the pair of lines from the combs in the two directions. The combined spectrum agrees well with the hyperbolic secant fit (dashed black).

We then look at the heterodyne RF spectrum between the two combs by detecting the combined combs on a high bandwidth photodetector (≥ 250 MHz) and recording the RF spectrum on a MSA. The recorded RF spectrum shows a series of equally spaced peaks at 19 MHz as seen in Fig. 5.8. Since the first beat note appears as a result of the third pair of lines, the actual repetition frequency difference Δf_r between the two soliton trains is 6.3 MHz (or 1/3 the frequency of the first beat note).

As the pump power ratio is adjusted and the counter-rotating 3 soliton state is reinitialized, we observe the tunability of the recorded beat notes. The multiplicative factor of 2 on the nonlinear phase introduced by the XPM as compared to the SPM introduces an asymmetry in the effective detuning for the CW and CCW modes. So, even if the pump laser is degenerate at a fixed wavelength and the current applied to the integrated heaters shifts the resonance for both directions equally that makes the detuning introduced by the heater common to both modes, the additional SPM and XPM terms cause an inequality in the

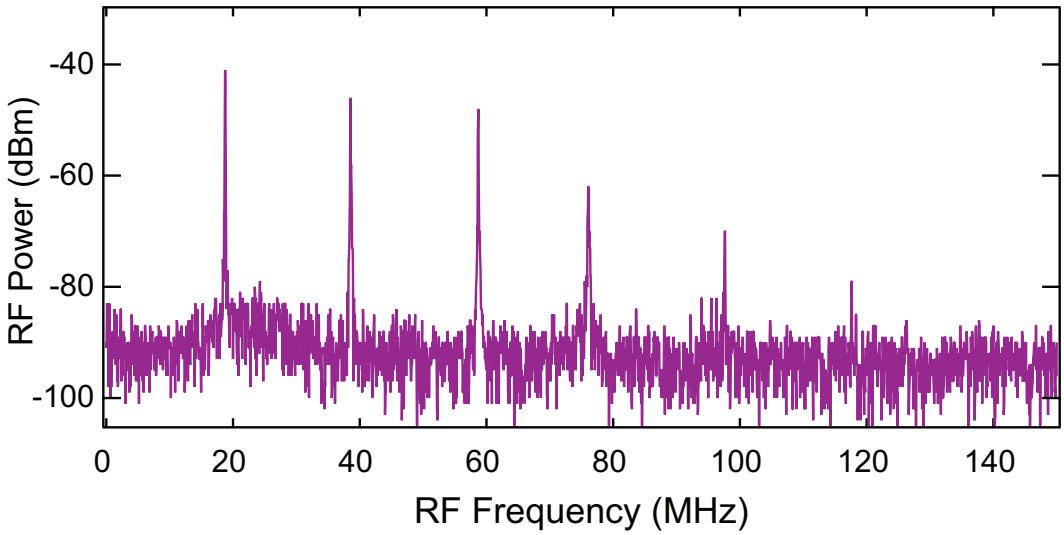

Figure 5.8: Combined RF spectra recorded on a MSA by detecting the mixed comb on a high bandwidth photodetector as a 3 soliton state is generated in both the clockwise (blue) and counterclockwise (red) directions with a pump power ratio of r = 0.67. The spectrum is recorded with a 100 kHz resolution bandwidth implying a minimum coherence time of 10 μs for the generated dual comb.

pump-cavity detuning. The effective detuning for the clockwise and counterclockwise modes can be defined in terms of the detuning of the laser δ_{p} with respect to the thermally shifted cavity resonance frequency after applying a heater current ω_0 as determined by the resonance condition Eq. 3.9 and the nonlinear shift introduced by the SPM and XPM terms for the corresponding powers in the clockwise and counterclockwise directions [155]. The effective detuning in both directions is given by,

$$\delta\omega_{\mathrm{CW}} = \delta_{\mathrm{p}} + \frac{\omega_0 n_2}{n_{\mathrm{eff}} A_{\mathrm{eff}}}(P_{\mathrm{circ,CW}} + 2P_{\mathrm{circ,CCW}}) \tag{5.3}$$

$$\delta\omega_{\mathrm{CCW}} = \delta_{\mathrm{p}} + \frac{\omega_0 n_2}{n_{\mathrm{eff}} A_{\mathrm{eff}}}(P_{\mathrm{circ,CCW}} + 2P_{\mathrm{circ,CW}}) \tag{5.4}$$

As previous studies have established [103,158], the intracavity soliton power for solitons generated in a microresonator depends on the effective detuning of the pump and has a square root relationship to the detuning and other waveg-

uide parameters given by,

$$P_{\text{sol}} = \frac{2\ A_{\text{eff}}}{\omega_0\ n_2}\sqrt{-2\ c\ \beta_2\ n_{\text{eff}}\ \delta\omega} \tag{5.5}$$

The soliton pulse width also depends on the detuning and has a inverse square root relationship that is given by,

$$\tau_{\text{sol}} = \sqrt{\frac{-c\ \beta_2}{2\ n_{\text{eff}}\ \delta\omega}} \tag{5.6}$$

The is the average power of the soliton over a round trip (τ_r) which implies the peak power of the soliton, based on the hyperbolic secant function $P_0\text{sech}^2(t/\tau_{\text{sol}})$ integrated over a round trip from $-\tau_r/2$ to $\tau_r/2$ is given by $P_0 = \frac{P_{\text{sol}}\tau_r}{2\tau_{\text{sol}}}$. Combining the above equations, we get the intracavity soliton peak power that has a near linear relationship with the detuning to be,

$$P_0 = \frac{2\ c\ A_{\text{eff}}\ \tau_{\text{r}}}{\omega_0\ n_2\ L}\delta\omega \tag{5.7}$$

The intracavity fields consist of two components in both direction, the solitons and the continuous wave pump fields. This means that for each of the four components there are four possible interactions, SPM due to itself, and XPM due to the other three components. At the detuning where we expect the solitons to be generated, the CW background field is a lot weaker than the peak soliton power, so we neglect the XPM effect of the CW pumps on the soliton peak. So the only effect that we consider is the SPM due to the soliton acting on itself as it propagates around the cavity. The accumulated phase shift over one round trip results in a change in the effective index that the soliton experiences

over one round trip. This results in a change in the repetition rate for the soliton due to this phase accrued. The induced change in the repetition frequency ∂f_{r} is given by,

$$f_{\mathrm{r}} = \frac{c}{n_{\mathrm{eff}}\, L} \tag{5.8}$$

$$\partial f_{\mathrm{r}} = \frac{c}{L}\left(\frac{\Delta n_{\mathrm{eff}}}{n_{\mathrm{eff}}^2}\right) \tag{5.9}$$

$$\partial f_{\mathrm{r}} = f_{\mathrm{r}}\left(\frac{\Delta n_{\mathrm{eff}}}{n_{\mathrm{eff}}}\right) \tag{5.10}$$

The Δn_{eff} due to the SPM by the soliton on itself is $g\, n_2 P_0/A_{\mathrm{eff}}$, where g is the factor for the nonlinear phase shift induced by the dissipative soliton on itself. That leads to a difference of repetition rates between the solitons in the CW and CCW directions given by,

$$\Delta f_{\mathrm{r}} = |f_{\mathrm{CW}} - f_{\mathrm{CCW}}| = g\frac{n_2\, f_{\mathrm{r}}}{A_{\mathrm{eff}}\, n_{\mathrm{eff}}}|P_{\mathrm{sol,CW}} - P_{\mathrm{sol,CCW}}| \tag{5.11}$$

$$\Delta f_{\mathrm{r}} = g\frac{2\, f_{\mathrm{r}}}{\omega_0}|\delta\omega_{\mathrm{CW}} - \delta\omega_{\mathrm{CCW}}| \tag{5.12}$$

The Δf_{r} can thus be related to the pump cavity detuning and pump powers by Eq.5.3,Eq.5.4, and Eq.5.12. The enhancement due to the resonator, coupling losses at the output facet, and insertion losses for the fiber components before the light circulating in the CW direction reached the photodetector is combined into the term η. This gives us the relationship between the intracavity pump power and transmitted pump power as $P_{\mathrm{circ,CW}} = \eta P_{\mathrm{out}}$. A reasonable assumption to make at the detuning at which we operate, is that the factor η is the same for both directions to first order which means the intracavity ratio of powers r

can be assumed to be the same as that as measured on the photodetectors based on the transmitted power.

Combining the above analysis, we get a normalized measure for the difference in repetition rates $\Delta f_{\mathrm{r}}/P_{\mathrm{out}}$ that can be expressed in material parameters, P_{out}, and the ratio r between the powers in both directions that is given by,

$$\frac{\Delta f_{\mathrm{r}}}{P_{\mathrm{out}}} = g\frac{2\, n_2\, f_{\mathrm{r}}}{n_{\mathrm{eff}}\, A_{\mathrm{eff}}}\, \eta\, |1 - r|. \tag{5.13}$$

We then sweep the pump power in the bus waveguide in both directions over a range of 1.35 to 6.1 mW and measure the corresponding $\frac{\Delta f_{\mathrm{r}}}{P_{\mathrm{out}}}$ at various values of the ratio r. The recorded values are binned based on the ratio r into bins that are 0.02 wide and all the points within that bin are averaged into a single $\frac{\Delta f_{\mathrm{r}}}{P_{\mathrm{out}}}$ value. The fluctuations in the transmitted power as a result of the interference between the strong pump in the two directions makes this binning necessary. The tuning curve for $\frac{\Delta f_{\mathrm{r}}}{P_{\mathrm{out}}}$ is shown in Fig. 5.9

The tuning curve shows two interesting regimes of operation as the ratio r between the pump powers is varied. At ratios far from 1, we observe that the value of $\frac{\Delta f_{\mathrm{r}}}{P_{\mathrm{out}}}$ is in reasonable agreement with our simple model for the tunability given by Eq. 5.13. The large error bars on some of the points and some deviations from the expected behavior occur due to the aforementioned fluctuations that limit the accuracy of the measurements.

At ratios close to 1, within a region from 0.9 to 1.1, we do not observe a beat note. The recorded optical spectra also show signs of interference on each line that would imply that each pair of lines is identical in frequency. This behavior seems to indicate that the soliton trains in both directions are synchronized to

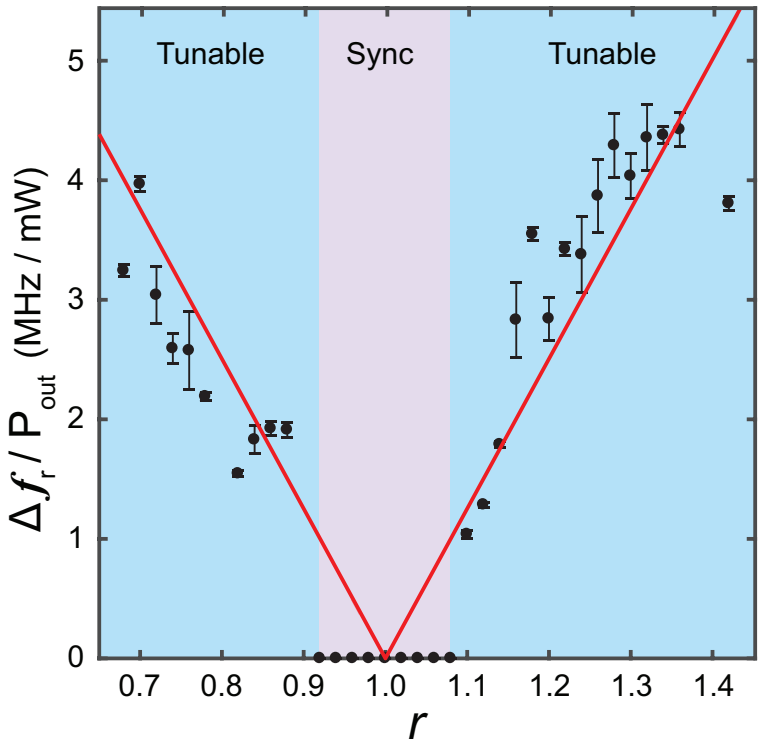

Figure 5.9: The difference in repetition rate normalized to the power in the clockwise mode ($\Delta f_{\mathrm{r}}/P_{\mathrm{out}}$) as a function of the power ratio r. Each of the measured points from the experiment is binned over a 0.02 window in r and plotted as a black dot. The red curve represents the theoretical curve from Eq. 5.13.

each other. A more detailed study on synchronization was performed in silicon nitride microresonators [138] that goes into great detail about synchronization behaviour. The behavior observed here in Fig. 5.9 is similar to the behavior observed in that experiment.

In conclusion, we observe counter-rotating cavity solitons in a single silicon nitride microresonator using a single fixed frequency pump laser. We demonstrate the ability to tune the difference in the repetition frequency of the two soliton trains by varying pump power for the modes in the clockwise and counterclockwise directions. Using a single-frequency laser and a single microresonator eliminates common mode noise in the dual-comb source.

The interferometric fluctuations that are created by the degenerate pump that we use in our case strongly affect the ability to stabilize the dual comb source. Future designs could incorporate splitting of the pump on chip and using structures such as integrated Mach Zehnder interferometers, potentially also give us the ability to control the pump power ratios on-chip using phase shifters. Such an approach would have the potential for an extremely compact dual-comb source with significantly reduced uncorrelated noise.

CHAPTER 6

OFFSET LOCKED DUAL-COMB SOURCES FOR RANGING

Microresonator based dual comb sources, as we have seen can be used for spectroscopy of species of interest in the near infrared [137, 149] and most importantly in the mid infrared within the so called 'molecular fingerprint' region where the strongest vibrational absorption features of molecules arise based on their energies [148]. In these spectroscopy measurements the signal comb is passed through the sample and combined with the reference comb. The recorded interferogram is then measured and a Fourier transform yields the RF spectrum. By doing a measurement without the sample, a baseline reference measurement of the spectrum can be performed. When the recorded RF spectrum including the absorption is normalized to this baseline, the spectrum can be measured.

Another powerful application of dual combs is ranging [95, 96]. Pulsed sources have regularly been used to characterize distances using time of flight measurements. A single pulse sent over a certain delay and detected would limit the resolution to the pulse width and also the bandwidth of the photodetector in being able to resolve the pulse and its delayed copy. A potential approach to improving the detection is to use the interferograms created by using two combs with different repetition rates. Similar to spectroscopy using a dual comb source, in ranging, one comb still acts as a local oscillator and the second comb acts as a signal comb that probes the target to acquire distance information. However, in this case the recorded interferograms are analyzed differently. We create two copies of the signal soliton, one of which is sent to a reflector at a known 'zero' position to create a reference interferogram. A second interfero-

gram is created from the second copy of the signal soliton that is reflected off the 'target' position. The distance between the zero position and the target position L_{delay} leads to a time delay in the signal soliton of $\tau_{delay} = 2\,L_{delay} / c$ for propagation through the delay distance in air as it goes to the target and back. After the delay, the signal soliton and the delayed copy of it are mixed with the LO comb and this results in two interferograms one from the overlap of the signal comb reflected at the 'zero' plane with the LO comb and one from the overlap of the signal comb reflected from the target plane with the LO comb. Fig. 6.1 gives an outline of this ranging measurement.

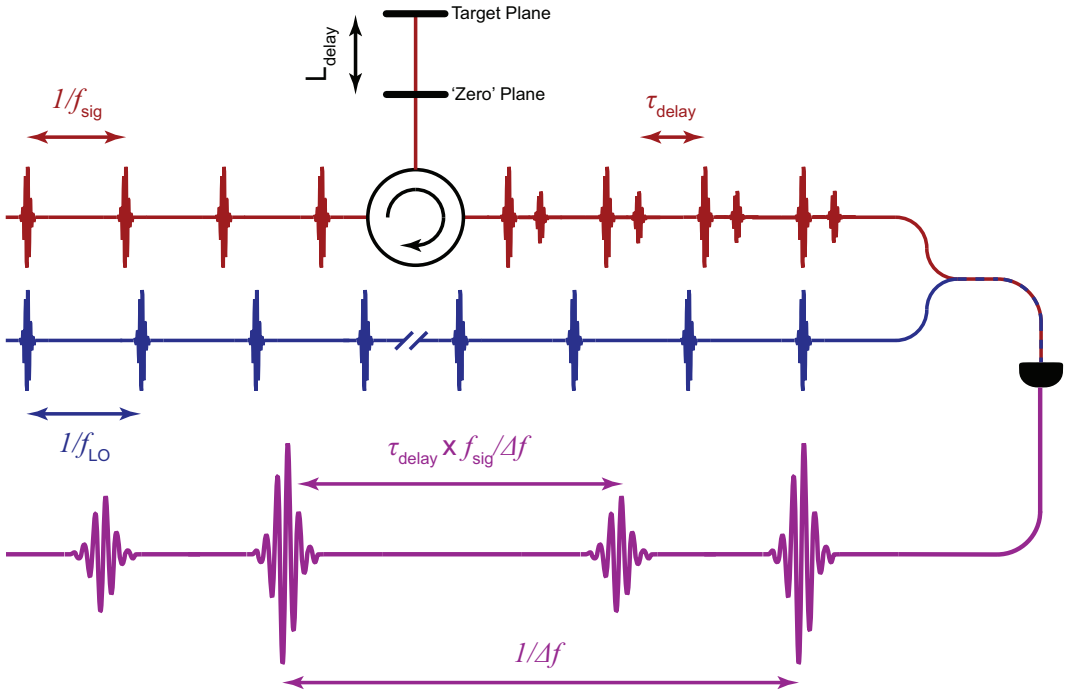

Figure 6.1: Schematic of a ranging measurement using a dual comb source. The signal comb is reflected off a 'zero' plane and a target plane to create two copies of the resulting interferogram when it is mixed with the local oscillator comb. The delay between the two interferograms can be used to measure the distance between the 'zero' plane and the target plane.

As we can see here, the interferogram repeats every $1/\Delta f$ where $\Delta f = |f_{LO} - f_{sig}|$. The interferogram created by this effectively magnifies the time

axis of the signal comb by a factor of $f_{sig}/\Delta f$. This allows for detection of the distance to a greater precision limited only by the detector bandwidth and the speed at which the detector output voltage can be sampled using a data acquisition tool such as a fast real-time oscilloscope or a digitizer board. If the delay time is increased by the repetition rate of the signal soliton to $\tau_{delay}+1/f_{sig}$ we get an identical interferogram as the original τ_{delay}. This leads to an ambiguity in the measured distance corresponding to increases in the delay time by integer multiples of $1/f_{sig}$. The ambiguity distance therefore corresponds to $L_{amb} = \frac{c}{2\ f_{sig}}$. For a 200 GHz soliton train the ambiguity distance will be 0.7494 mm.

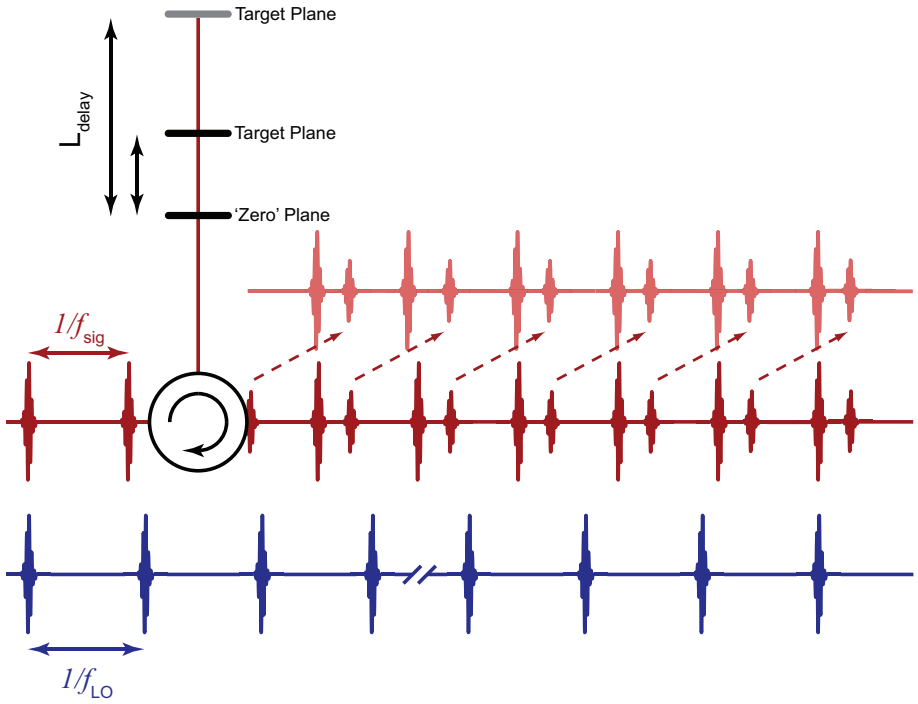

Figure 6.2: The amibiguity in the ranging measurement results from identical interferograms created when the delay time increases by integer multiples of $1/f_{sig}$ that limits the ranging measurement. The ambiguity distance therefore corresponds to $L_{amb} = \frac{c}{2\ f_{sig}}$. This ambiguity needs to be lifted in order to perform a precise ranging measurement over long distances.

Lifting the ambiguity on ranging measurements can be achieved by changing f_{sig}. At a different value of f_{sig} the corresponding ambiguity distance L_{amb}

will be different resulting in a shift in the measured interferogram. This shift will allow us to lift the ambiguity in the distance to be measured. Heaters allow for independent control of two ring resonators that can generate soliton mode-locked combs with slightly different repetition rates. These can then act as the LO and signal combs that can be used as a source for an integrated solid state ranging scheme.

Independent heater controls on two ring resonators allow us to force the repetition frequency of the signal comb soliton train to be locked at a frequency offset to the repetition frequency of the LO comb soliton train. The offset frequency is derived from a tunable reference RF source. Tuning of the RF frequency of the reference allows for tuning of the Δf by acting on the heater to control f_{sig}.

6.1 Phase detection and frequency locking

When two frequencies are driven to be identical to each other using a phase locked loop, the difference in phase is driven to zero by a feedback mechanism. Signals at two frequencies ω_1 and ω_2 have phase terms that are given by $\phi_1 = \omega_1 t + \alpha$ and $\phi_2 = \omega_2 t + \beta$. In order to drive the the phase difference between the two to zero, the phase has to be detected and can serve as an error signal in a feedback loop where it can be locked to zero (or a fixed DC level given by $(\alpha - \beta)$.

An electrical mixer can be used as a phase detector [159]. The mixer multiplies the two inputs that are sent to it. The two inputs can be assumed to be $\cos(\omega_1 t + \alpha)$ and $\cos(\omega_2 t + \beta)$. The output of the mixer can be broken into the sum of two terms using the trigonometric identity for the product of cosines as

follows,

$$\cos(\omega_1 t+\alpha)\times\cos(\omega_2 t+\beta)=\frac{1}{2}\big[\cos((\omega_1+\omega_2)t+(\alpha+\beta))+\cos((\omega_1-\omega_2)t+(\alpha-\beta))\big] \tag{6.1}$$

The output of the mixer has components at the sum and difference frequencies. Typically when a mixer is used as a phase detector, a $\pi/2$ phase shift is applied on one of the inputs converting that into a sine wave. It operates as a phase detector in a regime where the input frequencies $\omega_1 \approx \omega_2 = \omega$ that results in a vanishing $\omega_1 - \omega_2$. This results in an output that is the sum of two sine waves given by,

$$\cos(\omega t+\alpha)\times\sin(\omega t+\beta)=\frac{1}{2}\big[\sin(2\omega t+(\alpha+\beta))+\sin(\alpha-\beta)\big] \tag{6.2}$$

The output has a component that purely depends on the phase of the two waves, $(\alpha - \beta)$ and a sum frequency component at double the frequency 2ω. The high frequency component is filtered and the remaining output is the low frequency component dependent on the phase difference. In the low phase difference limit, the small angle approximation can be used and yields the phase difference as the output, $\sin(\alpha - \beta) \approx (\alpha - \beta) = \Delta\phi$.

In the case of optical frequency locking. The difference between two optical signals f_1 & f_2 is detected as a RF beat note at $\Delta f_{\text{rep}} = f_1 - f_2$. If this frequency difference is to be driven to a specific value, a RF reference frequency corresponding to this value (f_{RF}) is sent to one of the inputs of a phase detector, the beat note Δf_{rep} is sent to the other input. The phase detector detects the differ-

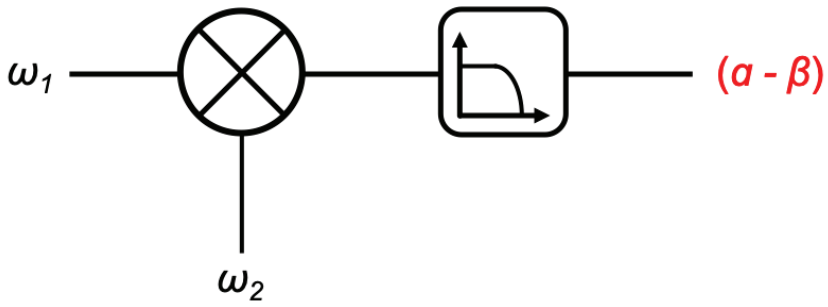

Figure 6.3: A schematic of an electrical mixer as a phase detector. The output of the phase detector filters out the sum frequency component and the remaining low frequency component is proportional to the phase difference between the two waves $(\alpha - \beta)$ when $\omega_1 \approx \omega_2 = \omega$.

ence between the phase of the two inputs and leads to a phase term given by $\eta \times sin(\Delta f_{\text{rep}} - f_{\text{RF}})t$. The output of the phase detector acts as an error signal and is then sent through feedback electronics that act on the frequency difference between the two optical frequencies. This might be in a master slave configuration where f_1 remains free running and the feedback acts on f_2. Or it might drive any other optical interaction that modifies Δf_{rep}. In our case the difference between the two soliton repetition rates appears as the first beat note between the two combs at Δf_{rep}. This can then be compared to a frequency reference derived from a RF source. The phase locked loop, as seen in Fig. 6.4 acts on the effective detuning of one of the soliton trains by modifying the current on its heater and disciplines it to be at a fixed offset frequency from the other by driving $f_1 - f_2$ to f_{RF}. In this case, the PID controller and actuator determine the bandwidth of the feedback loop. As we saw earlier in Section 4.3, the bandwidth of the heaters rolls off beyond ≈20 kHz which becomes the limiting bandwidth of the feedback loop.

The limitation on bandwidth of the feedback means that the feedback mechanism will only be able to respond to a frequency difference of upto 20 kHz

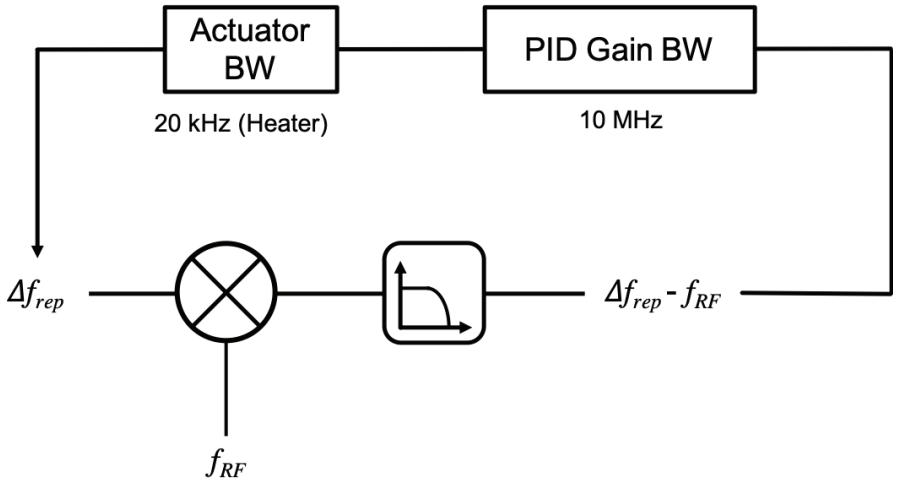

Figure 6.4: A schematic of the locking loop used to lock the difference in frequency of the two soliton trains Δf_{rep} to a RF reference frequency f_{RF}.

between Δf_{rep} and f_{RF}. This allows for a frequency excursion of only 40 kHz for Δf_{rep} around f_{RF} before the lock is broken as a result of it being beyond the feedback bandwidth. Typically, the frequency excursion of Δf_{rep} is a lot larger than 40 kHz. This means that a different approach to generating an error signal is required. The phase detector can only track a phase difference from $-\pi$ to π which limits the frequency excursion within which the feedback loop can account for the phase difference to the bandwidth of the heaters. If we can unwrap the phase, this would allow for a greater frequency excursion within which the frequency lock can be engaged.

The approach we use for phase unwrapping is to use a digital phase detector that can extend the range beyond $-\pi$ to π. We use a digital phase detector, (Menlo Systems DXD 200) to detect the phase difference between Δf_{rep} and f_{RF}. The DXD 200 operates using a counter that counts up or down depending on which input leads or lags the other. The maximum count on the counter allows us to unwrap the phase as the two frequencies vary. The DXD 200 allows for phase unwrapping up to $\pm 32\pi$ of phase. This results in a 32 fold extension

of the frequency excursion over which the lock can be engaged to $\geq$1.3 MHz. An adapted schematic of the phase detection using the digital phase detector is shown in Fig. 6.5

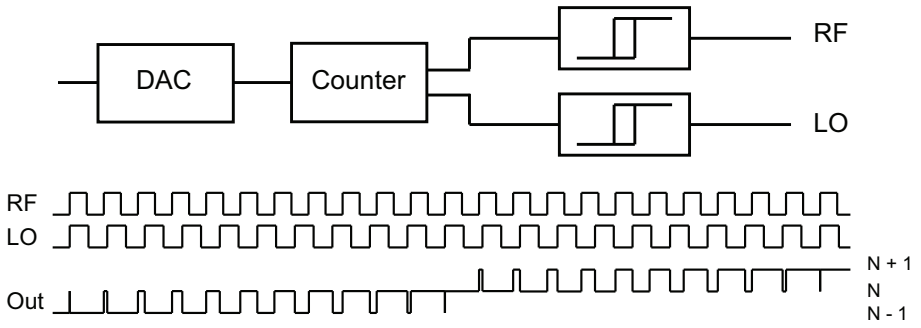

Figure 6.5: A schematic of the phase detection using the digital phase detector adapted from [160]. The DXD 200 uses a counter to unwrap the phase over $\pm 32\pi$. This extends the frequency excursion over which the lock can be engaged.

6.2 Dual comb generation and tunable offset locking

We use a scheme in which soliton modelocked combs are generated on two nearly identical ring resonators. The pump laser is shared by the two resonators. As seen in the schematic of the chip in Fig. 6.6, the pump is split on chip using a multimode interference power splitter [161,162]. The soliton generation in both ring resonators is independently controlled using a pair of platinum heaters. The two output waveguides are placed at a separation of 200 μm on the output facet that allows for them to be simultaneously collected using a single aspheric lens without significant distortion that would reduce the output coupling efficiency. The outputs are spatially separated allowing for each of the combs to be collected independently in fiber using a pair of fiber collimation packages to act as the signal and LO comb.

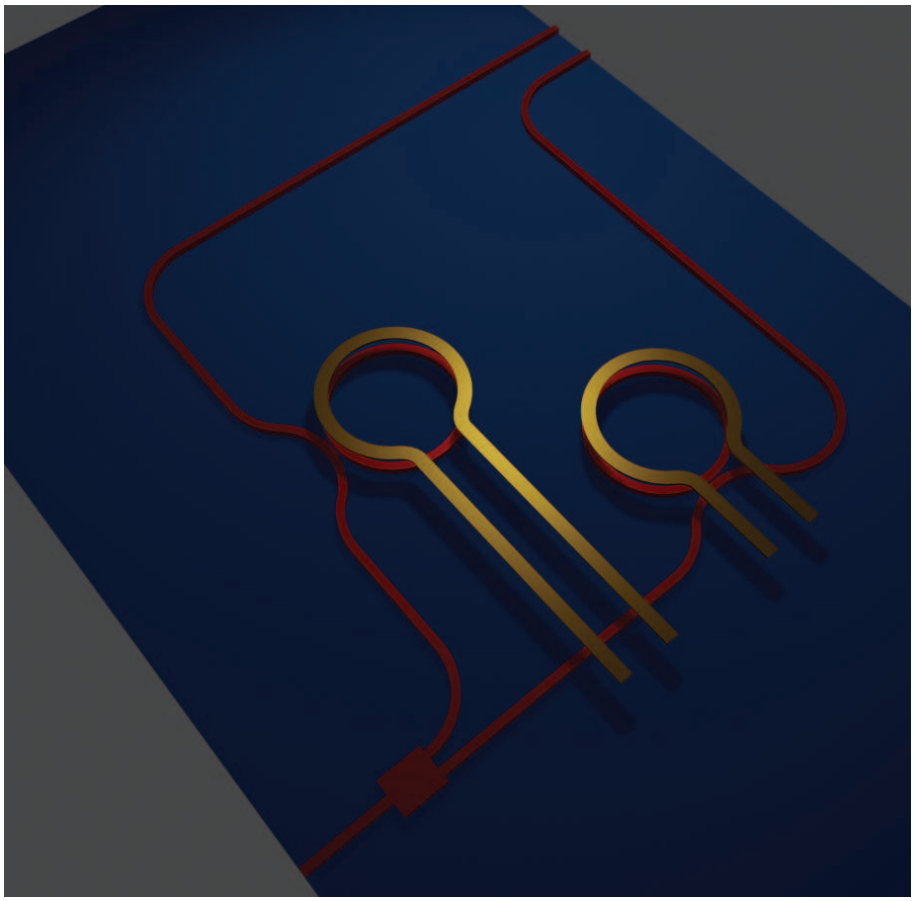

Figure 6.6: A schematic of the chip used to generate the dual comb source for ranging on an integrated device. The two ring resonators are independently controlled using a pair of integrated heaters to generate soliton trains with slightly different repetition rates. The two outputs are spatially separated that allows for them to be collected using a single aspheric lens and sent to two fiber collimation packages to act as the signal and LO comb.

We generate solitons in the two rings using a two-channel arbitrary waveform generator to control the heaters on both ring resonators independently. We tap 1% of each of the two comb outputs using a pair of 99:1 fiber splitters and combine the two using a 50:50 fiber mixer. One of the outputs of the 50:50 mixer is sent to an amplified photodetector (Thorlabs PDA10-CS) where the Δf_{rep} is detected. We use this detected beat note to lock the offset frequency Δf_{rep} to a RF reference f_{RF}. The detected Δf_{rep} electrical signal is sent to one input of a digital phase detector (Menlo Systems DXD 200) and the RF reference frequency f_{RF} is

sent to the other input. The slope of the measured phase determines whether Δf_{rep} leads or lags f_{RF}. The detected phase acts as the error signal that is passed through the PID Servo Loop (Vescent Photonics D2-125) and combined with one of the output of the arbitrary waveform generator using an OpAmp adder circuit with unity gain. The ring with the feedback acts as the slave resonator and when the lock is engaged the slave soliton train maintains a difference in repetition frequency of f_{RF} from the repetition rate of the master soliton train. A schematic of the setup used to generate an offset locked dual comb source is shown in Fig. 6.7.

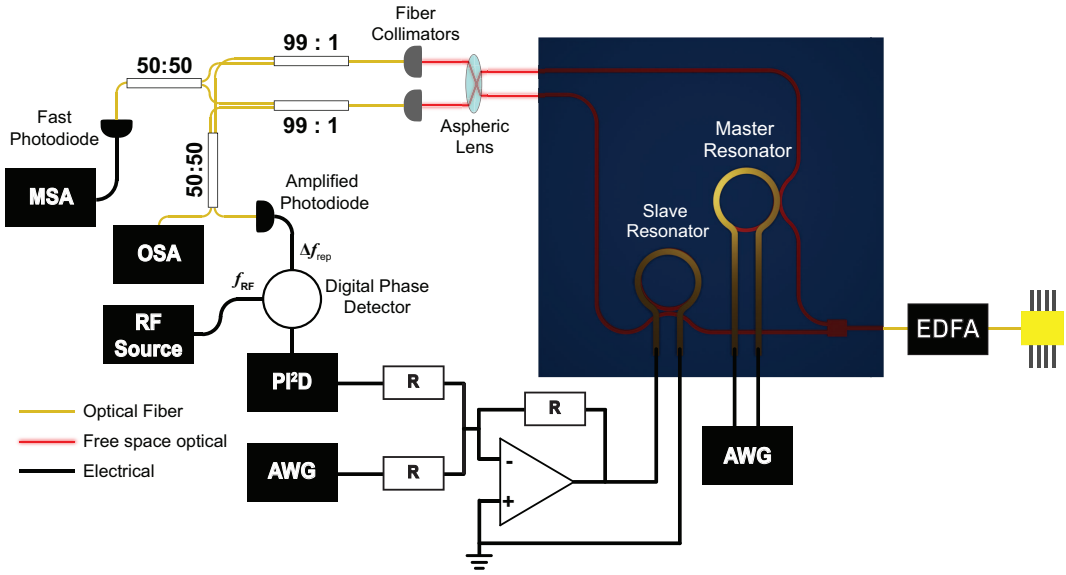

Figure 6.7: A schematic of the setup used to generate an offset locked dual comb source. The comb outputs are collected using Fiber collimators and analyzed using in the optical domain using an OSA, in the RF domain using a fast photodiode and an MSA. 1% of the outputs are tapped, mixed and detected on a amplified photodiode to determine the Δf_{rep} which is then compared to f_{RF} using a digital phase detector. The error signal thus generated is sent to a PI^{2}D servo controller and the servo output is combined with the signal from the arbitrary waveform generator (AWG) that controls soliton generation in the slave resonator using a summing amplifier with unity gain and fed back to the heaters for the slave resonator to establish a lock at $\Delta f_{\text{rep}} = f_{\text{RF}}$.

We set f_{RF} to 15 MHz and detect the phase difference between this and Δf_{rep}

detected on the amplified photodetector. The output of the phase detector does an excursion over ± 2 V that corresponds to $\pm 32\pi$. The frequency of this phase excursion is 32 times slower than $\Delta f_{\text{rep}} - f_{\text{RF}}$ and the slope of the phase curve indicates whether Δf_{rep} is higher than f_{RF} or lower. The detected phase is shown in Fig. 6.8.

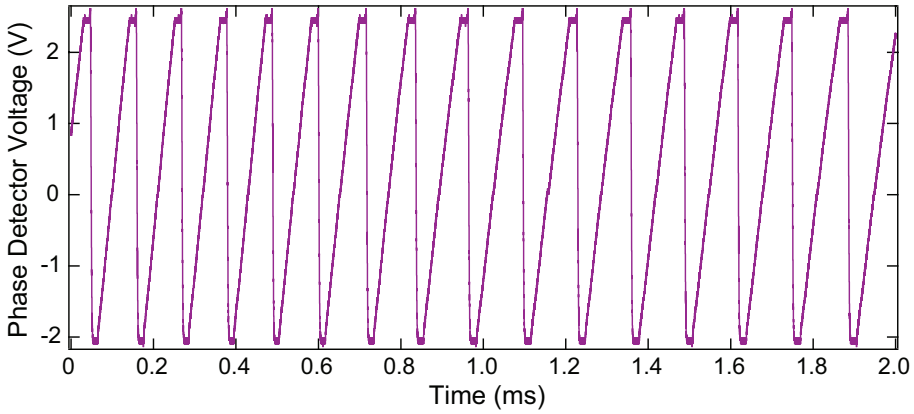

Figure 6.8: The output of the phase detector when a free running beat note Δf_{rep} is compared to a fixed f_{RF} = 15 MHz. The frequency of the phase curve indicates $\Delta f_{\text{rep}} - f_{\text{RF}}$ and slope indicates the direction of Δf_{rep} with respect to f_{RF}

The detected phase is then attenuated and acts as the error signal input $e(t)$ of a PID Servo controller (Vescent Photonics D2-125) that enables a PI^{2}D feedback loop. The first integrator can eliminate slow drift at low frequencies while the second integrator acts on higher frequencies to enable the lock. The correction signal can be expressed as $r(t)$,

$$r(t) = K_p\, e(t) + \int_0^{t_1} K_{i1}\, e(t)dt + \int_0^{t_2} K_{i2}\, e(t)dt + K_d \frac{d\, e(t)}{dt} \tag{6.3}$$

The servo output is then connected to an adder circuit to combine it with the output of the arbitrary waveform generator that is used to generate the slave soliton. The adder circuit is designed to have unity gain and have an output current that is high enough to be able to drive the heaters to the desired current

levels to generate a soliton. The correction signal $r(t)$ has a small amplitude close to zero. Initially it is set to zero and adds to the DC voltage level established by the generation of the soliton state. As we saw earlier in Chapter 5, the soliton repetition rate depends on the effective detuning and by sending the small correction signal $r(t)$ to the heaters the detuning can be controlled to maintain the f_{sig} at a fixed frequency offset of f_{RF} from the free running f_{LO}. To determine the approximate amplitude of the required correction signal, we switch the servo controller to ramp mode and look for turning points in the error signal that will establish a lock point. The lock point corresponds to the amplitude of the ramp signal at the locations of the turning points and in this case is ≈6 mV. This correction signal corresponds to a current correction of 25 μA applied to the heater of the signal comb.

Once the lock points have been established we engage the lock. If there is any drift in the Δf_{rep} arising from environmental fluctuations or power fluctuations in the pump or other effects, the correction signal accounts for that to drive it back to f_{RF}. By locking the difference in frequency to f_{RF}, we ensure that the interferogram detected will repeat every $1/f_{\text{RF}}$. We look at the RF spectrum of the recorded interferogram and observe a series of RF tones at multiples of Δf_{rep}.

We also look at the relative drift of the free running dual comb and compare it to the stable locked dual comb in Fig. 6.10. Both spectra are recorded over 5 ms with a resolution bandwidth of 100 Hz and a frequency span of 1 MHz from 14.5 to 15.5 MHz on a RF spectrum analyzer (Rohde & Schwarz FSWP50). In the free running case, we observe a drift of ≈200 kHz over the 5 ms sweep time. In the locked case the drift is significantly reduced as can be seen from the

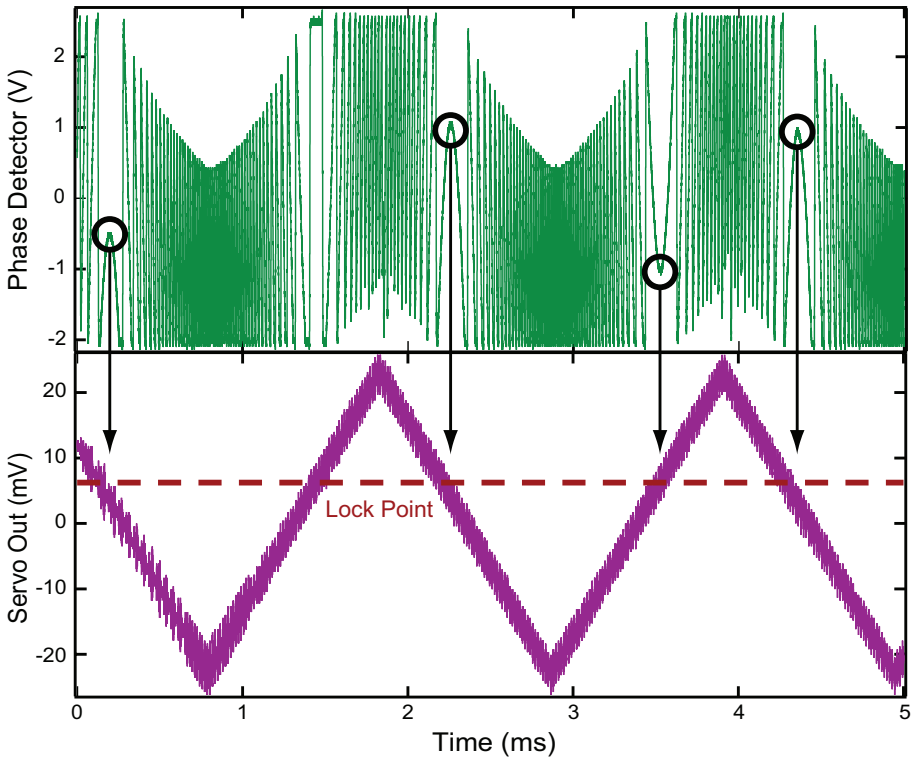

Figure 6.9: When the servo output is switched to a ramp mode, turning points can be identified (black circles) in the error signal that can be used to identify the lock point on the ramp (dashed red line). In this case the lock point appears at an amplitude of ≈6 mV.

inset of the figure.

We also study the tunability of the dual comb source as the reference RF freuqency f_{RF} is tuned with the lock engaged. As we discussed previously, acting on f_{sig} can be used to lift the ambiguity in a ranging measurement. In our case, to tune Δf_{rep} we act on the signal comb so tunability of the dual comb source will allow for ambiguity free ranging over larger distances. We engage the lock with f_{RF} = 12 MHz. We then tune the f_{RF} in steps of 100 kHz to 14.5 MHz. We record the first 5 RF tones of the dual comb as this is done. The RF beat notes follow the f_{RF} without the lock being disengaged. The RF beatnotes were recorded with a higher resolution bandwidth in this case (200 kHz) over a

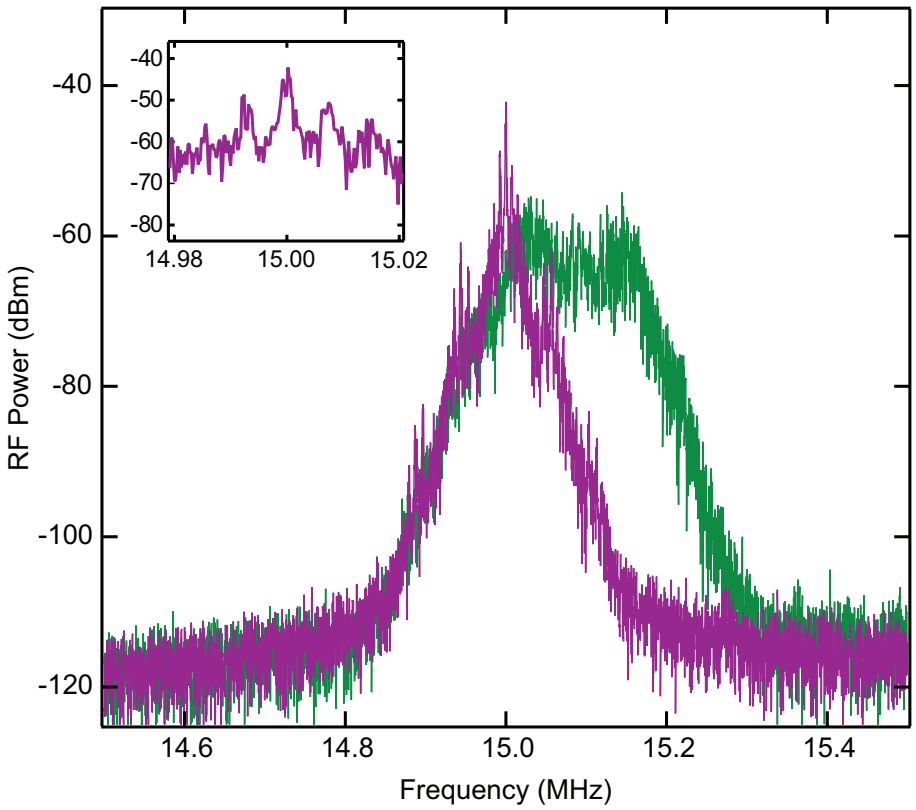

Figure 6.10: Comparison of the locked (violet) and unlocked (green) RF spectrum of the first beat note between the signal and LO combs. We see a significant narrowing of the RF beat note when the lock is engaged. Both spectra are recorded over 5 ms with a resolution bandwidth of 100 Hz and a frequency span of 1 MHz from 14.5 to 15.5 MHz on a RF spectrum analyzer (Rohde & Schwarz FSWP50).

wider span from DC to 70 MHz to include the first 5 RF beatnotes. The tunable dual comb is shown in Fig. 6.11.

This tunable dual comb source can be used to perform distance ranging and lift the ambiguity on the measured distance.

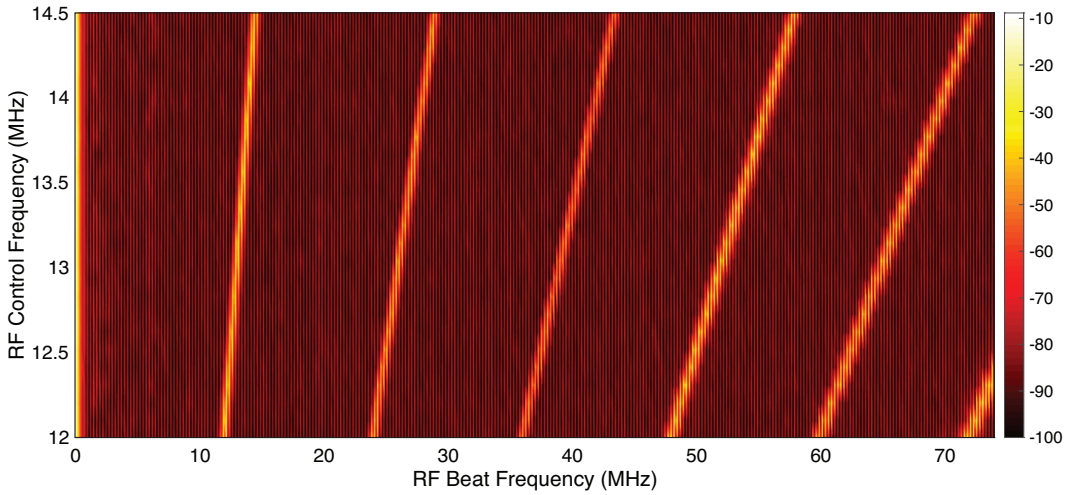

Figure 6.11: Tuning of the dual comb source generated with the offset frequency Δf_{rep} between the two combs locked to f_{RF} as it is varied in steps of 100 kHz from 12 MHz to 14.5 MHz. The first 5 RF tones are recorded over a span from DC to 70 MHz with a resolution bandwidth of 200 kHz.

6.3 Ambiguity free ranging using a tunable dual comb source

Ranging using dual combs has a limitation that we discussed previously. This limitation is introduced in the measurement due to the ambiguity in the recorded interferogram. If the signal comb is delayed by exactly the repetition rate of its pulses, the interferogram will be identical. So any distance that corresponds to a delay in integer increments of the signal pulse repetition rate $1/f_{\text{sig}}$ as we saw in Fig. 6.2, cannot be distinguished. This ambiguity can be lifted by tuning f_{sig}.

For a ranging measurement, the distance between a reference and target is to be characterized. The time of flight light between the reference and target planes leads to a delay. For a distance that is beyond the ambiguity range determined by the signal comb, the delay time is τ_{del} and is given by,

$$\tau_{\text{del}} = \frac{N}{f_{\text{sig}}} + \tau \tag{6.4}$$

where N is an integer and τ lies between 0 and $1/f_{\text{sig}}$.

The delayed copy of the target interferogram is effectively magnified by a factor of $f_{\text{sig}}/\Delta f$ where Δf is the offset frequency between the LO comb and signal comb established by the offset lock. The observed delay between the reference interferogram and target interferogram arises from τ and is given by,

$$t = \tau \times \frac{f_{\text{sig}}}{\Delta f} \tag{6.5}$$

If we operate the offset locked dual comb at two offset frequencies by tuning the reference RF frequency $f_{\text{RF}} = \Delta f_1$ & Δf_2 resulting in the repetition rate of the signal comb being set to $f_{\text{sig,1}}$ & $f_{\text{sig,2}}$. The time delay can be expressed in terms of the two signal comb repetition rates as,

$$\tau_{\text{del}} = \frac{N}{f_{\text{sig,1}}} + \tau_1 \tag{6.6}$$

$$\tau_{\text{del}} = \frac{N}{f_{\text{sig,2}}} + \tau_2 \tag{6.7}$$

In this case $f_{\text{sig,1}}$ and $f_{\text{sig,2}}$ are on the order of 200 GHz while the heater induced tuning is on the order of 1 MHz. This lifts the ambiguity on the measured distance upto a point where the two delays do not share the same integer number of periods of the signal comb. This imposes a secondary ambiguity when the corresponding integer numbers differ by 1. In order for this to be the case, we would require $f_{\text{sig,1}}/f_{\text{sig,2}} = (N+1)/N = 1 + 1/N$. In the case of a 1 MHz change to a 200 GHz signal comb repetition rate, this implies a value of $N = 200000$. The new limit for ambiguity free ranging is thus raised from 0.75 mm, for a 200 GHz repetition frequency comb to 150 m. For smaller differences between $f_{\text{sig,1}}$ and $f_{\text{sig,2}}$, the $f_{\text{sig,1}}/f_{\text{sig,2}} = 1 + 1/N$ relation would imply an

even higher range. However this would come at the cost of a higher difficulty in distinguishing differences between the interferograms that is limited by the photodetector and data acquisition bandwidths.

The delay on the two recorded interferograms t_1 and t_2 that can be measured from the measurements, according to Eq. 6.5, are given by,

$$t_1 = \tau_1 \frac{f_{\text{sig,1}}}{\Delta f_1} \tag{6.8}$$

$$t_2 = \tau_2 \frac{f_{\text{sig,2}}}{\Delta f_2} \tag{6.9}$$

We plug the values t_1 and t_2 from Eq. 6.8 and 6.9 back into the original equations for the delay time, Eq.6.6 and 6.7 and eliminate N from these two equations to arrive at an expression for τ_{del} completely in terms of measurable or known quantities,

$$\tau_{\text{del}} f_{\text{sig,1}} - t_1 \Delta f_1 = \tau_{\text{del}} f_{\text{sig,2}} - t_2 \Delta f_2 \tag{6.10}$$

$$\tau_{\text{del}} (f_{\text{sig,1}} - f_{\text{sig,2}}) = t_1 \Delta f_1 - t_2 \Delta f_2 \tag{6.11}$$

Since the combs operate in a master slave configuration, assuming negligible drift in the LO comb, $f_{\text{sig,1}} = f_{\text{LO}} + \Delta f_1$ and $f_{\text{sig,2}} = f_{\text{LO}} + \Delta f_2$ giving us,

$$\tau_{\text{del}} = \frac{t_1 \Delta f_1 - t_2 \Delta f_2}{\Delta f_1 - \Delta f_2} \tag{6.12}$$

and the delay distance to be,

$$\text{L}_{\text{del}} = \frac{t_1 \Delta f_1 - t_2 \Delta f_2}{\Delta f_1 - \Delta f_2} \frac{c}{2} \tag{6.13}$$

The setup for the ranging is as shown in Fig. 6.12. The two combs are collected from the spatially separated output on the chip using a single aspheric lens. A portion of the collimated output beams is collected on a pair of photodetectors using the Fresnel reflection from a glass slide to monitor the pump transmission. The pump transmission is used to ensure the generation of a single soliton modelocked state on both the LO and signal combs using the procedure explained in Chapter 4. We use a pair of silicon nitride ring resonators with a FSR of 200 GHz with the pump split on chip using a MMI splitter as shown in Fig. 6.6.

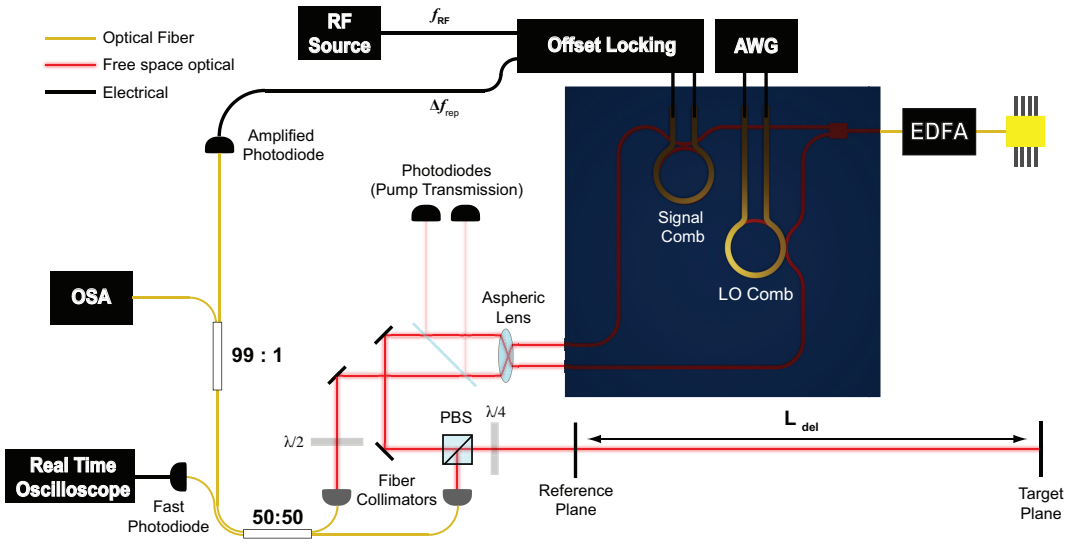

Figure 6.12: A schematic of the setup used for ambiguity free ranging using a offset locked dual comb source. The signal comb is sent to a free space circulator consisting of a PBS and a QWP. It is reflected off a reference plane and a target plane separated by the distance to be detected (L_{del}) to create two copies of the signal comb and collected in fiber using a collimator. The polarization of the LO comb is rotated by $\pi/2$ using a HWP and coupled into fiber. The signal and LO combs are mixed using a fiber 50:50 splitter and one half of the output is sent to a real time oscilloscope the record the interferograms. The other half is split further using a 99:1 splitter where the weaker portion is sent to an OSA to monitor the spectrum and the stronger portion is sent to an amplifier photodetector to determine the offset frequency of the two combs Δf_{rep} that is then locked to f_{RF}.

The signal comb is then sent through a polarizing beam splitter (PBS) and a

quarter wave plate (QWP). This configuration acts as a circulator. The incoming linearly polarized (TE) light passes through the PBS unperturbed at which point the QWP makes it circularly polarized. The reflections from the reference and target planes flip the handedness of the circularly polarized light. As the light passes through the QWP a second time the polarization goes back to linearly polarized, but rotated at an angle of $\pi/2$ with respect to the incoming light. This then which then reflects off the PBS instead of going back towards the chip. The two copies of the signal comb thus generated are coupled into a fiber using a fiber collimator. The polarization of the LO comb is rotated by $\pi/2$ using a half wave plate (HWP) and is then coupled into fiber using a fiber collimator. The two combs are then combined using a 50:50 fiber splitter. One half of the combined output is sent to a to a fast photodiode with a bandwidth of $\geq$12.5 GHz (EO Tech 3500-F) and the interferograms are recorded using a real time oscilloscope (Keysight DSOZ634A). The other half of the combined combs is split further using a 99:1 fiber splitter. The stronger portion of this is filtered using a WDM filter to get rid of the strong pump laser and sent to an amplified photodiode (Thorlabs PDA-10CS) to detect the difference in repetition rates. This is then used to derive the error signal and lock the difference in repetition rate Δf to a external RF source at a frequency of f_{RF} as discussed in Section 6.2.

We use two value of f_{RF}, 12 MHz and 13 MHz to perform an ambiguity free distance measurement. We first record the interferogram by setting the value of f_{RF} to be 12 MHz. The recorded trace has a repetition period of 83.3 ns ($\frac{1}{12\text{ MHz}}$) and has two peaks corresponding to the interferograms generated from reflections off the reference and target planes. The higher peak (negative amplitude) corresponds to the stronger reference reflection and the weaker peak corresponds to the target reflection. The interferogram is recorded over 838 μs

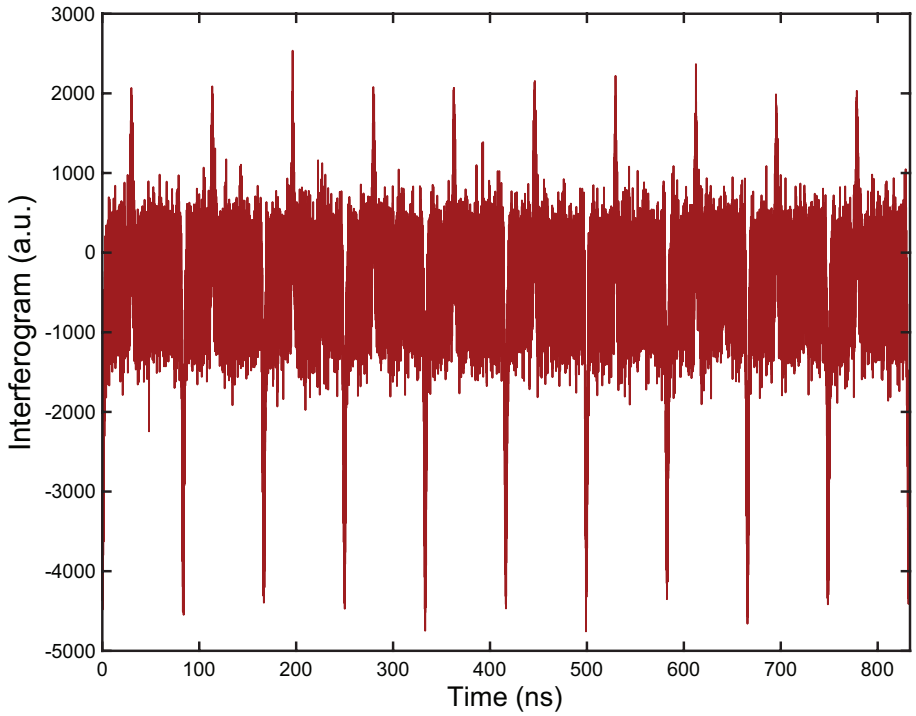

Figure 6.13: The raw interferogram when the difference between the LO and signal comb is locked to 12 MHz. The trace corresponds to 10 periods of the interferogram and clearly shows the two distinct interferograms from the reference plane as well as weaker interferograms corresponding to a weaker reflection from the target plane.

corresponding to 10066 periods of the interferogram. The raw interferogram over 10 periods (830 ns) is shown in Fig 6.13

We then repeat this measurement with the f_{RF} set to 13 MHz and record 10895 periods of the interferogram over 838 μs. As expected, again we observe the two interferograms from the reference plane and the target plane as expected with a period of 76.9 ns (or $\frac{1}{13\ \mathrm{MHz}}$). The raw interferogram over 10 periods for this 13 MHz offset locked dual comb is shown in Fig. 6.14.

The raw interferograms are then processed to reduce the noise and extract the amplitudes of the signals over each period. In some cases the period of the interferograms is observed to drift away from the lock point and those time pe-

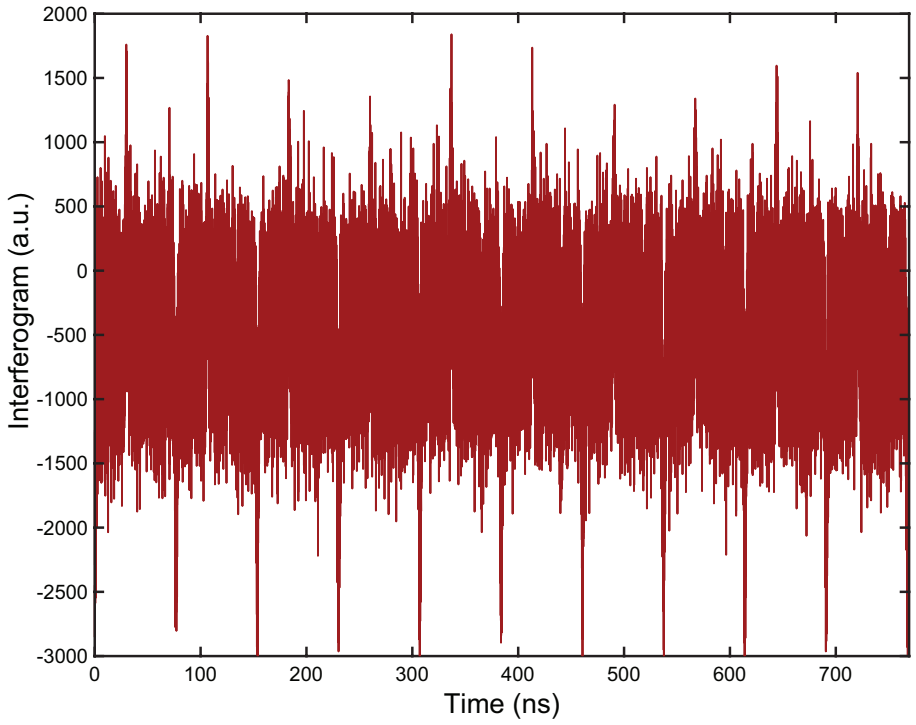

Figure 6.14: The raw interferogram when the difference between the LO and signal comb is locked to 13 MHz. The trace corresponds to 10 periods of the interferogram and clearly shows the two distinct interferograms from the reference plane as well as weaker interferograms corresponding to a weaker reflection from the target plane.

riods where the period of the interferogram is off by more than 2.5 kHz in either direction from the lockpoints of 12 and 13 MHz are eliminated. This results in processed interferograms examples of which are seen in Fig. 6.15 and Fig. 6.16 from which the delays t_1 and t_2 can be extracted that will be used to infer τ_{del} using Eq. 6.12.

From the recorded interferograms, we estimate t_1 = 29.88$\pm$0.17 ns for the 12MHz lockpoint. From the 13 MHz lockpoint interferogram we infer t_2 to be 29.76$\pm$0.19 ns. These delays are recorded in the slow time axis of the interferograms and are converted to the fast axis of the signal comb using Eq. 6.8 and Eq. 6.9. Using Eq. 6.12, to determine the ambiguity free delay time these

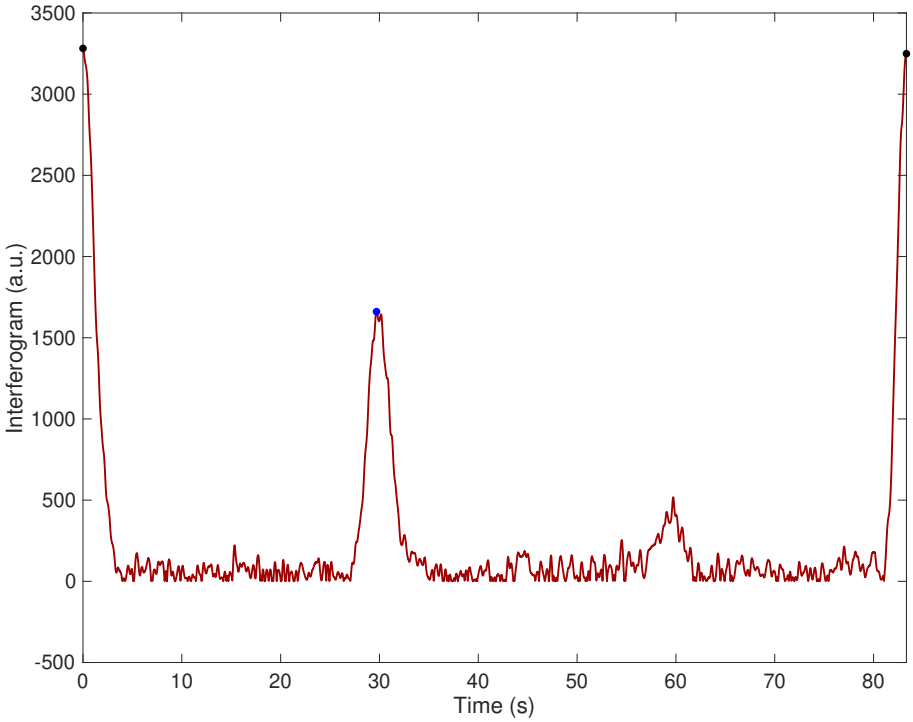

Figure 6.15: A processed interferogram for the 12 MHz lockpoint that yields t_1 that can be used to infer the value of the delay in conjunction with t_2 from the interferogram recorded at the lockpoint of 13 MHz.

measurements yield a delay time τ_{del} of 28.38 ns. This implies a ambiguity free distance L_{del} of 4.25 m. However, the errors on the delay measurements t_1 and t_2 impose limits on the ambiguity free range measurement that limit the accuracy to $L_{\text{del}} = 4.25 \pm 0.35$ m. The distance between the reference plane and target plane is characterized using conventional measurement tools and is given by $L = 4.03 \pm 0.002$ m that falls within the error of the detected distance. A more precise measurement of the delay times t_1 and t_2 will be required to drive down the errors in the ambiguity free measurement. This can be achieved with a tighter lock on the offset frequency between the signal and LO combs as well as minimizing drift of the LO comb. The LO comb is free-running in this configuration which means that the signal comb repetition rate might be drifting even if the offset is locked.

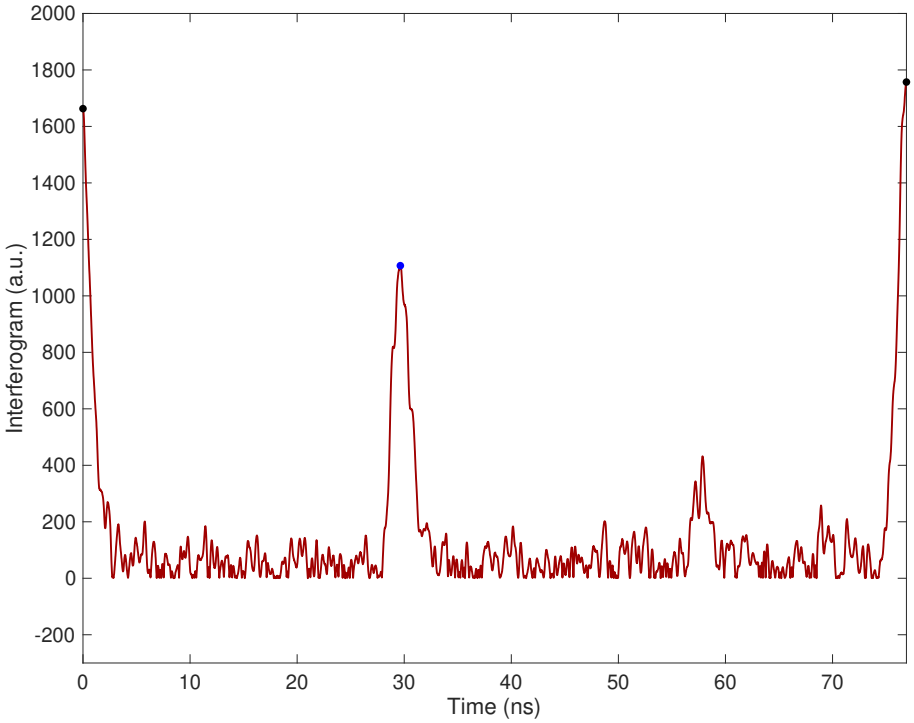

Figure 6.16: A processed interferogram for the 13 MHz lockpoint that yields t_2 that can be used to infer the value of the delay in conjunction with t_1 from the interferogram recorded at the lockpoint of 12 MHz.

CHAPTER 7

RELATED WORK AND FUTURE WORK

The ability to readily generate soliton modelocked combs on a silicon nitride microresonator platform using thermal control has enabled several applications that have already been demonstrated. Silicon Nitride dual combs have been used to perform spectroscopy of liquid phase dichloromethane [137]. A pair of nearly identical silicon nitride microresonators on separate chips have been synchronized to each other using a fiber link [138]. Such a system could act as clocks that are synchronized to each other through an optical link. Synchronization has also been shown in subharmonic and harmonic regimes where solitons with repetition rates that are multiples of each other are synchronized [139]. An integrated comb source using an indium phosphide gain chip and a high quality silicon nitride ring as a end mirror has been shown to lase with a very narrow linewidth [163] as well as generate soliton modelocked combs [141]. Solitons have also been generated in the visible frequency range using thermal control of higher order modes in silicon nitride [140]. Work has also been done to stabilize the solitons over long periods of time using feedback on the heaters [164] and tune the pump laser and have the soliton follow [165].

Thermal control of resonances has also been applied to other regimes of operation such as using a dual cavity configuration, where the output of the ring resonator is fed back to an EDFA that causes the system to lase at a particular mode of the ring resonator, a thermally tunable comb source was used to measure gas phase spectra of acetylene [166]. In the normal group velocity dispersion regime, thermal tuning has been used to build a turnkey high efficiency comb source in silicon nitride microresonators by using heaters to control the

strength of mode interactions between coupled rings [128].

A potentially more stable and integrated source for tunable counter-rotating solitons using a single microresonator could be designed with an on chip splitter and Mach-Zehnder interferometer to control the relative pump powers. This would help alleviate some of the limitations of the counter-rotating solitons as seen in the work presented in this dissertation and potentially generate extremely low noise RF tones by eliminating common mode noise between the two soliton trains.

Future work on offset locked sources includes the possibility of expanding upon the ideas of synchronization [138,139] to utilize on chip coupling between two resonators with repetition rates separated from each other. This would present the most extreme case of synchronization since the coupling between the two combs will occur at a single line far from the pump line. A tighter lock on the Δf in such an offset locked dual comb source would allow significantly improved precision in the range measurements without requiring a feedback servo or being limited by the bandwidth of the heaters. This will allow for the heaters to be a tuning mechanism independent of the locking scheme to lift the ambiguity on the ranging measurement.

Another potential configuration for optical feedback to establish a offset lock would pick off a single line (n^{th} line) from the master comb, apply a phase modulation with a large enough voltage on this comb line to drive its entire power into sidebands at $\pm f_{RF}$. These sidebands are then fed into the slave resonator to establish injection locking. If the coupling is strong enough to establish the injection lock this would result in an offset locked dual comb at f_{RF}/n.

A fully integrated comb source with laser, detector and control electronics all on a single chip would be the holy grail of on-chip frequency comb technology [Fig. 7.1. Several pieces of this puzzle have been solved by previous research on integrated frequency combs. The work presented in this dissertation adds to this body of work that could eventually lead to a realization of this vision of a fully integrated frequency comb source for spectroscopy, ranging and many more applications. If such a vision can be realized these sources could see mass adoption at scale.

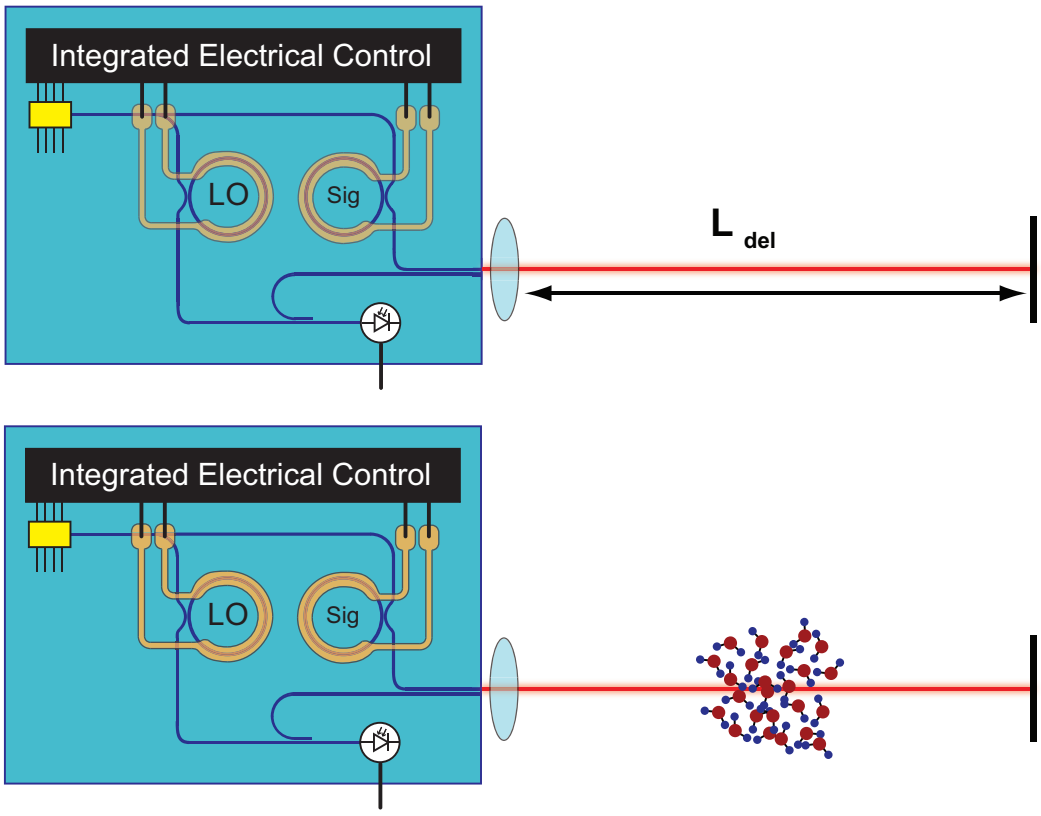

Figure 7.1: A vision for a fully integrated comb source with laser, detector and control electronics all on a single chip for applications in ranging and spectroscopy.

BIBLIOGRAPHY

[1] A. L. Schawlow and C. H. Townes, "Infrared and optical masers," Phys. Rev. **112**, 1940–1949 (1958).

[2] T. H. Maiman, "Stimulated Optical Radiation in Ruby," Nature **187**, 493–494 (1960).

[3] G. E. Moore, "Cramming more components onto integrated circuits," Electronics **38** (1965).

[4] R. W. Boyd, *Nonlinear Optics* (Elsevier, 2003), 3rd ed.

[5] P. A. Franken, A. E. Hill, C. W. Peters, and G. Weinreich, "Generation of optical harmonics," Phys. Rev. Lett. **7**, 118–119 (1961).

[6] J. D. Jackson, *Classical Electrodynamics* (Wiley, 1999), 3rd ed.

[7] G. Agrawal, *Nonlinear Fiber Optics* (Elsevier / Academic Press, 2013), 5th ed.

[8] K. Ikeda, R. E. Saperstein, N. Alic, and Y. Fainman, "Thermal and Kerr nonlinear properties of plasma-deposited silicon nitride/silicon dioxide waveguides," Opt. Express **16**, 12987–12994 (2008).

[9] J. S. Levy, A. Gondarenko, M. A. Foster, A. C. Turner-Foster, A. L. Gaeta, and M. Lipson, "CMOS-compatible multiple-wavelength oscillator for on-chip optical interconnects," Nature Photonics **4**, 37 (2009).

[10] D. J. Moss, R. Morandotti, A. L. Gaeta, and M. Lipson, "New CMOS-compatible platforms based on silicon nitride and Hydex for nonlinear optics," Nature Photonics **7**, 597–607 (2013).

[11] J. A. Giordmaine and R. C. Miller, "Tunable coherent parametric oscillation in $LiNbO_3$ at optical frequencies," Phys. Rev. Lett. **14**, 973–976 (1965).

[12] L. E. Hargrove, R. L. Fork, and M. A. Pollack, "Locking of He–Ne laser modes induced by synchronous intracavity modulation," Applied Physics Letters **5**, 4–5 (1964).

[13] S. A. Diddams, "The evolving optical frequency comb," J. Opt. Soc. Am. B **27**, B51–B62 (2010).

[14] T. Udem, J. Reichert, R. Holzwarth, and T. W. Hänsch, "Absolute optical frequency measurement of the cesium d_1 line with a mode-locked laser," Phys. Rev. Lett. **82**, 3568–3571 (1999).

[15] T. Udem, J. Reichert, R. Holzwarth, and T. W. Hänsch, "Accurate measurement of large optical frequency differences with a mode-locked laser," Opt. Lett. **24**, 881–883 (1999).

[16] S. A. Diddams, T. Udem, J. C. Bergquist, E. A. Curtis, R. E. Drullinger, L. Hollberg, W. M. Itano, W. D. Lee, C. W. Oates, K. R. Vogel, and D. J. Wineland, "An Optical Clock Based on a Single Trapped $^{199}Hg^{+}$ Ion," Science **293**, 825–828 (2001).

[17] D. J. Jones, S. A. Diddams, J. K. Ranka, A. Stentz, R. S. Windeler, J. L. Hall, and S. T. Cundiff, "Carrier-envelope phase control of femtosecond mode-locked lasers and direct optical frequency synthesis," Science **288**, 635–639 (2000).

[18] S. A. Diddams, D. J. Jones, J. Ye, S. T. Cundiff, J. L. Hall, J. K. Ranka, R. S. Windeler, R. Holzwarth, T. Udem, and T. W. Hänsch, "Direct link between microwave and optical frequencies with a 300 THz femtosecond laser comb," Phys. Rev. Lett. **84**, 5102–5105 (2000).

[19] R. Holzwarth, A. Nevsky, M. Zimmermann, T. Udem, T. Hänsch, J. von Zanthier, H. Walther, J. Knight, W. Wadsworth, P. Russell, M. Skvortsov, and S. Bagayev, "Absolute frequency measurement of iodine lines with a femtosecond optical synthesizer," Applied Physics B **73**, 269–271 (2001).

[20] T. Udem, S. A. Diddams, K. R. Vogel, C. W. Oates, E. A. Curtis, W. D. Lee, W. M. Itano, R. E. Drullinger, J. C. Bergquist, and L. Hollberg, "Absolute frequency measurements of the Hg^{+} and Ca optical clock transitions with a femtosecond laser," Phys. Rev. Lett. **86**, 4996–4999 (2001).

[21] T. Udem, R. Holzwarth, and T. W. Hansch, "Optical frequency metrology," Nature **416**, 233–237 (2002).

[22] H. Telle, G. Steinmeyer, A. Dunlop, J. Stenger, D. Sutter, and U. Keller, "Carrier-envelope offset phase control: A novel concept for absolute optical frequency measurement and ultrashort pulse generation," Applied Physics B **69**, 327–332 (1999).

[23] M. Niering, R. Holzwarth, J. Reichert, P. Pokasov, T. Udem, M. Weitz,

T. W. Hänsch, P. Lemonde, G. Santarelli, M. Abgrall, P. Laurent, C. Salomon, and A. Clairon, "Measurement of the hydrogen $1S$- $2S$ transition frequency by phase coherent comparison with a microwave cesium fountain clock," Phys. Rev. Lett. **84**, 5496–5499 (2000).

[24] V. Gerginov, C. E. Tanner, S. A. Diddams, A. Bartels, and L. Hollberg, "High-resolution spectroscopy with a femtosecond laser frequency comb," Opt. Lett. **30**, 1734–1736 (2005).

[25] S. A. Diddams, L. Hollberg, and V. Mbele, "Molecular fingerprinting with the resolved modes of a femtosecond laser frequency comb," Nature **445**, 627–630 (2007).

[26] K. C. Cossel, F. Adler, K. A. Bertness, M. J. Thorpe, J. Feng, M. W. Raynor, and J. Ye, "Analysis of trace impurities in semiconductor gas via cavity-enhanced direct frequency comb spectroscopy," Applied Physics B **100**, 917–924 (2010).

[27] I. Coddington, W. C. Swann, and N. R. Newbury, "Coherent multiheterodyne spectroscopy using stabilized optical frequency combs," Phys. Rev. Lett. **100**, 013902 (2008).

[28] M. T. Murphy, T. Udem, R. Holzwarth, A. Sizmann, L. Pasquini, C. Araujo-Hauck, H. Dekker, S. D'Odorico, M. Fischer, T. W. Hänsch, and A. Manescau, "High-precision wavelength calibration of astronomical spectrographs with laser frequency combs," Monthly Notices of the Royal Astronomical Society **380**, 839–847 (2007).

[29] C.-H. Li, A. J. Benedick, P. Fendel, A. G. Glenday, F. X. Kartner, D. F. Phillips, D. Sasselov, A. Szentgyorgyi, and R. L. Walsworth, "A laser frequency comb that enables radial velocity measurements with a precision of 1 cm s^{-1}," Nature **452**, 610–612 (2008).

[30] T. Steinmetz, T. Wilken, C. Araujo-Hauck, R. Holzwarth, T. W. Hänsch, L. Pasquini, A. Manescau, S. D'Odorico, M. T. Murphy, T. Kentischer, W. Schmidt, and T. Udem, "Laser frequency combs for astronomical observations," Science **321**, 1335–1337 (2008).

[31] A. Bartels, S. A. Diddams, C. W. Oates, G. Wilpers, J. C. Bergquist, W. H. Oskay, and L. Hollberg, "Femtosecond-laser-based synthesis of ultrastable microwave signals from optical frequency references," Opt. Lett. **30**, 667–669 (2005).

[32] J. J. McFerran, E. N. Ivanov, A. Bartels, G. Wilpers, C. W. Oates, S. A. Diddams, and L. Hollberg, "Low-noise synthesis of microwave signals from an optical source," Electronics Letters **41**, 650–651 (2005).

[33] Z. Jiang, C.-B. Huang, D. E. Leaird, and A. M. Weiner, "Optical arbitrary waveform processing of more than 100 spectral comb lines," Nature Photonics **1**, 463–467 (2007).

[34] N. K. Fontaine, R. P. Scott, J. Cao, A. Karalar, W. Jiang, K. Okamoto, J. P. Heritage, B. H. Kolner, and S. J. B. Yoo, "32 phase $\times$ 32 amplitude optical arbitrary waveform generation," Opt. Lett. **32**, 865–867 (2007).

[35] A. L. Gaeta, M. Lipson, and T. J. Kippenberg, "Photonic-chip-based frequency combs," Nature Photonics **13**, 158–169 (2019).

[36] P. Del'Haye, "Optical frequency comb generation in monolithic microresonators," Ph.D. thesis, Ludwig-Maximilians-Universität-München (2011).

[37] I.-W. Hsieh, X. Chen, X. Liu, J. I. Dadap, N. C. Panoiu, C.-Y. Chou, F. Xia, W. M. Green, Y. A. Vlasov, and R. M. Osgood, "Supercontinuum generation in silicon photonic wires," Opt. Express **15**, 15242–15249 (2007).

[38] R. K. W. Lau, M. R. E. Lamont, A. G. Griffith, Y. Okawachi, M. Lipson, and A. L. Gaeta, "Octave-spanning mid-infrared supercontinuum generation in silicon nanowaveguides," Opt. Lett. **39**, 4518–4521 (2014).

[39] B. Kuyken, T. Ideguchi, S. Holzner, M. Yan, T. W. Hänsch, J. Van Campenhout, P. Verheyen, S. Coen, F. Leo, R. Baets, G. Roelkens, and N. Picqué, "An octave-spanning mid-infrared frequency comb generated in a silicon nanophotonic wire waveguide," Nature Communications **6**, 6310 (2015).

[40] R. Halir, Y. Okawachi, J. S. Levy, M. A. Foster, M. Lipson, and A. L. Gaeta, "Ultrabroadband supercontinuum generation in a CMOS-compatible platform," Opt. Lett. **37**, 1685–1687 (2012).

[41] A. R. Johnson, A. S. Mayer, A. Klenner, K. Luke, E. S. Lamb, M. R. E. Lamont, C. Joshi, Y. Okawachi, F. W. Wise, M. Lipson, U. Keller, and A. L. Gaeta, "Octave-spanning coherent supercontinuum generation in a silicon nitride waveguide," Opt. Lett. **40**, 5117–5120 (2015).

[42] Y. Okawachi, M. Yu, J. Cardenas, X. Ji, M. Lipson, and A. L. Gaeta, "Co-

herent, directional supercontinuum generation," Opt. Lett. **42**, 4466–4469 (2017).

[43] H. Guo, C. Herkommer, A. Billat, D. Grassani, C. Zhang, M. H. P. Pfeiffer, W. Weng, C.-S. Brès, and T. J. Kippenberg, "Mid-infrared frequency comb via coherent dispersive wave generation in silicon nitride nanophotonic waveguides," Nature Photonics **12**, 330–335 (2018).

[44] D. R. Carlson, D. D. Hickstein, A. Lind, S. Droste, D. Westly, N. Nader, I. Coddington, N. R. Newbury, K. Srinivasan, S. A. Diddams, and S. B. Papp, "Self-referenced frequency combs using high-efficiency silicon-nitride waveguides," Opt. Lett. **42**, 2314–2317 (2017).

[45] J. Yuan, Z. Kang, F. Li, X. Zhang, X. Sang, Q. Wu, B. Yan, K. Wang, X. Zhou, K. Zhong, G. Zhou, C. Yu, C. Lu, H. Y. Tam, and P. K. A. Wai, "Mid-infrared octave-spanning supercontinuum and frequency comb generation in a suspended germanium-membrane ridge waveguide," Journal of Lightwave Technology **35**, 2994–3002 (2017).

[46] C. R. Phillips, C. Langrock, J. S. Pelc, M. M. Fejer, J. Jiang, M. E. Fermann, and I. Hartl, "Supercontinuum generation in quasi-phase-matched $LiNbO_3$ waveguide pumped by a tm-doped fiber laser system," Opt. Lett. **36**, 3912–3914 (2011).

[47] M. Yu, B. Desiatov, Y. Okawachi, A. L. Gaeta, and M. Lončar, "Coherent two-octave-spanning supercontinuum generation in lithium-niobate waveguides," Opt. Lett. **44**, 1222–1225 (2019).

[48] D. D. Hickstein, H. Jung, D. R. Carlson, A. Lind, I. Coddington, K. Srinivasan, G. G. Ycas, D. C. Cole, A. Kowligy, C. Fredrick, S. Droste, E. S. Lamb, N. R. Newbury, H. X. Tang, S. A. Diddams, and S. B. Papp, "Ultrabroadband supercontinuum generation and frequency-comb stabilization using on-chip waveguides with both cubic and quadratic nonlinearities," Phys. Rev. Applied **8**, 014025 (2017).

[49] P. Del'Haye, A. Schliesser, O. Arcizet, T. Wilken, R. Holzwarth, and T. J. Kippenberg, "Optical frequency comb generation from a monolithic microresonator," Nature **450**, 1214–1217 (2007).

[50] A. G. Griffith, R. K. Lau, J. Cardenas, Y. Okawachi, A. Mohanty, R. Fain, Y. H. D. Lee, M. Yu, C. T. Phare, C. B. Poitras, A. L. Gaeta, and M. Lipson, "Silicon-chip mid-infrared frequency comb generation," Nature Communications **6**, 6299 (2015).

[51] B. J. M. Hausmann, I. Bulu, V. Venkataraman, P. Deotare, and M. Lončar, "Diamond nonlinear photonics," Nature Photonics **8**, 369 (2014).

[52] C. Wang, M. Zhang, R. Zhu, H. Hu, H. Chen, and M. Lončar, "On-chip Kerr frequency comb generation in lithium niobate microresonators," in "2018 Conference on Lasers and Electro-Optics (CLEO)," (2018), pp. 1–2.

[53] H. Jung, R. Stoll, X. Guo, D. Fischer, and H. X. Tang, "Green, red, and ir frequency comb line generation from single ir pump in AlN microring resonator," Optica **1**, 396–399 (2014).

[54] L. Razzari, D. Duchesne, M. Ferrera, R. Morandotti, S. Chu, B. E. Little, and D. J. Moss, "CMOS-compatible integrated optical hyper-parametric oscillator," Nature Photonics **4**, 41 (2009).

[55] M. Pu, L. Ottaviano, E. Semenova, and K. Yvind, "Efficient frequency comb generation in AlGaAs-on-insulator," Optica **3**, 823–826 (2016).

[56] A. A. Savchenkov, A. B. Matsko, V. S. Ilchenko, I. Solomatine, D. Seidel, and L. Maleki, "Tunable Optical Frequency Comb with a Crystalline Whispering Gallery Mode Resonator," Physical Review Letters **101**, 093902 (2008).

[57] I. S. Grudinin, N. Yu, and L. Maleki, "Generation of optical frequency combs with a CaF_2 resonator," Opt. Lett. **34**, 878–880 (2009).

[58] W. Liang, A. A. Savchenkov, A. B. Matsko, V. S. Ilchenko, D. Seidel, and L. Maleki, "Generation of near-infrared frequency combs from a MgF2 whispering gallery mode resonator," Optics Letters **36**, 2290–2292 (2011).

[59] D. J. Wilson, K. Schneider, S. Hoenl, M. Anderson, T. J. Kippenberg, and P. Seidler, "Integrated gallium phosphide nonlinear photonics," arXiv e-prints arXiv:1808.03554 (2018).

[60] K. Saha, Y. Okawachi, B. Shim, J. S. Levy, R. Salem, A. R. Johnson, M. A. Foster, M. R. E. Lamont, M. Lipson, and A. L. Gaeta, "Modelocking and femtosecond pulse generation in chip-based frequency combs," Optics Express **21**, 1335–1343 (2013).

[61] Y. Okawachi, K. Saha, J. S. Levy, Y. H. Wen, M. Lipson, and A. L. Gaeta, "Octave-spanning frequency comb generation in a silicon nitride chip," Opt. Lett. **36**, 3398–3400 (2011).

[62] K. Luke, Y. Okawachi, M. R. E. Lamont, A. L. Gaeta, and M. Lipson, "Broadband mid-infrared frequency comb generation in a Si_3N_4 microresonator," Opt. Lett. **40**, 4823–4826 (2015).

[63] M. A. Foster, J. S. Levy, O. Kuzucu, K. Saha, M. Lipson, and A. L. Gaeta, "Silicon-based monolithic optical frequency comb source," Opt. Express **19**, 14233–14239 (2011).

[64] P.-H. Wang, Y. Xuan, L. Fan, L. T. Varghese, J. Wang, Y. Liu, X. Xue, D. E. Leaird, M. Qi, and A. M. Weiner, "Drop-port study of microresonator frequency combs: power transfer, spectra and time-domain characterization," Opt. Express **21**, 22441–22452 (2013).

[65] H. H. Hopkins and N. S. Kapany, "A Flexible Fibrescope, using Static Scanning," Nature **173**, 39–41 (1954).

[66] K. C. Kao and G. A. Hockham, "Dielectric-fibre surface waveguides for optical frequencies," Proceedings of the Institution of Electrical Engineers **113**, 1151–1158 (1966).

[67] R. Otte, B. Bottoms, T. Bowen, G. Celler, L. Giovane, M. Glick, R. Grzybowski, L. Kimerling, T. Miao, P. Popescu, and J. Sinsky, "Scaling limits for copper interconnects," MIT Microphotonics Center, CTR III White Paper (2011).

[68] D. A. B. Miller, "Optical interconnects to silicon," IEEE Journal of Selected Topics in Quantum Electronics **6**, 1312–1317 (2000).

[69] R. Soref, "The past, present, and future of silicon photonics," IEEE Journal of Selected Topics in Quantum Electronics **12**, 1678–1687 (2006).

[70] B. Jalali and S. Fathpour, "Silicon photonics," Journal of Lightwave Technology **24**, 4600–4615 (2006).

[71] K. Luke, A. Dutt, C. B. Poitras, and M. Lipson, "Overcoming Si_3N_4 film stress limitations for high quality factor ring resonators," Opt. Express **21**, 22829–22833 (2013).

[72] X. Ji, F. A. S. Barbosa, S. P. Roberts, A. Dutt, J. Cardenas, Y. Okawachi, A. Bryant, A. L. Gaeta, and M. Lipson, "Ultra-low-loss on-chip resonators with sub-milliwatt parametric oscillation threshold," Optica **4**, 619–624 (2017).

[73] J. Tyndall, "Six lectures on light," Longmans, Green, and Co. (1873).

[74] COMSOL Multiphysics ®v. 5.2., www.comsol.com, COMSOL AB, Stockholm, Sweden.

[75] J. S. Levy, "Integrated nonlinear optics in silicon nitride waveguides and resonators," Ph.D. thesis, Cornell University (2011).

[76] V. Venkataraman, K. Saha, and A. L. Gaeta, "Phase modulation at the few-photon level for weak-nonlinearity-based quantum computing," Nature Photonics **7**, 138 (2012).

[77] D. Popmintchev, C. Hernández-García, F. Dollar, C. Mancuso, J. A. Pérez-Hernández, M.-C. Chen, A. Hankla, X. Gao, B. Shim, A. L. Gaeta, M. Tarazkar, D. A. Romanov, R. J. Levis, J. A. Gaffney, M. Foord, S. B. Libby, A. Jaron-Becker, A. Becker, L. Plaja, M. M. Murnane, H. C. Kapteyn, and T. Popmintchev, "Ultraviolet surprise: Efficient soft x-ray high-harmonic generation in multiply ionized plasmas," Science **350**, 1225–1231 (2015).

[78] J. Leuthold, C. Koos, and W. Freude, "Nonlinear silicon photonics," Nature Photonics **4**, 535 (2010).

[79] M. Dinu, F. Quochi, and H. Garcia, "Third-order nonlinearities in silicon at telecom wavelengths," Applied Physics Letters **82**, 2954–2956 (2003).

[80] C. Kittel, *Introduction to Solid State Physics* (Wiley, 1986), 6th ed.

[81] R. K. W. Lau, M. R. E. Lamont, Y. Okawachi, and A. L. Gaeta, "Effects of multiphoton absorption on parametric comb generation in silicon microresonators," Opt. Lett. **40**, 2778–2781 (2015).

[82] M. Yu, Y. Okawachi, A. G. Griffith, M. Lipson, and A. L. Gaeta, "Mode-locked mid-infrared frequency combs in a silicon microresonator," Optica **3**, 854–860 (2016).

[83] D. K. Armani, T. J. Kippenberg, S. M. Spillane, and K. J. Vahala, "Ultra-high-Q toroid microcavity on a chip," Nature **421**, 925–928 (2003).

[84] R. H. Stolen and E. P. Ippen, "Raman gain in glass optical waveguides," Applied Physics Letters **22**, 276–278 (1973).

[85] Q.-F. Yang, X. Yi, K. Y. Yang, and K. Vahala, "Stokes solitons in optical microcavities," Nature Physics **13**, 53 (2016).

[86] T. J. Kippenberg, S. M. Spillane, D. K. Armani, and K. J. Vahala, "Ultralow-threshold microcavity Raman laser on a microelectronic chip," Opt. Lett. **29**, 1224–1226 (2004).

[87] Y. Wang, M. Anderson, S. Coen, S. G. Murdoch, and M. Erkintalo, "Stimulated Raman scattering imposes fundamental limits to the duration and bandwidth of temporal cavity solitons," Phys. Rev. Lett. **120**, 053902 (2018).

[88] E. Vella, F. Messina, M. Cannas, and R. Boscaino, "Unraveling exciton dynamics in amorphous silicon dioxide: Interpretation of the optical features from 8 to 11 ev," Phys. Rev. B **83**, 174201 (2011).

[89] M. Vogt and R. Hauptmann, "Plasma-deposited passivation layers for moisture and water protection," Surface and Coatings Technology **74-75**, 676 – 681 (1995). Fourth International Conference on Plasma Surface Engineering Part 2.

[90] J. Ye, "Optical Metrology : Everything under control," Nature Photonics **55**, 447–448 (2007).

[91] N. Picqué and T. W. Hänsch, "Frequency comb spectroscopy," Nature Photonics **13**, 146–157 (2019).

[92] I. Coddington, N. Newbury, and W. Swann, "Dual-comb spectroscopy," Optica **3**, 414–426 (2016).

[93] S. Okubo, K. Iwakuni, H. Inaba, K. Hosaka, A. Onae, H. Sasada, and F.-L. Hong, "Ultra-broadband dual-comb spectroscopy across 1.0–1.9 μm," Applied Physics Express **8**, 082402 (2015).

[94] F. Keilmann, C. Gohle, and R. Holzwarth, "Time-domain mid-infrared frequency-comb spectrometer," Opt. Lett. **29**, 1542–1544 (2004).

[95] K. Minoshima and H. Matsumoto, "High-accuracy measurement of 240-m distance in an optical tunnel by use of a compact femtosecond laser," Appl. Opt. **39**, 5512–5517 (2000).

[96] I. Coddington, W. C. Swann, L. Nenadovic, and N. R. Newbury, "Rapid

and precise absolute distance measurements at long range," Nature Photonics **3**, 351 (2009).

[97] J. M. Dudley, G. Genty, and S. Coen, "Supercontinuum generation in photonic crystal fiber," Rev. Mod. Phys. **78**, 1135–1184 (2006).

[98] L. A. Lugiato and R. Lefever, "Spatial dissipative structures in passive optical systems," Phys. Rev. Lett. **58**, 2209–2211 (1987).

[99] M. Haelterman, S. Trillo, and S. Wabnitz, "Dissipative modulation instability in a nonlinear dispersive ring cavity," Optics Communications **91**, 401 – 407 (1992).

[100] Y. Okawachi, M. Yu, V. Venkataraman, P. M. Latawiec, A. G. Griffith, M. Lipson, M. Lončar, and A. L. Gaeta, "Competition between Raman and Kerr effects in microresonator comb generation," Opt. Lett. **42**, 2786–2789 (2017).

[101] M. R. E. Lamont, Y. Okawachi, and A. L. Gaeta, "Route to stabilized ultrabroadband microresonator-based frequency combs," Optics Letters **38**, 3478–3481 (2013).

[102] T. Herr, V. Brasch, J. D. Jost, C. Y. Wang, N. M. Kondratiev, M. L. Gorodetsky, and T. J. Kippenberg, "Temporal solitons in optical microresonators," Nature Photonics **8**, 145–152 (2014).

[103] X. Yi, Q.-F. Yang, K. Y. Yang, M.-G. Suh, and K. Vahala, "Soliton frequency comb at microwave rates in a high-Q silica microresonator," Optica **2**, 1078–1085 (2015).

[104] K. E. Webb, M. Erkintalo, S. Coen, and S. G. Murdoch, "Experimental observation of coherent cavity soliton frequency combs in silica microspheres," Opt. Lett. **41**, 4613–4616 (2016).

[105] X. Yi, Q.-F. Yang, K. Y. Yang, and K. Vahala, "Active capture and stabilization of temporal solitons in microresonators," Opt. Lett. **41**, 2037–2040 (2016).

[106] J. R. Stone, T. C. Briles, T. E. Drake, D. T. Spencer, D. R. Carlson, S. A. Diddams, and S. B. Papp, "Thermal and nonlinear dissipative-soliton dynamics in Kerr-microresonator frequency combs," Phys. Rev. Lett. **121**, 063902 (2018).

[107] S. Zhang, J. M. Silver, L. D. Bino, F. Copie, M. T. M. Woodley, G. N. Ghalanos, A. Ø. Svela, N. Moroney, and P. Del'Haye, "Sub-milliwatt-level microresonator solitons with extended access range using an auxiliary laser," Optica **6**, 206–212 (2019).

[108] S. H. Lee, D. Y. Oh, Q.-F. Yang, B. Shen, H. Wang, K. Y. Yang, Y.-H. Lai, X. Yi, X. Li, and K. Vahala, "Towards visible soliton microcomb generation," Nature Communications **8**, 1295 (2017).

[109] Z. Lu, W. Wang, W. Zhang, S. T. Chu, B. E. Little, M. Liu, L. Wang, C.-L. Zou, C.-H. Dong, B. Zhao, and W. Zhao, "Deterministic generation and switching of dissipative Kerr soliton in a thermally controlled microresonator," AIP Advances **9**, 025314 (2019).

[110] Y. HE, Q.-F. Yang, J. Ling, R. Luo, H. Liang, M. Li, B. Shen, H. Wang, K. Vahala, and Q. Lin, "A self-starting bi-chromatic $LiNbO_3$ soliton microcomb," arXiv e-prints arXiv:1812.09610 (2018).

[111] Z. Gong, X. Liu, Y. Xu, M. Xu, J. B. Surya, J. Lu, A. Bruch, C. Zou, and H. X. Tang, "Soliton microcomb generation at 2 μm in z-cut lithium niobate microring resonators," Opt. Lett. **44**, 3182–3185 (2019).

[112] Z. Gong, A. Bruch, M. Shen, X. Guo, H. Jung, L. Fan, X. Liu, L. Zhang, J. Wang, J. Li, J. Yan, and H. X. Tang, "High-fidelity cavity soliton generation in crystalline AlN micro-ring resonators," Opt. Lett. **43**, 4366–4369 (2018).

[113] V. Brasch, M. Geiselmann, T. Herr, G. Lihachev, M. H. P. Pfeiffer, M. L. Gorodetsky, and T. J. Kippenberg, "Photonic chip–based optical frequency comb using soliton Cherenkov radiation," Science **351**, 357–360 (2016).

[114] P.-H. Wang, J. A. Jaramillo-Villegas, Y. Xuan, X. Xue, C. Bao, D. E. Leaird, M. Qi, and A. M. Weiner, "Intracavity characterization of micro-comb generation in the single-soliton regime," Opt. Express **24**, 10890–10897 (2016).

[115] C. Joshi, J. K. Jang, K. Luke, X. Ji, S. A. Miller, A. Klenner, Y. Okawachi, M. Lipson, and A. L. Gaeta, "Thermally controlled comb generation and soliton modelocking in microresonators," Opt. Lett. **41**, 2565–2568 (2016).

[116] Q. Li, T. C. Briles, D. A. Westly, T. E. Drake, J. R. Stone, B. R. Ilic, S. A. Diddams, S. B. Papp, and K. Srinivasan, "Stably accessing octave-spanning microresonator frequency combs in the soliton regime," Optica **4**, 193–203 (2017).

[117] H. Guo, M. Karpov, E. Lucas, A. Kordts, M. H. P. Pfeiffer, V. Brasch, G. Lihachev, V. E. Lobanov, M. L. Gorodetsky, and T. J. Kippenberg, "Universal dynamics and deterministic switching of dissipative Kerr solitons in optical microresonators," Nature Physics **13**, 94 (2016).

[118] M. H. P. Pfeiffer, C. Herkommer, J. Liu, H. Guo, M. Karpov, E. Lucas, M. Zervas, and T. J. Kippenberg, "Octave-spanning dissipative Kerr soliton frequency combs in $\mathrm{Si_3N_4}$ microresonators," Optica **4**, 684–691 (2017).

[119] V. Brasch, M. Geiselmann, M. H. P. Pfeiffer, and T. J. Kippenberg, "Bringing short-lived dissipative Kerr soliton states in microresonators into a steady state," Opt. Express **24**, 29312–29320 (2016).

[120] M. Yu, J. K. Jang, Y. Okawachi, A. G. Griffith, K. Luke, S. A. Miller, X. Ji, M. Lipson, and A. L. Gaeta, "Breather soliton dynamics in microresonators," Nature Communications **8**, 14569 (2017).

[121] C. Bao, J. A. Jaramillo-Villegas, Y. Xuan, D. E. Leaird, M. Qi, and A. M. Weiner, "Observation of Fermi-Pasta-Ulam recurrence induced by breather solitons in an optical microresonator," Phys. Rev. Lett. **117**, 163901 (2016).

[122] E. Lucas, M. Karpov, H. Guo, M. L. Gorodetsky, and T. J. Kippenberg, "Breathing dissipative solitons in optical microresonators," Nature Communications **8**, 736 (2017).

[123] C. Joshi, A. Klenner, Y. Okawachi, M. Yu, K. Luke, X. Ji, M. Lipson, and A. L. Gaeta, "Counter-rotating cavity solitons in a silicon nitride microresonator," Opt. Lett. **43**, 547–550 (2018).

[124] Q.-F. Yang, X. Yi, K. Y. Yang, and K. Vahala, "Counter-propagating solitons in microresonators," Nat. Photon. **11**, 560–564 (2017).

[125] R. Bouchand, W. Weng, E. Lucas, and T. Kippenberg, "Cherenkov radiation induced symmetry breaking in counter propagating dissipative Kerr solitons," arXiv e-prints (2019).

[126] D. C. Cole, E. S. Lamb, P. Del'Haye, S. A. Diddams, and S. B. Papp, "Soliton crystals in Kerr resonators," Nature Photonics **11**, 671–676 (2017).

[127] J. K. Jang, Y. Okawachi, M. Yu, K. Luke, X. Ji, M. Lipson, and A. L. Gaeta,

"Dynamics of mode-coupling-induced microresonator frequency combs in normal dispersion," Opt. Express **24**, 28794–28803 (2016).

[128] B. Y. Kim, Y. Okawachi, J. K. Jang, M. Yu, X. Ji, Y. Zhao, C. Joshi, M. Lipson, and A. L. Gaeta, "Turn-key, high-efficiency Kerr comb source," arXiv e-prints arXiv:1907.07164 (2019).

[129] Newport Corporation, *Velocity TLB-6700 Datasheet*.

[130] A. Arbabi and L. L. Goddard, "Measurements of the refractive indices and thermo-optic coefficients of $\mathrm{Si_3N_4}$ and SiO_x using microring resonances," Opt. Lett. **38**, 3878–3881 (2013).

[131] J. C. A. Peltier, "Nouvelles expériences sur la caloricité des courants électrique," Annales de Chimie et de Physique **56** (1834).

[132] T. Herr, K. Hartinger, J. Riemensberger, C. Y. Wang, E. Gavartin, R. Holzwarth, M. L. Gorodetsky, and T. J. Kippenberg, "Universal formation dynamics and noise of Kerr-frequency combs in microresonators," Nature Photonics **6**, 480–487 (2012).

[133] R. Hui and A. Mecozzi, "Phase noise of fourwave mixing in semiconductor lasers," Applied Physics Letters **60**, 2454–2456 (1992).

[134] Redfern Integrated Optics, *RIO Orion Datasheet*.

[135] J. Hirano and T. Kimura, "Multiple mode locking of lasers," IEEE Journal of Quantum Electronics **5**, 219–225 (1969).

[136] H. Taheri, A. B. Matsko, and L. Maleki, "Optical lattice trap for Kerr solitons," The European Physical Journal D **71**, 153 (2017).

[137] A. Dutt, C. Joshi, X. Ji, J. Cardenas, Y. Okawachi, K. Luke, A. L. Gaeta, and M. Lipson, "On-chip dual-comb source for spectroscopy," Science Advances **4** (2018).

[138] J. K. Jang, A. Klenner, X. Ji, Y. Okawachi, M. Lipson, and A. L. Gaeta, "Synchronization of coupled optical microresonators," Nature Photonics **12**, 688–693 (2018).

[139] J. K. Jang, X. Ji, C. Joshi, Y. Okawachi, M. Lipson, and A. L. Gaeta, "Sub-

harmonic synchronization of Kerr frequency combs," in "Conference on Lasers and Electro-Optics," (Optical Society of America, 2019), p. FM1D.4.

[140] Y. Zhao, X. Ji, B. Y. Kim, P. S. Donvalkar, J. K. Jang, C. Joshi, M. Yu, C. Joshi, R. R. Domeneguetti, and F. A. S. Barbosa, "Visible Nonlinear Photonics," arXiv e-prints arXiv:1907.04843 (2019).

[141] B. Stern, X. Ji, Y. Okawachi, A. L. Gaeta, and M. Lipson, "Battery-operated integrated frequency comb generator," Nature **562**, 401–405 (2018).

[142] S. Schiller, "Spectrometry with frequency combs," Opt. Lett. **27**, 766–768 (2002).

[143] T. Ideguchi, A. Poisson, G. Guelachvili, N. Picqué, and T. W. Hänsch, "Adaptive real-time dual-comb spectroscopy," Nature Communications **5**, 3375 (2014).

[144] B. Bernhardt, E. Sorokin, P. Jacquet, R. Thon, T. Becker, I. T. Sorokina, N. Picqué, and T. W. Hänsch, "Mid-infrared dual-comb spectroscopy with 2.4 μm Cr2+:ZnSe femtosecond lasers," Appl. Phys. B **100**, 3–8 (2010).

[145] G. Millot, S. Pitois, M. Yan, T. Hovhannisyan, A. Bendahmane, T. W. Hänsch, and N. Picqué, "Frequency-agile dual-comb spectroscopy," Nat. Photon. **10**, 27–30 (2016).

[146] S. M. Link, A. Klenner, M. Mangold, C. A. Zaugg, M. Golling, B. W. Tilma, and U. Keller, "Dual-comb modelocked laser," Opt. Express **23**, 5521–5531 (2015).

[147] G. Villares, J. Wolf, D. Kazakov, M. J. Süess, A. Hugi, M. Beck, and J. Faist, "On-chip dual-comb based on quantum cascade laser frequency combs," Applied Physics Letters **107**, 251104 (2015).

[148] M. Yu, Y. Okawachi, A. G. Griffith, N. Picqué, M. Lipson, and A. L. Gaeta, "Silicon-chip-based mid-infrared dual-comb spectroscopy," Nature Communications **9**, 1869 (2018).

[149] M.-G. Suh, Q.-F. Yang, K. Y. Yang, X. Yi, and K. J. Vahala, "Microresonator soliton dual-comb spectroscopy," Science **354**, 600–603 (2016).

[150] N. G. Pavlov, G. Lihachev, S. Koptyaev, E. Lucas, M. Karpov, N. M. Kondratiev, I. A. Bilenko, T. J. Kippenberg, and M. L. Gorodetsky, "Soliton

dual frequency combs in crystalline microresonators," Opt. Lett. **42**, 514–517 (2017).

[151] T. Ideguchi, T. Nakamura, Y. Kobayashi, and K. Goda, "Kerr-lens mode-locked bidirectional dual-comb ring laser for broadband dual-comb spectroscopy," Optica **3**, 748–753 (2016).

[152] K. Kieu and M. Mansuripur, "All-fiber bidirectional passively mode-locked ring laser," Opt. Lett. **33**, 64–66 (2008).

[153] R. Gowda, N. Nguyen, J.-C. Diels, R. A. Norwood, N. Peyghambarian, and K. Kieu, "All-fiber bidirectional optical parametric oscillator for precision sensing," Opt. Lett. **40**, 2033–2036 (2015).

[154] S. Mehravar, R. A. Norwood, N. Peyghambarian, and K. Kieu, "Real-time dual-comb spectroscopy with a free-running bidirectionally mode-locked fiber laser," Appl. Phys. Lett. **108**, 231104 (2016).

[155] L. Del Bino, J. M. Silver, S. L. Stebbings, and P. Del'Haye, "Symmetry Breaking of Counter-Propagating Light in a Nonlinear Resonator," Scientific Reports **7**, 43142 (2017).

[156] J. M. Silver, L. D. Bino, and P. Del'Haye, "A nonlinear enhanced microresonator gyroscope," in "Conference on Lasers and Electro-Optics," (Optical Society of America, 2017), p. SM1M.2.

[157] C. Wang and C. P. Search, "Enhanced rotation sensing by nonlinear interactions in silicon microresonators," Opt. Lett. **39**, 4376–4379 (2014).

[158] E. Lucas, H. Guo, J. D. Jost, M. Karpov, and T. J. Kippenberg, "Detuning-dependent properties and dispersion-induced instabilities of temporal dissipative Kerr solitons in optical microresonators," Phys. Rev. A **95**, 043822 (2017).

[159] S. R. Kurtz, "Mixers as phase detectors," WJ Tech-Note (1978).

[160] Menlo Systems, *Menlo Systems DXD 200 Phase Detector Manual*.

[161] O. Bryngdahl, "Image formation using self-imaging techniques," J. Opt. Soc. Am. **63**, 416–419 (1973).

[162] L. B. Soldano, F. B. Veerman, M. K. Smit, B. H. Verbeek, A. H. Dubost, and E. C. M. Pennings, "Planar monomode optical couplers based on multimode interference effects," Journal of Lightwave Technology **10**, 1843–1850 (1992).

[163] B. Stern, X. Ji, A. Dutt, and M. Lipson, "Compact narrow-linewidth integrated laser based on a low-loss silicon nitride ring resonator," Opt. Lett. **42**, 4541–4544 (2017).

[164] T. Lin, A. Dutt, X. Ji, C. T. Phare, C. Joshi, O. A. J. Gordillo, M. C. Shin, A. L. Gaeta, and M. Lipson, "Long-term stabilization and operation of a soliton micro-comb for 9-days," in "Conference on Lasers and Electro-Optics," (Optical Society of America, 2019), p. STu3J.5.

[165] T. Lin, A. Dutt, X. Ji, C. Joshi, A. L. Gaeta, and M. Lipson, "Broadband high-resolution scanning of soliton micro-combs," in "Conference on Lasers and Electro-Optics," (Optical Society of America, 2019), p. SF3H.6.

[166] M. Yu, Y. Okawachi, C. Joshi, X. Ji, M. Lipson, and A. L. Gaeta, "Gas-Phase Microresonator-Based Comb Spectroscopy without an External Pump Laser," ACS Photonics **5**, 2780–2785 (2018).